UNIVERSITY OF CAPE TOWN
IYUNIVESITHI YASEKAPA • UNIVERSITEIT VAN KAAPSTAD

Department of Civil Engineering

Computational Continuum Mechanics Group

Growth, Modelling and Remodelling of Cardiac Tissue: A Multiphase Approach

A dissertation in partial fulfilment of the requirements for a Master of Sciences degree in the field of Civil Engineering

Prepared for: University of Cape Town

Author:
Mr. Gary Hopkins

Supervisor:
Dr. Sebastian Skatulla

The financial assistance of the National Research Foundation (NRF) towards this research is hereby acknowledged. Opinions expressed and conclusions arrived at, are those of the author and are not necessarily to be attributed to the NRF.

June 18, 2017

Plagiarism Declaration

- I know that plagiarism is wrong. Plagiarism is to use another's work and to pretend that it is one's own.
- Each significant contribution to and quotation in this document from the work or works of other people has been attributed and has been cited and referenced.
- This thesis is my own work.
- I have not allowed and will not allow anyone to copy my work with the intention of passing it as his or her own work.
- This dissertation has been submitted to the Turnitin module and I confirm that my supervisor has seen my report and any concerns revealed by such have been resolved with my supervisor.

Name	**Student No**	**Date**	**Signed**
Gary Hopkins	HPKGAR001	18/06/2017	Signed by candidate

Abstract

Rheumatic heart disease (RHD) is identified as a serious health concern in developing countries, specifically amongst young individuals, accounting for between 250 000 and 1.4 million deaths annually. As such, the attention of this research is initially placed on the importance of the development of a cardiac analysis toolbox with functionality for pathophysiological analysis of the disease. Subsequently, in order to further the understanding of the mechanisms of the disease as linked to cardiomyocyte growth and remodelling of the microstructure, a continuum bi-phasic model applicable to cardiac tissue is formulated based on the theory of porous media (TPM). This makes it possible to account for interactions and contributions of multiple phases of constituent materials, which in computational cardiac modelling are the solid phase - the cardiac tissue - and the liquid phase - blood and interstitial fluid.

Subsequent attention is paid to the cardiac model development in order to implement a sound base on which to add strain-driven phase transition via a mass supply function proposed within this study. To this end, based on thermodynamical restrictions, constitutive relations are proposed for stress, permeability, seepage velocity, mass supply and interaction forces such as friction. The approach is implemented in the in-house computational cardiac mechanics toolbox SESKA which supports finite element as well as Element-free *Galerkin*-based approximations. This investigation considers the passive and active non-linear elastic material behaviour of the myocardium of the left ventricle coupled with porous media theory, along with an an additional coupling to the haemodynamics of the circulatory system, facilitating modelling of the full cardiac cycle.

As such, an initial cardiac growth and remodelling computer model is developed as an initial step to computational modelling of the adverse effects of RHD and other similar inflammatory heart diseases, with the potential to limit the invasiveness and risk of in-vivo patient studies. A patient specific case study is conducted, making use of cardiovascular magnetic resonance scans taken over a period of two years from a patient affected by RHD to generate realistic 3D computer models, from which information is drawn with regards to the pathophysiological behaviour of the disease.

Acknowledgements

Soli Deo gloria

To my supervisor, Dr. Sebastian Skatulla; for the many hours spent assisting with understanding difficult theory and finding solutions to computer code which would not behave, for giving me with the opportunity to travel to Germany for an extended period of time, and for providing me with an extremely interesting and relevant topic; one which was intrinsically challenging and which I hope will further the medical knowledge in the field for individuals affected by this debilitating disease.

To Prof. Tim Ricken and his research group at the Technical University of Dortmund, Germany; for hosting me during my travels and providing me with unlimited assistance and a great experience of their country; I am incredibly thankful for this.

To Prof. Ntobeko Ntusi; for his collaboration in this research, for providing expert medical input and financial assistance with computer software.

To Jess, my amazing fiancée; for her continual support and encouragement.

To my parents; for their financial assistance and encouragement, and to my brother; for his support.

To the research group at UCT and the friends I have made; for many conversations sorting out theory, and many other hours making the most of this beautiful city in which we live.

To UCT and the NRF; for providing me with postgraduate funding allowing me to complete my degree.

Table of Contents

List of Figures

List of Tables

Chapter 1

Introduction

1.1 Background to study

Alongside epidemiological and clinical studies, mathematical modelling is often used as one of the research tools to gain basic understanding of the function of the beating heart; providing information in terms of the interactions between electro-physiological, biomolecular and biomechanical processes under both healthy and pathological conditions [11]. Resulting from a need for further understanding in the field of cardiac mechanics and pathophysiology, such cardiac electro-mechanic models have been gradually developing to a stage of accuracy and complexity with which they can be used as a diagnostic tool.

With increasing availability of computing power, biomechanics is rapidly emerging as an area of research bringing together multidisciplinary research concerned with understanding the behaviour of biological structures at various scales, ranging from the level of organs, down to study on the cellular level [82]. The application of continuum mechanics methods in the area of bioengineering is recognised as having a significant impact on developments in this field. It is possible to apply the principles of continuum mechanics to better understand biological structures, and such models aid in the quantification of the mechanical environment in states of health, injury and disease [82]. As a consequence, this leads to advances in therapeutic and diagnostic procedures and methods [82].

Due to advances in microscopic technology to characterise the molecular changes taking place during heart failure, it is feasible to mathematically describe the associated processes on the microscopic level using phenomenological approaches; for example the description of muscle growth. The detailed description of the heart's micro-structure, physiology and pathophysiology allows for specific processes to be targeted and computational study of their impact on the mechanical and chemical behaviour of healthy and diseased cardiac tissue [64].

The living heart is a structure which is able to grow stronger, weaker, larger or smaller within months, weeks or days as a result of micro-structural changes. Rheumatic heart disease (RHD) is associated with such changes, wherein this diseased condition of the heart is associated with significant dilation of the ventricular cavities as a result of growth and remodelling of cardiac muscle tissue, ultimately leading to heart failure and death of the affected patient.

1.2 Problem identification

The human heart beats about 100 000 times daily; delivering 7000 l of blood to the human body, and is often regarded as the most vital organ of the body [11]. However, due to its complexity, the heart is susceptible to various types of disease – referred to as cardiac diseases. Cardiac disease is viewed as a globally serious health issue; claiming more than 16 million lives worldwide annually [4]. Furthermore, the prominence of this pandemic is increasing at a concerning rate, especially in developing nations including Asia, Africa and South America. It is predicted by epidemiologists that by the year 2020 cardiac disease will be the cause of 25 million deaths annually (which translates to 36% of all annual mortality). If such predictions materialise, it will be the leading cause of death for the first time in human history, and may therefore be considered as humankind's most serious health threat [5, 58].

Compared to various types of cardiac disease such as hypertensive and ischemic, Marijon et al. [72] identifies RHD, which falls under the category of inflammatory heart disease, as the most under-represented by media and policy makers. In developing countries, due to under-representation and poor healthcare frameworks, RHD is a major burden where it causes a large portion of cardiovascular morbidity and mortality, and is regarded as a disease of poverty and low socio-economic circumstances. Estimates of annual mortality due to RHD range from 250 000 to 1.4 million [72, 93].

RHD is an autoimmune disease caused by a group A *streptococcal* infection, referred to as acute rheumatic fever (ARF) [45]. ARF causes inflammation of the heart muscle (myocarditis) and scarring of atrio-ventricular valve tissue via formation of excess fibrous connective tissue (fibrosis). Valvular damage of this manner is permanent and is the primary cause of death in affected patients, with the only current direct treatment option being replacement of damaged valves. This pathological condition is known as RHD. Resulting from the damage, a weaker pumping capacity of the heart materialises which is compensated via dilation of the ventricular cavities; leading to further dilation as overall heart function gradually deteriorates and pumping efficiency is continuously decreased, which is termed dilated cardiomyopathy (DCM).

In order to treat this condition effectively, a sound understanding of the underlying failure mechanisms involved is required. However, due to improved socio-economic conditions, infection rates of ARF are extremely low in first world countries, and as a result research capacity in this field is scarce. In terms of heart valve replacement therapy, progress has been made allowing the heart valve to regenerate. However, in such therapy the main focus has been on the infectious and inflammatory process of ARF and less on the subsequent proliferative responses (growth) of the heart. In this sense, research aiming specifically at the tertiary prevention and treatment of RHD remains inadequate. The development of effective treatment strategies requires an understanding of how changes to proliferative mechanisms impact on the overall pumping capacity of the heart, and the causes of these mechanisms thereof.

With reference to RHD and cardiac disease as a whole, it is frequently stressed that more data and research is required [37, 93].

1.3 Biomechanical modelling

Identifying the true origin of biomechanics is nearly impossible, however it is easy to say that it is as old as mechanics itself [55]. Beginning with da Vinci's [1] study into the flight of birds, ranging through Galilei's [2] interest in the structure of bones and Hooke's [3] study into linear elasticity using biological materials such as sinews and bones [15], through to Young's [4] lecture in 1808 to the Royal Society about the mechanical function of the heart and arteries; it is clear that biomechanics has been a topic which has attracted much interest over many centuries [55]. However, until the development of personal computers in the 1960's and a continual increase in computing power, along with the development of the finite element method (FEM) beginning in the 1950's, it was not possible to conduct large scale, detailed biomechanical studies [7]. In 1972, Oden [77] investigated non-linear FEM applicable to tissue mechanics. Since then, with increased attention and developing technology such as state-of-the-art medical imaging, the field of biomechanics has been developing rapidly. [96]

The history of continuum biomechanics is long and complex, however, the current potential for impacting scientific understanding and clinical intervention could not be grater [7]. With the development of biomechanics, and the later coupling of continuum mechanics and biomechanics to form continuum biomechanics, it has become possible to model *inter alia* the pathophysiology associated with chronic conditions of disease, such as heart disease. Understanding the mechanisms of growth in such chronic conditions may open new avenues in medical device design and personalised medicine to surgically or pharmacologically manipulate development and alter, control, or revert disease progression [66]. Finite element simulations employing such growth theories computationally have the potential to predict the formation of growth-induced instabilities and identify regions of growth-induced stress [66].

A distinction is made between various types of tissue modelling based on the type of adaptation; hard tissue, soft tissue and tissue remodelling [42]. Therefore, depending on the type of tissue to be modelled, deviations from classical continuum mechanics theory depend on these types of adaptation. In the following, growth and remodelling of soft tissue is addressed, with an initial focus on cardiac tissue.

1.4 Growth modelling

Due to the alarming global increase in the pandemic of heart disease [58], and the uniqueness in growth of cardiomyocytes in that they cannot divide by mitosis but can only grow by the deposition of new sarcomeres in the process of sarcomerogenesis [83], a plethora of studies have been conducted into the growth, modelling and remodelling of cardiac tissue. To this

---

[1] Leonardo da Vinci (1452-1513): Italian painter, sculptor, architect, mathematician, engineer and scientist well known for *inter alia* his studies into biomechanics.

[2] Galileo Galilei (1564-1642): Italian astronomer, physicist, mathematician, engineer, and philosopher who played a major role in the scientific revolution during the Renaissance.

[3] Robert Hooke (1635-1703): English natural philosopher, architect and polymath accredited for the discovery of the law of linear elasticity.

[4] Thomas Young (1773-1829): English polymath who made notable scientific contributions to the fields of vision, light, solid mechanics, energy and physiology.

end, in the realm of growth and remodelling, a common approach employed by various authors is the use of kinematics-based growth models which model finite growth by means of a second order growth tensor, which has been shown to be successful as a unified modelling concept [42, 43, 66, 74], and has been extensively employed in the literature. As such, the initial focus in the following is to outline the principles, strengths and weaknesses, and salient findings in studies using such an approach. Indeed, the Theory of Mixtures and Theory of Porous Media (TPM) have been successfully employed in growth and remodelling of soft biological tissue (cf. [7]), but have not appeared in the literature with applications to cardiac tissue with the exception of Werner et al. [107]. Therefore, the advantages and recent works employing TPM with applications to biological growth modelling are subsequently addressed which serve as motivation for use of porous media theory in this investigation.

1.4.1 The human heart

Amongst others, Rodriguez et al. [90] investigated the mechanics of soft elastic tissue, in which the stress dependent growth of the left ventricle was addressed. Upon this, a generic continuum-based concept for finite growth of living tissue has been presented by Göktepe et al. [42] in which an incompatible growth configuration was used which requires multiplicative decomposition of the deformation gradient tensor, common to such kinematic theories [25]. Consequently, elastic deformation of cardiac tissue is captured within one part of the deformation gradient, and the consequences of growth captured in the other, referred to as the growth tensor [66].

Within this approach, the two major challenges experienced are the characterisation of the kinematic properties of the growth tensor, and identification of the mechanical driving forces causing evolution of the tensor [42]. Indeed, these challenges are not limited to the characterisation of cardiac growth and remodelling, and are ubiquitous to all studies making use of this approach [66]. While earlier studies making use of such theory were primarily of theoretical and analytical nature, there has been a clear trend towards the computational modelling of volumetric growth, and that the shortcomings of the phenomenological theory of volumetric growth and the characterisation of the growth tensor are being overcome with the correlation of macroscopic tissue growth to microscopic observations on the cellular level [43].

In order to address these issues, Göktepe et al. [42] introduced a micro-mechanically motivated ansatz to describe the growth tensor caused by stress-driven ventricular dilation and stress-driven wall thickening, occurring independently which was subsequently adapted and implemented by Werner et al. [107] using porous media theory. Numerical examples were presented for both cases investigated by Göktepe et al. [42], with the use of a generic bi-ventricular heart model. With the use of this model, and the ansatz developed, examples considered were: the growth of an athlete's heart due to elevated pressure and increased filling, cardiac dilation as strain-driven isotropic growth, and cardiac wall thickening as a result of stress-driven isotropic growth. Agreement with clinical results was found, elucidating the link between ventricular volume/pressure overload and cardiac dilation/hypertrophy.

With the use of this approach, a mechanically driven growth criterion is introduced in order to distinguish between conditions of growth and non-growth [42]. To this end, growth is activated above a certain threshold of sarcomere stretch, which is controlled by a limiting growth function. Similar to the approach taken to predict the onset of plastic deformation in finite strain plasticity, this method contains a clear distinction between conditions. With the elastic behaviour of the material being captured in the elastic part of the deformation tensor, a generic isotropic Neo-Hookean baseline elasticity is used in order to focus on the behaviour of growth. However, more sophisticated anisotropic constitutive equations have been incorporated such as those used by Göktepe et al. [44] and Werner et al. [107]. Furthermore, within this study (and that of Werner et al. [107]) the baseline cardiac behaviour was modelled to be passive, thus neglecting the effects of active contraction (that is pumping of the heart). Growth processes are characterised through a single growing solid phase and the biochemical origin of the growing material is neglected, and thus accounted for phenomenologically and neglecting the source of the growth and thus the mass exchange process from blood to muscle tissue. Growth is determined to be driven either by stress or strain, and different methods are followed to characterise stress- and strain-driven growth respectively. Stress-driven growth is considered to cause a volumetric change of cardiomyocytes, whereas its counterpart is considered to cause sarcomere deposition resulting in cardiomyocyte stretch causing an increase in cavity volume with a constant wall thickness (cf. section 2.3 and [41]).

Using a similar kinematic approach, Göktepe et al. [43] adopted the framework of volumetric growth characterised through the concept of an incompatible growth configuration, in which the deformation gradient is once again multiplicatively split. The deformation gradient is influenced by means of internal variables called growth multipliers; common to this approach. Depending on the type of growth experienced, different types of growth multipliers were used which define the direction relative to the sarcomere axis along which mass deposition occurs. As common to this kinematic approach, the Helmholtz [5] free energy is defined as a function of the total deformation gradient and the growth part of the deformation gradient. This dependence differs substantially from multiphase theories such as proposed by Krause [63] in which the Helmholtz free energy is defined as a function of the right Cauchy Green deformation tensor and fraction of the material that is composed of solid components. Modelling the baseline characteristics of the cardiac tissue as isotropic and passive, this study introduced a generic model for eccentric and concentric growth which allows for exploration of the impact of growth on different scales and was used in the simulation of human bi-ventricular models.

When using such kinematic theories, it is advantageous to begin the simulation with a loaded state at growth equilibrium and include effects of residual stress [43]. This is of importance as shown by Ambrosi et al. [3], Imatani and Maugin [56] and Omens et al. [79], which show that growth does indeed affect residual stresses. Such an approach was conducted by Ricken et al. [87] in which a pre-run of the model was conducted under ideal loading and geometric conditions in order to determine ideal flow in the liver with an anisotropic nature of blood flow. Residual stress due to growth was included by Ateshian and Ricken [8] in which the newly deposited generation of growth may be assumed to be in a stress-free state, even though the underlying tissue remains in a loaded configuration with the implication that if growth occurs within a loaded material, it will no longer return to its previous state of stress, and residual stresses remain (cf. section 4.5.2).

Kroon et al. [65] developed a method to simulate three dimensional volumetric growth of the left ventricle, with which the reference configuration was continually updated in an investi-

---

[5] Hermann von Helmholtz (1821-1894): German physician and physicist known for his theories on the conservation of energy, and works on a mechanical foundation of thermodynamics.

gation into tissue turnover and choice of the reference configuration. It was concluded that results are indeed effected depending on this important choice. Using an updated reference configuration, it was noted that to reach an amount of growth equal to that when a fixed reference configuration was used, twice as many increments were required. In the case of updating the reference configuration, it was assumed that growth-induced internal stresses relax due to tissue turnover, and are only dependant on the previous configuration and that growth is triggered by a deviation from a predetermined value of end-diastolic myofibre strain, with the use of a growth criterion, similar to Göktepe et al. [42, 44]. Once again for the sake of comparison, the issue of the choice of reference configuration is dealt with by Ateshian and Humphrey [7], in which the reference configurations are dealt with within the framework of TPM.

Rausch et al. [83] used a kinematics-based method with the key feature of the model to define the evolution equation for the growth tensor, motivated by pressure-overload-induced sarcomerogenesis. Cardiac hypertrophy in systemic and pulmonary hypertension was modelled as a means of testing the model developed, illustrating how cardiac hypertrophy is caused due to a chronic overload of pressure.

A notable study making use of kinematic theory with a split of the deformation gradient into elastic and growth parts is that of Kerckhoffs et al. [60], in which it was tested whether the kinematic growth law adopted was able to predict concentric and eccentric hypertrophy in response to aortic stenosis and mitral valve regurgitation. A computational model of the adult canine heart was used coupled to a closed loop model of circulatory haemodynamics. It was concluded that the growth law used was sufficient, however, it was noted that while maximum cellular dimensions were limited, minimum cellular dimensions were not, important in the role of reverse remodelling and growth. Additionally, volume overload was applied upon commencement of the simulation, therefore neglecting the effect of residual stresses before volume overload. Another notable study was that of Klepach et al. [61], in which the pre- and post-operative behaviour of infarcted hearts was modelled.

Discussion

Growth and remodelling of biological tissues are a time dependant phase conversion between tissue cells and nutrients, whereby the nutrients themselves can be transported through the tissue [85]. Based on the review of available literature concerned with growth and remodelling of cardiac tissue, kinematic-based approaches are favoured. However, the multiphasic nature of biological materials is generally neglected, assuming that the liquid constituent of the material does not affect the overall mechanical and growth behaviour, and that the source of growth lies outside the system.

Therefore, in further cardiac mechanics investigation it is pertinent that a more holistic approach taking into account the multiphasic nature of cardiac tissue with consideration of the liquid phase, and growth as mass a exchange process [88] is employed. As such, biomechanical modelling approaches using porous media theory are to be addressed in the following section with consideration of relevant theory and methods required, making reference to particular studies using this approach.

1.4.2 Theory of Porous Media

As biological materials are composed of either porous hard or soft tissue saturated with a fluid medium such as blood, they are composed of multiple interacting components, and are therefore considered to be multiphasic [7, 66, 85]. Therefore, if the overall behaviour of biological material is to be accurately described taking a more accurate influence of the micro-structure into account, it becomes necessary to consider the multiple components individually. Such an approach is made possible by modelling the tissue as a multiphase continua which consists of superimposed and interacting solid and fluid phases. The tissue excluding the liquid (Figure 1.1) is summarised within the solid phase, and the extracellular fluids (such as blood [106] which contains nutrients and other components such as introduced pharmaceutical agents) are summarised within the fluid phase. The solid phase is considered to be porous in nature, while the pores are filled with fluid. The fluid phase is composed of water and several other constituents such as nutrients, but remains a homogeneous solution. In order to superimpose the behaviour of the two phases under the assumption that the porous solid phase is saturated with the liquid phase, the concept of volume fractions [63] is extended from the general thermodynamic framework of the Theory of Mixtures, developed by Bowen [20] and Truesdell and Toupin [98]. Consequently, in the case of a biphasic model, the entire volume under analysis is constituted by the solid and liquid phases; each with a specific contribution to the total volume, called the volume fraction, depicted in Figure 3.1. This concept leads to the saturation condition, stating that the sum of solid and fluid fractions within the body is equal to unity [27].

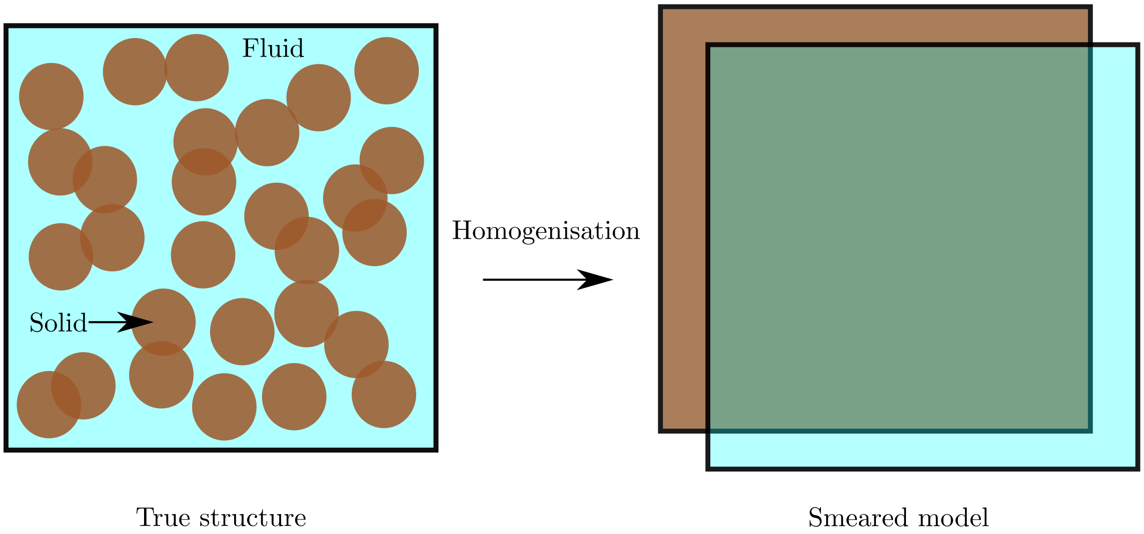

Figure 1.1. Illustration of the homogenisation and statistical distribution of a porous two phase material consisting of a solid and fluid phase, and showing the link between the micro- and macro-scale.

As a result, the deformation gradient is composed of contributions from the solid and fluid phases, via a multiplicative decomposition into the solid and fluid parts [29]. The balance equations for each constituent are taken from those of mixture theory and adapted as necessary [85]. Using the balance equations, the description of remodelling and growth processes is given by the balance equations of mass, momentum and material time derivative of the saturation condition [85]. As growth in biological materials is described as a phase conversion between tissue cells and nutrients [85, 94], growth is described by the transfer of mass from one phase to another.

The immiscible solid and fluid phases yield a coupled fluid-structure interaction, and can be described on the macroscopic level using the TPM framework as described by, amongst others Biot [16], Bowen [18], de Boer [27] and Ehlers [34]. Using this framework, and the concept of volume fractions, it is possible to model the mechanics of biological tissue, along with growth included as a mass exchange between the solid and fluid phases [85].

Based on TPM, Ricken and Bluhm [85] proposed a continuum model consisting of a solid filled with fluid containing nutrients (referred to as a tri-phase model, in which the nutrient fraction is contained within the liquid) for the phenomenological description of growth and remodelling in isotropic and transversely isotropic biological tissues. As such, a coupled calculation concept to determine the solid motion, inner pressure as well as the solid, fluid and nutrient volume fractions was put forward. In this study, a calculation concept was presented for the description of stress- and nutrient-induced growth and in its development, the solid and fluid material of the body was assumed to be incompressible, meaning that volumetric deformations only result from a change in porosity as fluid leaves the solid boundary.

Using the model developed, Ricken and Bluhm [85] conducted numerical examples involving transversely isotropic material behaviour, and optimised organic topology, in order to demonstrate performance of the concept. The isotropic material was modelled as a rectangular section containing a hole in the middle (illustrative of fasciated muscle) consisting of a solid matrix filled with fluid. When compared against analysis of an isotropic material, the transversely isotropic material showed less volumetric strain, indicating that biological materials of this nature such as muscles are less prone to injury due to the orientation of their fibres. In a similar example, Ricken et al. [86] demonstrated the application of their model with isotropic material behaviour making use of a similar specimen. In the case of the optimised organic topology, it was shown that the calculation concept predicted the rearrangement of internal structure of biological tissue in response to given loading conditions [87], showing good compliance to optimised topologies given in the literature.

Ricken et al. [87] generated a biphasic mechanical model to describe the vascular remodelling process in relation to variable pressure gradient in the liver, as a response to obstructed outflow. In order to model the effects of the transverse isotropic permeability and flow, it was assumed that initially the direction of all liver sinusoids were horizontal at the onset of analysis. As remodelling occurred, sinusoids orientated themselves parallel to the pressure gradient, and the new configuration was considered to be a reasonable physiological starting condition. Therefore, in order to determine the optimised conditions of flow before obstruction, an initial run was conducted before the introduction of flow obstruction. Once the obstruction was reintroduced, the simulation was continued and remodelling of the liver continued towards a new optimum state in which sinusoidal pressure was minimised with the formation of new vascular structures from dilated sinusoids following the direction of the highest pressure gradient.

1.5 Gap statement

As presented in section 1.4.1 it is clear that various growth models making use of kinematic approaches have been developed and applied to cardiac tissue in order to study the mechanisms of growth due to mechanical influences. Additionally, literature regarding the use of multiphase theory was presented in section 1.4.2 in order to illustrate the potential of multiphase models developed within the framework of TPM to describe growth and remodelling due to mechanical influences and the presence of nutrients. However, currently it appears only an initial attempt has been made to develop a cardiac growth model within the framework of TPM, in order to utilise the various advantages of such a multiphase approach. Specifically, the inclusion of growth as a mass exchange process, and the effects of active cardiac contraction coupled with the modelling potential of TPM have not been utilised. Additionally, it appears that computational heart models aimed particularly at the study of the pathophysiology of RHD and other inflammatory heart diseases have not been developed or made use of to date. The gap statements for this study are therefore as follows:

1. The theory of porous media has not been employed to investigate cardiac behaviour including active contraction;
2. A growth model for cardiac tissue within the TPM framework has been only partially developed; and
3. RHD mechanisms have not been studied computationally making use of realistic patient myocardial data, leading to a deficiency of knowledge of disease chronology.

1.6 Aims and objectives

This research project aims to assist in the development of a computational cardiac mechanics toolbox which facilitates patient-specific modelling of the rheumatic heart. For this purpose, 3D cardiac magnetic resonance (CMR) scans of a diseased heart at various stages provided by Cape Universities Body Imaging Centre (CUBIC) [6], serve to generate 3D left ventricular heart computer models. The main focus lies on extending the existing cardiac mechanics models which are part of the in-house simulation software SESKA to account for the proliferative mechanisms in ventricular hypertrophy - namely growth and remodelling of cardiac tissue.

In contrast to existing approaches which address such growth processes phenomenologically on the macroscopic level with exclusion of the effects of the fluid-solid interactions, this project aims to provide an initial method of mass transfer modelling between the solid and fluid phases which describes growth of cardiac tissue. In this way, the effect of the change of volume concentration of the two main constituents can be investigated.

---

[6] Faculty of Health Sciences, UCT, Groote Schuur Hospital, Cape Town, South Africa: www.cubic.uct.ac.za

Therefore, the specific research objectives of this MSc project are as follows:

1. Creation of 3D left ventricular heart models from CMR scans taken from a rheumatic heart;
2. Development and coding of a micro-structurally motivated cardiac growth model based on the multiphase continuum framework and the Theory of Porous Media;
3. Benchmarking and calibration of the multiphase computational growth model; and
4. Computational case study of the mechanisms and pathophysiology of rheumatic heart disease.

1.7 Scope and limitations

A growth model applicable to cardiac muscle is developed within the framework of TPM, in order to computationally study the pathophysiology of RHD. The developed model takes into account growth due to mechanical factors, and the orthotropic and active nature of the tissue, coupled with the haemodynamics of the circulatory system. Other factors leading to growth such as hormonal and chemical aspects are neglected due to the high complexity and lack of sufficient knowledge. The case study is to be conducted with the use of 3D left ventricular heart models produced from CMR scans of healthy and diseased patients, and atria are to not be included.

1.8 Layout of document

Following this introductory chapter in which the specific aspects of this investigation are addressed along with the pertinent literature, this document introduces relevant information regarding the physiology and pathophysiology of the human heart in Chapter 2 in which the general structure and behaviour of the heart is addressed, followed by a summary of the pathophysiology of RHD. In Chapter 3 the background concepts and porous media theory are addressed, followed by a detailed development of the cardiac growth model in Chapter 4. Subsequently, the specific aspects of cardiac mechanics and cardiac modelling are outlined in Chapter 5, following which a detailed case study of a patient presenting with RHD is conducted in Chapter 6. Based on the study, conclusions are drawn and the possibility of future work are addressed in Chapter 7.

Chapter 2

Physiology of the heart

2.1 General structure and behaviour

A mammalian heart may be thought of as two pumps operating in parallel, serving the purpose of supplying itself and the body with oxygenated blood. The first pump is comprised of the *right atrium* and *right ventricle*, shown in Figure 2.1. Blood enters the right atrium via the *venae cavae*, and passes through the *tricuspid valve* into the right ventricle. In this manner, de-oxygenated blood is transported from the *systemic circulation* into the heart. From the right ventricle, blood is pumped into the *pulmonary circulation* via the *pulmonary artery*, where it enters the lungs and *inter alia*, carbon dioxide gas leaves the blood and oxygen attaches to *haemoglobin* proteins oxygenating the blood via diffusion through the lung walls.

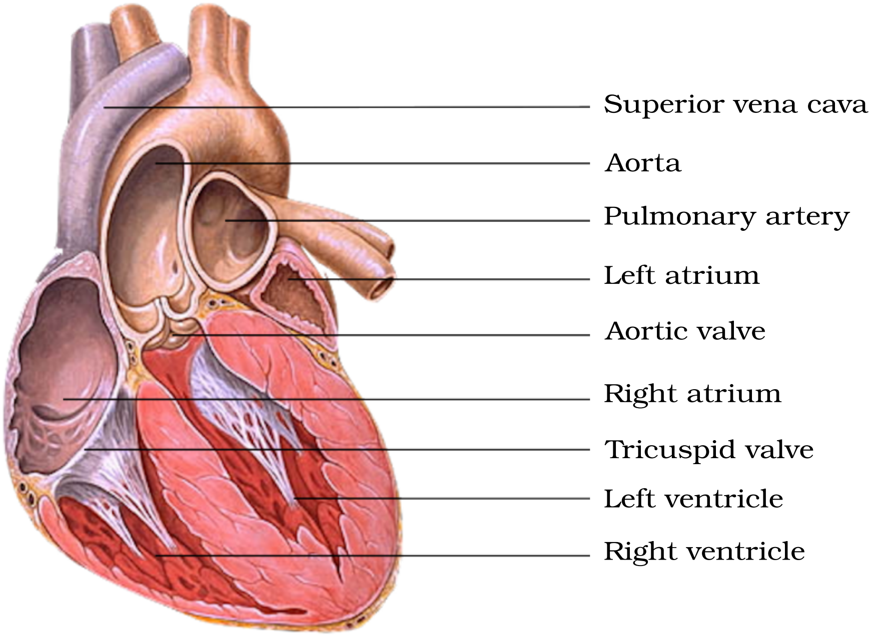

Figure 2.1. Cross section of the human heart; showing both atria and ventricles with corresponding valves, major veins and arteries, and cardiac muscle [70, modified].

Oxygenated blood re-enters the heart via the *pulmonary vein* into the *left atrium* , which then passes through the *mitral valve* into the *left ventricle*. From the left ventricle, blood is pumped via the *aorta* into the *systemic circulation* where the body is supplied with oxygenated blood which then returns back to the heart. [58]

The atria develop significantly lower pressures than do the ventricles, and consequently contain thinner walls of cardiac muscle, known as the *myocardium* shown in Figure 2.2, which is supplied by four major arteries. The left ventricle, whose cavity resembles the shape of a cone, has approximately three times the mass and twice the thickness of the right ventricle, and may be thought of as a pressure pump [58]. In a healthy human heart, peak *systolic* pressure is normally three times higher than that of the right ventricle, which is shaped like a crescent.

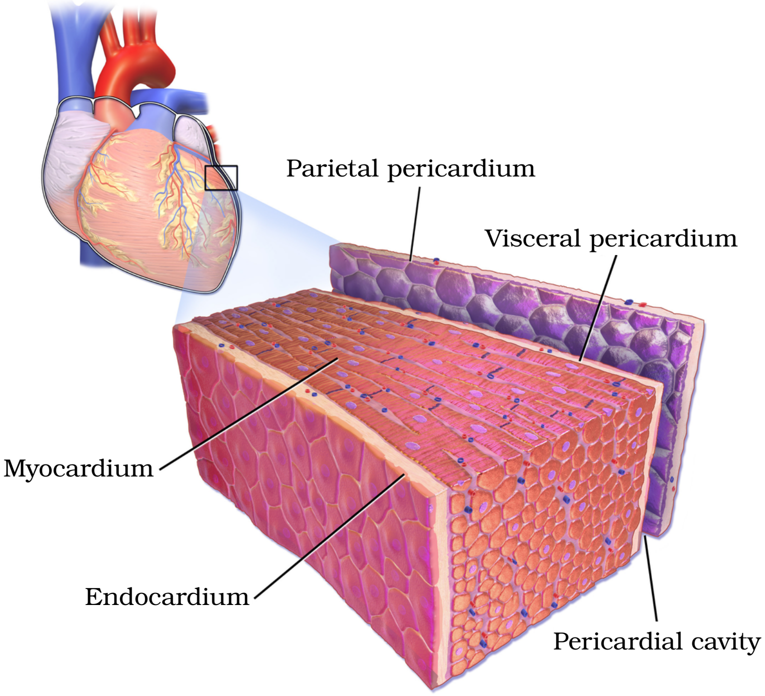

Figure 2.2. Layers of the wall of the heart; showing the epicardium as the visceral pericardium, the thick layer of the myocardium and the endocardium in relation to to the heart itself [78, modified].

Along with a small amount of fluid, the heart is contained within a fibrous sac called the *pericardium*, which has a continuous inner surface with the *epicardium*. The *endocardium*, a thin layer of connective tissue, lines the cavities of the atria and ventricles. Because the heart is contained within the rigid pericardium, the ventricles interact with one another. The muscular walls of the ventricles consist of overlapping fibre bundles, which follow spiral paths as they sweep from the base of the heart to its apex. [58]

2.2 Cardiac muscle

The myocardium, which makes up a vast majority of the heart wall's thickness, is composed of cells called *cardiomyocytes* and connective tissue. Cardiomyocytes shown in Figure 2.4 represent most of the myocardial mass [42], however, approximately 70% of the cardiac cells are smaller non-myocytes which secrete and maintain the connective tissue fibres which contribute to the tensile strength and stiffness of the heart. Several types of cardiomyocytes are found in the human heart including *working cardiomyocytes*, specialised for contraction, which are found in the atria and ventricles. These myocytes are filled with cross-striated *myofibrils* and make up almost half of the volume of the working cardiomyocytes. Most of the remaining volume is occupied by *mitochondria* which generate the large amount of energy required for contraction [58]. *Sarcomeres*, the functional contractile unit of cardiomyocytes form a parallel arrangement of thick filaments of *myosin* that slide along thick filaments of *actin*, illustrated in Figure 2.3. [58]

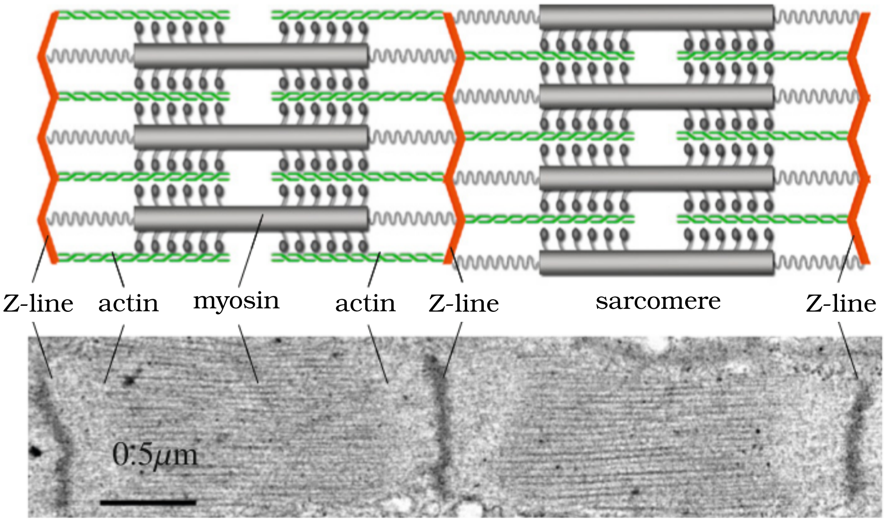

Figure 2.3. Sarcomere units of a cardiomyocyte; sarcomeres are defined as the segment between two neighbouring Z-lines, shown in orange. Healthy sarcomeres are 1.9-2.1 μm in length and are characterized by a parallel arrangement of thick filaments of myosin, displayed in grey, sliding along thin filaments of actin, labelled in green. Although cardiac cells are known to change length and thickness in response to mechanical loading, the individual sarcomeres maintain an optimal resting length [43, modified].

The connective tissue framework, shown in Figure 2.5, is organised into the *endomysium* which surrounds individual cardiomyocytes, the *perimysium* which supports groups of cardiomyocytes and the *epimysium* which encases the entire muscle. *Intercalated discs*, shown in Figure 2.4, represent specialised cell-to-cell junctions that form strong mechanical linkages between cells; important to maintain cell linkages during contraction [58].

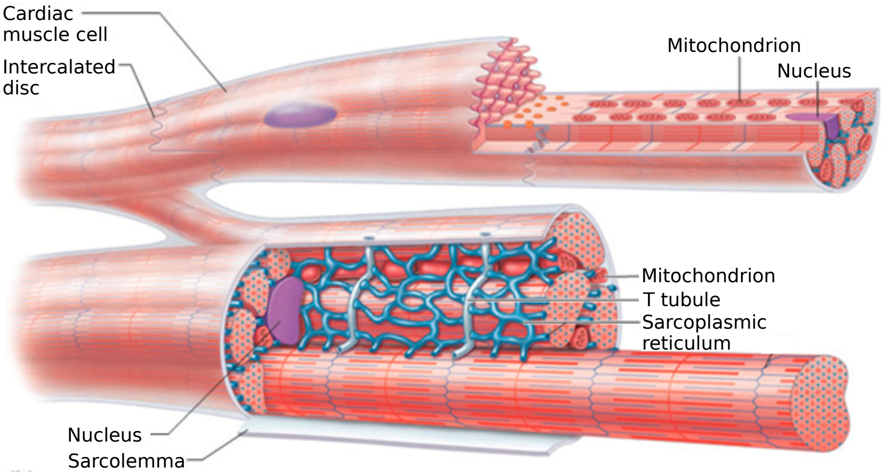

Figure 2.4. Microscopic anatomy of a cardiomyocyte; showing mitochondria, intercalated discs and myofibrils running along the muscle orthogonal to the intercalated discs [54].

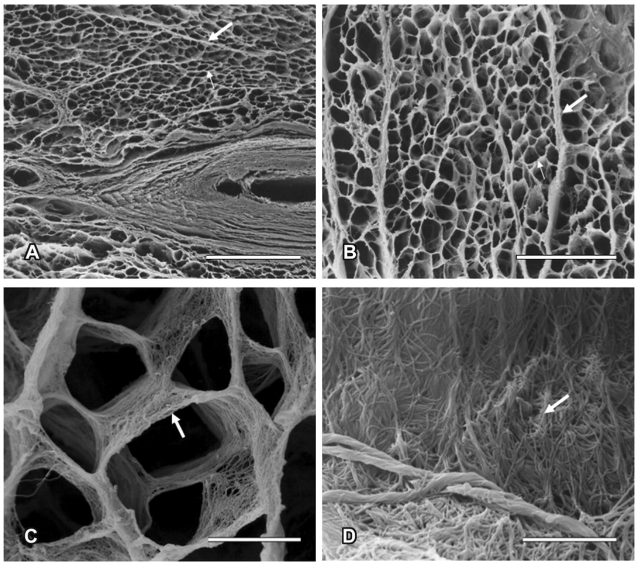

Figure 2.5. Micro-scale connective tissue skeleton of the human heart (transverse section). **A**: The collagen network around cardiomyocytes and small vessels is clearly observed (thick arrow, perimysium; thin arrow, endomysium). **B**: The interstitial connective tissue consisting of perimysial and endomysial components presents a honeycomb shape. The perimysium (thick arrow) surrounds groups of cardiomyocytes, and the endomysium (thin arrow) surrounds each cardiomyocyte. **C**: The endomysium supports and connects individual cardiomyocyte fascicles. **D**: At higher magnification, collagen fibres show interconnections on the surface of cardiomyocytes [57].

The muscle fibres of a cardiomyocyte are arranged in transmural layers which are organised helically around the heart, spiralling from the apex to the base, resulting in an orthotropic behaviour of the heart [99]. This architecture is illustrated in Figure 2.6 in terms of the fibre direction $\mathbf{f}_0$, sheet plane vector $\mathbf{s}_0$ and the normal vector to the sheet plane $\mathbf{n}_0$. [42]

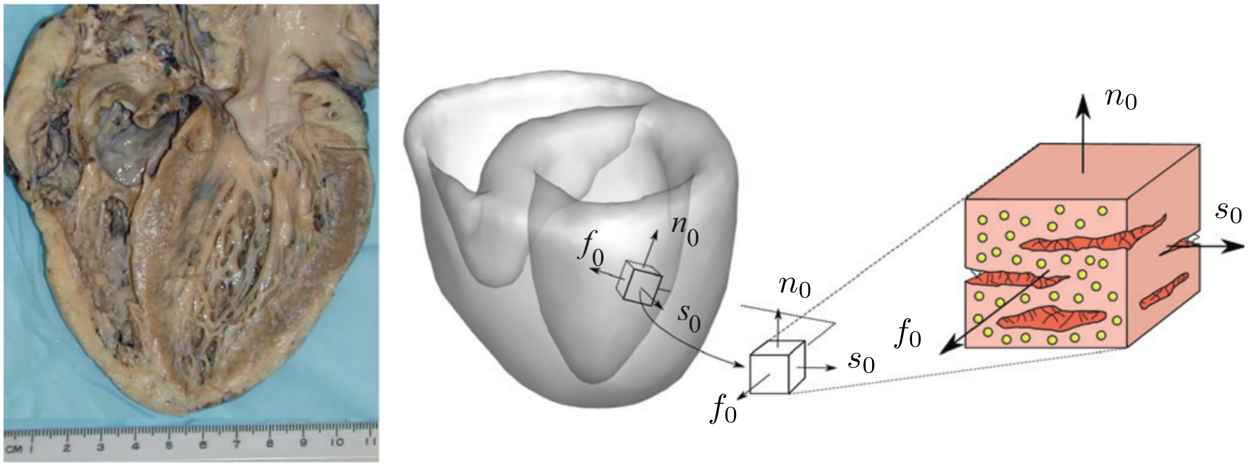

Figure 2.6. Normal healthy heart (left). Micro-structural architecture of the heart (right). The orthogonal unit vectors $\mathbf{f}_0$ and $\mathbf{s}_0$ designate the muscle fibre direction and the sheet plane vector in the undeformed configuration. The orthogonal vector $\mathbf{n}_0$ completes the local coordinate system, where the constitutive response of the heart is typically viewed as orthotropic. [42, modified]

2.3 Rheumatic heart disease

Rheumatic heart disease (RHD) results from an immune response after exposure to *Streptococcus pyogenes*, classified as a group A streptococcus, generally in the form of a throat infection [72]. Acute rheumatic fever (ARF) is the precursor to RHD and manifests itself as a combination of *inter alia* fever, carditis and arthritis usually about three weeks after an infection with a group A streptococcus bacteria and most often affects children, adolescents and young adults. The peak incidence of ARF is in children aged 5-14 years. Carditis (an inflammation of the heart or its surroundings) occurs a few weeks after initial infection in about 50% of patients, and presents as valvulitis sometimes combined with pericarditis or myocarditis. [72]

Patients are often diagnosed with RHD after a known infection of ARF, however it is possible to be diagnosed with RHD without a known infection, and often present 20-50 years after initial infection with a shortness of breath [72]. Most commonly, patients present with aortic or mitral regurgitation or stenosis. Regurgitation is a condition in which the valves are unable to prevent blood leaving the ventricle during ventricular contraction as a result of scarring of the heart valve tissue, whereas stenosis is a narrowing of the valves causing hindered blood flow, see Figure 2.7. Due to regurgitation and stenosis, a reduced pumping capacity of the heart is caused, leading to hypertrophy [1] of the ventricular cavities as a means of compensation for this reduced capacity.

In the case of ventricular pressure overload, the left ventricle experiences an increase in resistance as it ejects blood into the aorta (after-load increase). Common causes of left ventricular pressure overload are systemic hypertension or aortic stenosis to which the ventricles typically react by concentric hypertrophic growth, characterized by thickening of the wall associated

---

[1] Including eccentric and concentric.

with cardiac cell thickening when sarcomeres are added in parallel [41, 80]. In volume overload, the heart experiences an increase in filling, or pre-load. Following ventricular volume overload (caused by for example a regurgitant mitral valve) eccentric hypertrophy ensues as cardiac cells grow axially by adding sarcomeres in series [41, 80]. In such a case, a condition termed dilated cardiomyopathy (DCM) may develop, whereby the volume of the heart increases, but the amount of blood pumped during the cardiac cycle decreases [40], for which it has been show that mitral valve regurgitation is a cause which affects the diastolic function of the heart [112].

The cytoskeleton (cf. Figure 2.5) is responsible for creating a support and communication network for the cardiomyocyte constituents, and helps the heart adapt its architecture in response to cell deformation and changes in mechanical stress by modifying the size, shape and composition of the heart, known as *hypertrophy* in the case of an increase in size and volume [47]. Hypertrophy thus explains the compensation mechanism in response to a reduced pumping capacity due to regurgitation or stenosis [41].

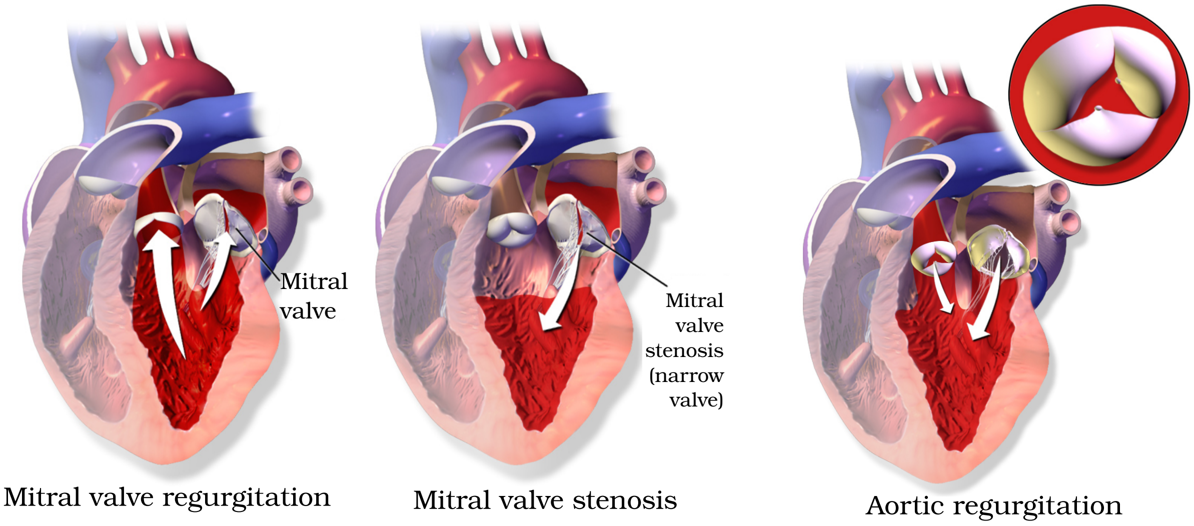

Figure 2.7. Common types of vulvular disease associated with RHD [78, modified]: From left to right, **mitral valve regurgitation** showing an inability of the valve to prevent flow of blood back into the left atrium; **mitral valve stenosis** showing a hindrance of flow into the left ventricle due to narrowing; **aortic regurgitation** showing a back flow of blood from the aorta into the left ventricle. All three conditions result in a weakened pumping capacity of the heart.

With specific reference to Figure 2.8, one can see that in order to study the mechanical processes involved with RHD, a model which has the ability to predict growth and remodelling of cardiac muscle is required. Furthermore, with reference to Figure 2.5, in order to obtain an accurate description of the cardiac tissue framework, it is advantageous to take into account that the microstructure is a multiphasic porous network of collagen fibres and connective tissue, saturated with a liquid medium (blood).

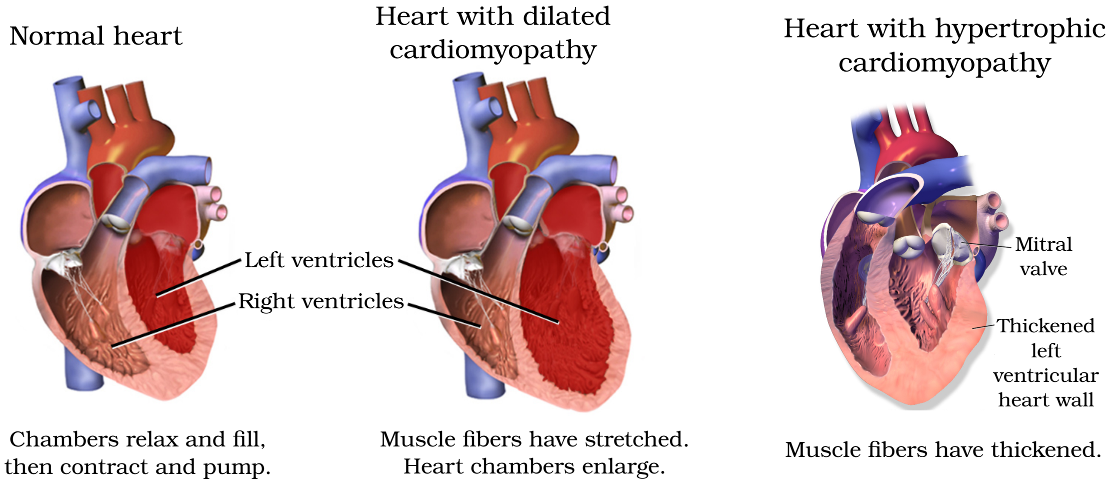

Figure 2.8. Normal heart versus diseased heart affected by cardiomyopathy: A normal heart is presented with healthy chambers (left), and is compared to a dilated heart in which muscle fibres have stretched and the heart cavity is dilated (middle). A hypertrophic heart is shown, where significant thickening of the myocardium is seen (right) [78, modified].

Chapter 3

Porous media theory

3.1 Introduction

In the field of biomechanics, it is common to deal with structures which are composed of two or more materials with differing phases and mechanical properties. One commonly used approach to describe the behaviour of such materials is to assume homogeneity in terms of behaviour and phase, and utilise specialised constant parameters within the constitutive relations in order to describe the behaviour of the overall medium. In terms of the familiar materials such as dense concrete and steel, wherein few pores containing a second phase are to be found, this approach has proven to be very effective. However, in the case of organic tissues, there generally exists a considerable amount of at least two phases (tissue and blood), wherein the existence of pores within the solid matrix is not minor and is not able to be ignored, along with a permeability of the tissue walls which causes a change in tissue behaviour depending on its state of deformation. To further complicate matters, biological tissues are well known for their ability to change in size/geometry and microstructure, of which the changes may be categorised as growth and remodelling respectively. As such, a second approach, the Theory of Porous Media (TPM) is employed, which has proved to be effective in this regard. The strongest case for the use of TPM is thus its ability to separate the behaviour of various phases, and account for a transfer of mass between these. The basics of TPM, which is based on Mixture Theory (cf. Atkin and Crain [9]), are the volume fraction concept, the saturation condition, the kinematics, balance equations and entropy inequality in the process of deriving thermodynamically consistent constitutive relations, for which detailed explanations are described by *inter alia* Drumheller [32], Bowen [18, 19], de Boer [27, 28], Ehlers [33] and Bluhm [17].

Taking into account the different material properties, motions and the associated interactions between the phases inevitably leads to a more complex description of the behaviour. Additionally, if one desires a phase separation, at least a basic description of the micro-scale is required. In order to achieve this, the theory of mixtures is employed, along with the concept of volume fractions, with which the micro-scale is touched upon. With the use of this approach, a "smeared" substitute continua results in reduced densities for the constituents, whereby the quantities at the micro-scale are averaged and substituted for by quantities on the macro-scale. As such, thermodynamical investigation and derivation can continue on the micro-scale avoiding the formalism connected with a true micro-scale investigation. Of course, in the past few years, the description of the micro-scale has been taken into account via the FE^2 method (cf. Feyel [39] and Schröder [91] and the references within) and a coupling of porous media theory with this method (see Bartel et al. [12, 13]), which at this point in the progress of the method proves to be extremely computationally demanding (cf. Feyel [38]) for the purposes of this investigation.

As mentioned by de Boer [28], the problem of analysis at the macroscopic level, is the closure problem. In any biphasic or triphasic model, it can be easily shown that for a medium consisting of κ constituents, only $\kappa - 1$ field equations are available. With the use of the volume fraction concept, this problem is addressed.

In the following sections, the underlying ideas of the proposed theory will be presented. Furthermore, the formulations of de Boer [27], Krause [63], Ricken and Bluhm [85], Ricken et al. [86] and Ricken [84] will be closely followed.

3.2 Volume faction concept

Within the framework of TPM, consider a porous material composed of κ constituents which has as its control space the porous solid, with the fluid contained within its pores able to freely leave or enter the control space. It is assumed that the pores are distributed in a statistical manner and that any volume element in the reference, intermediate or actual configuration is composed of the volume elements of the real constituents. That is, any whole volume element is composed of fractions of its multi-phasic parts, under the assumption that the whole control space is simultaneously and wholly occupied by the individual constituents to various degrees or fractions, whereby only the liquids or gases contained within the pores can leave the control space. This basis of the description of TPM makes use of elements of the theory of mixtures, restricted by the volume fraction concept and is the model of the macroscopic body, in which neither the microscopic interpretation of the pore structure nor the exact location of the individual constituents is required to be known. As such, all quantities relating to the individual phases such as motion, stress and deformation are defined as statistically averaged values of the quantities which make up the control space (cf. de Boer [27]).

The porous material, which is composed of a solid phase φ^{S} saturated by a fluid phase φ^{F} is bound by the control space $\mathrm{B}_{0\mathrm{S}}$ and surface $\partial\mathrm{B}_{0\mathrm{S}}$ in the reference configuration at time $\mathrm{t} = \mathrm{t}_0$ and the control space B_{S} and surface $\partial\mathrm{B}_{\mathrm{S}}$ in the actual configuration at time t. Furthermore, at time t, an intermediate configuration is defined with the control space B_{sg} and surface $\partial\mathrm{B}_{\mathrm{sg}}$, in analogy with Ateshian and Ricken [8] and Werner et al. [107], which takes into account that a change in volume and density occurs during the growth process.

The average quantities of the control spaces and contained fluid are obtained via a volume averaging approach, in which the macroscopic quantities are obtained from the microscopic (cf. Didwania and de Boer [29] and the references within in which the change of volume fractions associated with the micro scale are described by a further split of the solid deformation gradient via a multiplicative decomposition).

In the reference configuration, at the position X_α and the place $\mathbf{X}_\alpha$, for each constituent φ^α the volume fraction is postulated as

$$\mathrm{n}^\alpha_{0\alpha} = \mathrm{n}^\alpha_{0\alpha}\,(\,\mathbf{X}_\alpha,\,\mathrm{t} = \mathrm{t}_0\,) \tag{3.1}$$

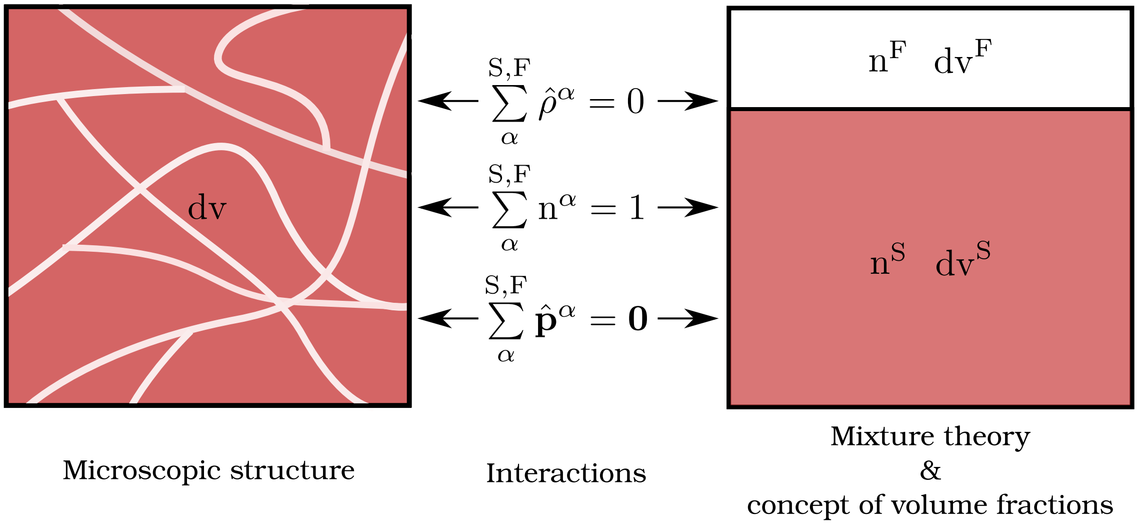

Figure 3.1. Volume fraction concept; showing the relation between the microscopic structure and the representative volume element (RVE) with volume dv. With the concept of volume fractions, the RVE is composed of dv^{F} and dv^{S}, represented by the fluid and solid volume fractions n^{F} and n^{S} respectively. The elements are related via the interactions in which $\hat{\rho}^\alpha$ is the mass supply, n^α are the respective volume fractions, and $\hat{\mathbf{p}}^\alpha$ are the interaction forces such as friction. [87, reproduced and adapted]

which relates the partial volume elements $\mathrm{dV}_{0\alpha}$ to the real volume element $\mathrm{dV}_{0\alpha}^{\alpha}$, for the constituent φ^α (superscript index) in the reference placement at the position $\mathbf{X}_\alpha$ (subscript index). As such, a partial volume V_0^α of φ^α is defined as

$$\mathrm{V}_0^\alpha = \int_{\mathrm{B}_{0\mathrm{S}}} \mathrm{n}_{0\alpha}^\alpha \, \mathrm{dV}_{0\alpha} = \int_{\mathrm{B}_{0\mathrm{S}}} \mathrm{dV}_{0\alpha}^\alpha \,, \tag{3.2}$$

Under consideration of eq. (3.1) and eq. (3.2), the total volume of the control space is defined by

$$\mathrm{V}_0 = \int_{\mathrm{B}_{0\mathrm{S}}} \mathrm{dV}_{0\alpha} = \sum_{\alpha=1}^{\kappa} \mathrm{V}_0^\alpha = \int_{\mathrm{B}_{0\mathrm{S}}} \sum_{\alpha=1}^{\kappa} \mathrm{dV}_{0\alpha}^\alpha = \int_{\mathrm{B}_{0\mathrm{S}}} \sum_{\alpha=1}^{\kappa} \mathrm{n}_{0\alpha}^\alpha \, \mathrm{dV}_{0\alpha} \,. \tag{3.3}$$

In order to obtain a realistic volume, it follows that the volume fractions must satisfy the local statement

$$\sum_{\alpha=1}^{\kappa} \mathrm{n}_{0\alpha}^\alpha = 1 \tag{3.4}$$

at every point in the control space $\mathrm{B}_{0\mathrm{S}}$. It is clear that eq. (3.4) is a constraint placed on the volume fractions of the respective volume elements and is termed the saturation condition in the reference configuration, with which the assumption that the porous body is wholly occupied by the individual constituents is made clear. The volume fraction of each constituent φ^α is thus the amount of the volume element which is occupied in the case of this investigation by a specific phase $\alpha \in \{\mathrm{S}, \mathrm{F}\}$ at a certain point in time, where the total fraction of volume occupied must be unity. In the intermediate configuration, the volume fraction is defined as

$$\mathrm{n}_{\mathrm{g}}^{\alpha} = \mathrm{n}_{\mathrm{g}}^{\alpha}\,(\,\mathbf{x}_{\mathrm{g}}\,,\mathrm{t}\,) \tag{3.5}$$

at the position x_{g} and place $\mathbf{x}_{\mathrm{g}}$, where the principle of superposition leads to the case that $\mathrm{x}_{\mathrm{sg}} = \mathrm{x}_{\mathrm{fg}} = \mathrm{x}_{\mathrm{g}}$ and $\mathbf{x}_{\mathrm{sg}} = \mathbf{x}_{\mathrm{fg}} = \mathbf{x}_{\mathrm{g}}$. With the use of eq. (3.5), the partial volume of each constituent in the reference configuration is obtained via

$$\mathrm{V}_{\mathrm{g}}^{\alpha} = \int\limits_{\mathrm{B}_{\mathrm{Sg}}} \mathrm{n}_{\mathrm{g}}^{\alpha}\,\mathrm{dv}_{\mathrm{g}}, \tag{3.6}$$

where the relation for each partial volume element

$$\mathrm{dv}_{\mathrm{g}}^{\alpha} = \mathrm{n}_{\mathrm{g}}^{\alpha}\,\mathrm{dv}_{\mathrm{g}} \tag{3.7}$$

has been used. Subsequently, the volume of the body in the intermediate configuration is defined as

$$\mathrm{V}_{\mathrm{g}} = \int\limits_{\mathrm{B}_{\mathrm{Sg}}} \mathrm{dv}_{\mathrm{g}} = \sum_{\alpha=1}^{\kappa} \mathrm{V}_{\mathrm{g}}^{\alpha} = \int\limits_{\mathrm{B}_{\mathrm{Sg}}} \sum_{\alpha=1}^{\kappa} \mathrm{dv}_{\mathrm{g}}^{\alpha} = \int\limits_{\mathrm{B}_{\mathrm{Sg}}} \sum_{\alpha=1}^{\kappa} \mathrm{n}_{\mathrm{g}}^{\alpha}\,\mathrm{dv}_{\mathrm{g}}. \tag{3.8}$$

Furthermore, the volume fraction in the actual configuration is defined as

$$\mathrm{n}^{\alpha} = \mathrm{n}^{\alpha}\,(\,\mathbf{x}\,,\mathrm{t}\,) \tag{3.9}$$

at the position x at the place $\mathbf{x}$, where the principle of superposition has once again been applied. The partial volume therefore follows as

$$\mathrm{V}^{\alpha} = \int\limits_{\mathrm{B}_{\mathrm{S}}} \mathrm{n}^{\alpha}\,\mathrm{dv} \tag{3.10}$$

where the partial control volume is described in the control space noting that $\mathrm{dv} = \mathrm{dv}\,(\mathbf{x}, \mathrm{t})$ and making use of the volume fraction is the actual configuration as

$$\mathrm{dv}^{\alpha} = \mathrm{n}^{\alpha}\,\mathrm{dv}. \tag{3.11}$$

The total volume of the control space B_{S} with the surface $\partial\mathrm{B}_{\mathrm{S}}$ is thus described as

$$\mathrm{V} = \int\limits_{\mathrm{B}_{\mathrm{S}}} \mathrm{dv} = \sum_{\alpha=1}^{\kappa} \mathrm{V}^{\alpha} = \int\limits_{\mathrm{B}_{\mathrm{S}}} \sum_{\alpha=1}^{\kappa} \mathrm{dv}^{\alpha} = \int\limits_{\mathrm{B}_{\mathrm{S}}} \sum_{\alpha=1}^{\kappa} \mathrm{n}^{\alpha}\,\mathrm{dv}. \tag{3.12}$$

Along with eq. (3.12), the saturation condition in the actual configuration must be satisfied as

$$\sum_{\alpha=1}^{\kappa} \mathrm{n}^{\alpha} = 1 \tag{3.13}$$

Following the concept of volume fractions, it is clear that the density of the volume element is required to be addressed, which is introduced as the effective density. Following such, it is possible to couple the balance equations of mixture theory, and the volume fractions and saturation can be determined. For the total number of constituents κ, the mass in the reference configuration with respect to $\mathrm{B_{0S}}$ is determined by

$$\mathrm{M_0} = \sum_{\alpha=1}^{\kappa} \mathrm{M}_0^\alpha = \int_{\mathrm{B_{0S}}} \sum_{\alpha=1}^{\kappa} \rho_{0\alpha}^\alpha \, \mathrm{dV}_{0\alpha}, \tag{3.14}$$

in the intermediate configuration with respect to $\mathrm{B_{sg}}$ as

$$\mathrm{M_g} = \sum_{\alpha=1}^{\kappa} \mathrm{M}_\mathrm{g}^\alpha = \int_{\mathrm{B_{Sg}}} \sum_{\alpha=1}^{\kappa} \rho_\mathrm{g}^\alpha \, \mathrm{dv_g} \tag{3.15}$$

and in the actual configuration with respect to $\mathrm{B_S}$ as

$$\mathrm{M} = \sum_{\alpha=1}^{\kappa} \mathrm{M}^\alpha = \int_{\mathrm{B_S}} \sum_{\alpha=1}^{\kappa} \rho^\alpha \, \mathrm{dv}. \tag{3.16}$$

In eq. (3.14), the partial density in the reference configuration at the point $\mathbf{X}_\mathrm{S}$ is defined as

$$\rho_{0\alpha}^\alpha = \rho_{0\alpha}^\alpha \, (\mathbf{X}_\alpha, \, \mathrm{t} = \mathrm{t}_0), \tag{3.17}$$

and similarly in eq. (3.15) at the point $\mathbf{x}_\mathrm{g}$ the partial density in the intermediate configuration is defined as

$$\rho_\mathrm{g}^\alpha = \rho_\mathrm{g}^\alpha \, (\mathbf{x}_\mathrm{g}, \, \mathrm{t}) \tag{3.18}$$

and subsequently in eq. (3.16) at the point $\mathbf{x}$ in the actual configuration the partial density is defined as

$$\rho^\alpha = \rho^\alpha \, (\mathbf{x}, \, \mathrm{t}). \tag{3.19}$$

With the use of the volume fractions, the relation between the real density and the partial density is obtained in the reference configuration via

$$\rho_{0\alpha}^{\alpha\mathrm{R}} = \rho_{0\alpha}^{\alpha\mathrm{R}} \, (\mathbf{X}_\alpha, \, \mathrm{t} = \mathrm{t}_0), \tag{3.20}$$

which relates to the partial volume element $\mathrm{dV}_{0\alpha}^\alpha$. In the intermediate configuration the realistic density relating to $\mathrm{dv}_\mathrm{g}^\alpha$ is defined as

$$\rho_\mathrm{g}^{\alpha\mathrm{R}} = \rho_\mathrm{g}^{\alpha\mathrm{R}} \, (\mathbf{x}_\mathrm{g}, \, \mathrm{t}) \tag{3.21}$$

and in the actual configuration the realistic density relating to dv^α is defined as

$$\rho^{\alpha\mathrm{R}} = \rho^{\alpha\mathrm{R}} \, (\mathbf{x}, \, \mathrm{t}). \tag{3.22}$$

With the concept of effective densities, it follows that an effective mass is to be introduced. Making use of eq. (3.20) - eq. (3.22) the partial mass of constituent φ^α is described in the reference configuration as

$$\mathrm{M}_0^\alpha = \int\limits_{\mathrm{B}_{0\mathrm{S}}} \rho_{0\alpha}^\alpha \, \mathrm{dV}_{0\alpha} = \int\limits_{\mathrm{B}_{0\mathrm{S}}} \rho_{0\alpha}^{\alpha\mathrm{R}} \, \mathrm{dV}_{0\alpha}^\alpha, \tag{3.23}$$

in the intermediate configuration as

$$\mathrm{M}_\mathrm{g}^\alpha = \int\limits_{\mathrm{B}_{\mathrm{Sg}}} \rho_\mathrm{g}^\alpha \, \mathrm{dv}_\mathrm{g} = \int\limits_{\mathrm{B}_{\mathrm{Sg}}} \rho_\mathrm{g}^{\alpha\mathrm{R}} \, \mathrm{dv}_\mathrm{g}^\alpha \tag{3.24}$$

and in the actual configuration as

$$\mathrm{M}^\alpha = \int\limits_{\mathrm{B}_\mathrm{S}} \rho^\alpha \, \mathrm{dv} = \int\limits_{\mathrm{B}_\mathrm{S}} \rho^{\alpha\mathrm{R}} \, \mathrm{dv}^\alpha. \tag{3.25}$$

From eq. (3.23) - eq. (3.25), the partial density in the reference configuration is defined as

$$\rho_{0\alpha}^\alpha = \mathrm{n}_{0\alpha}^\alpha \, \rho_{0\alpha}^{\alpha\mathrm{R}}, \tag{3.26}$$

in the intermediate configuration as

$$\rho_\mathrm{g}^\alpha = \mathrm{n}_\mathrm{g}^\alpha \, \rho_\mathrm{g}^{\alpha\mathrm{R}} \tag{3.27}$$

and in the actual configuration as

$$\rho^\alpha = \mathrm{n}^\alpha \, \rho^{\alpha\mathrm{R}}. \tag{3.28}$$

The realistic densities represent the true densities of the constituents at the macroscopic level, and in the case of an incompressible material where $\left\{\rho^{\alpha\mathrm{R}} = \rho_{0\alpha}^{\alpha\mathrm{R}} = \text{constant}\right\}$ the behaviour of the porous body is treated using the concept of volume fractions. Furthermore, in the case of incompressible solid and fluid constituents, compressibility of the porous body is accomplished via a change in pore space and therefore volume fractions.

3.3 Kinematics

The porous solid, saturated by the fluid, is represented as an immiscible mixture of the constituents φ^α with particles X^α in the reference configuration, with its own independent motion function

$$\mathbf{x} = \mathcal{X}_\alpha\left(\mathbf{X}_\alpha, \mathrm{t}\right), \qquad \mathbf{x}_\mathrm{g} = \mathcal{X}_{\mathrm{g}\alpha}\left(\mathbf{X}_\alpha, \mathrm{t}\right), \qquad \mathbf{X}_\alpha = \mathcal{X}_\alpha^{-1}\left(\mathbf{x}, \mathrm{t}\right) \tag{3.29}$$

where eq. $(3.29)_{1,2}$ represent the *Lagrangian* [1] description of motion generally applied to the solid fractions. The motion function $\mathcal{X}_\alpha$ is postulated to be unique and uniquely invertible at any time t. The existence of an inverse to eq. $(3.29)_{1,2}$ leads to the *Eulerian* [2] description of motion in eq. $(3.29)_3$ generally applied to the liquid fractions. With eq. $(3.29)_{1,2}$ and eq. $(3.29)_3$ the velocity and acceleration of a material point of a constituent φ^α are defined respectively as

$$\begin{aligned} \mathbf{x}'_\alpha &= \frac{\partial \mathcal{X}_\alpha\left(\mathbf{X}_\alpha, \mathrm{t}\right)}{\partial \mathrm{t}}, \qquad && \mathbf{v}_\alpha = \mathbf{x}'_\alpha = \mathbf{x}'_\alpha\left(\mathbf{x}, \mathrm{t}\right) \quad \text{and} \\ \mathbf{x}''_\alpha &= \frac{\partial^2 \mathcal{X}_\alpha\left(\mathbf{X}_\alpha, \mathrm{t}\right)}{\partial \mathrm{t}^2}, \qquad && \mathbf{a}_\alpha = \mathbf{x}''_\alpha = \mathbf{x}''_\alpha\left(\mathbf{x}, \mathrm{t}\right). \end{aligned} \tag{3.30}$$

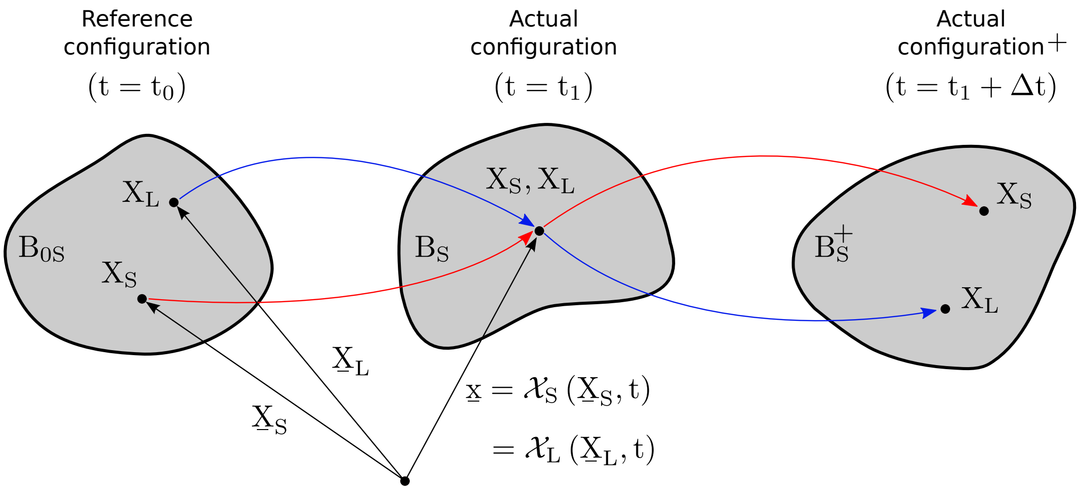

Figure 3.2. Motion of solid and fluid particle in a fluid saturated porous solid. In the reference configuration it is assumed that the solid and fluid particles are located via separate position vectors to allow for relative movement of solid and fluid constituents. Due to the principle of superposition of the balance equations, it is assumed that in the actual configuration the solid and fluid particles are both described by equal position vectors.

The Eulerian description of motion in eq. $(3.29)_3$ implies the existence of the non-singular *Jacobian*

$$\mathrm{J}_\alpha = \det \mathbf{F}_\alpha, \tag{3.31}$$

which has to differ from zero. Therein, $\mathbf{F}_\alpha$ denotes the deformation gradient tensor of the constituents φ^α, which is invertible. $\mathbf{F}_\alpha$ and its corresponding inverse $\mathbf{F}_\alpha^{-1}$ are defined as

$$\mathbf{F}_\alpha = \frac{\partial \mathbf{x}_\alpha}{\partial \mathbf{X}_\alpha} = \mathrm{Grad}_\alpha\, \mathcal{X}_\alpha \qquad \text{and} \qquad \mathbf{F}_\alpha^{-1} = \frac{\partial \mathbf{X}_\alpha}{\partial \mathbf{x}_\alpha} = \mathrm{grad}\, \mathbf{X}_\alpha \tag{3.32}$$

---

[1] Joseph-Louis Lagrange (1736-1813): Italian mathematician and astronomer, who was one of the 72 French scientists who were commemorated on plaques on the Eiffel Tower.

[2] Leonhard Euler (1707-1783): Swiss mathematician, physicist, astronomer, logician and engineer after who the Euler equations on fluid dynamics are named, and was the equivalent to doctoral advisor to Joseph-Louis Lagrange.

respectively, where the differential operator "$\text{Grad}_\alpha(\bullet)$" refers to a partial differentiation with respect to the reference position $\mathbf{X}_\alpha$ of the constituents φ^α and the differential operator "$\text{grad}(\bullet)$" refers to partial differentiation with respect to the spatial point $\mathbf{x}$. During deformation, $\mathbf{F}_\alpha$ is restricted to $\det \mathbf{F}_\alpha > 0$. Due to the postulation that the individual constituents are associated with different motions, a need arises for different material time derivatives. For a scalar field Γ depending on $\mathbf{x}$ and t, these are defined as

$$\Gamma'_\alpha = \frac{\partial \Gamma}{\partial \mathrm{t}} + \text{grad}\Gamma \cdot \mathbf{x}'_\alpha, \tag{3.33}$$

from which analogous material time derivatives for vector and tensor functions result. As such, the material velocity gradient is introduced as

$$(\mathbf{F}_\alpha)'_\alpha = \frac{\partial \mathbf{x}'_\alpha}{\partial \mathbf{X}_\alpha} = \text{Grad}_\alpha\, \mathbf{x}'_\alpha. \tag{3.34}$$

The spatial velocity gradient is defined as

$$\mathbf{L}_\alpha = (\text{Grad}\ \mathbf{x}'_\alpha)\, \mathbf{F}_\alpha^{-1} = \text{grad}\ \mathbf{x}'_\alpha, \tag{3.35}$$

which is additively decomposed into symmetric and skew-symmetric parts

$$\mathbf{L}_\alpha = \mathbf{D}_\alpha + \mathbf{W}_\alpha \tag{3.36}$$

which are defined as

$$\mathbf{D}_\alpha = \frac{1}{2}\left(\mathbf{L}_\alpha + \mathbf{L}_\alpha^{\mathrm{T}}\right) \qquad \text{and} \qquad \mathbf{W}_\alpha = \frac{1}{2}\left(\mathbf{L}_\alpha - \mathbf{L}_\alpha^{\mathrm{T}}\right) \tag{3.37}$$

respectively, where the superscript "T" denotes tensor transposition. The right and left *Cauchy* [3]-*Green* [4] deformation tensors are defined as

$$\mathbf{C}_{\mathrm{S}} = \mathbf{F}_{\mathrm{S}}^{\mathrm{T}}\mathbf{F}_{\mathrm{S}} \qquad \text{and} \qquad \mathbf{B}_{\mathrm{S}} = \mathbf{F}_{\mathrm{S}}\mathbf{F}_{\mathrm{S}}^{\mathrm{T}} \tag{3.38}$$

respectively, and subsequently the *Green* strain tensor as

$$\mathbf{E}_{\mathrm{S}} = \frac{1}{2}\left(\mathbf{C}_{\mathrm{S}} - \mathbf{1}\right) = \frac{1}{2}\left(\mathbf{F}_{\mathrm{S}}^{\mathrm{T}}\mathbf{F}_{\mathrm{S}} - \mathbf{1}\right). \tag{3.39}$$

3.4 Kinematics of finite growth

As growth occurs over time, the classical concept of the reference configuration falls under scrutiny (cf. the arguments and works of Ambrosi et al. [3], Ateshian [6], Ateshian and Ricken [8], Klisch et al. [62], Rodriguez et al. [90], Volokh [101], Volokh and lev [102]), as it is no longer clear in what way the reference configuration is to be accurately and realistically

---

[3] Baron Cauchy (1789-1857): French mathematician and early pioneer of analysis, after whom sixteen concepts and theorems in elasticity are named, and whose name appears engraved on the south-east side of the Eiffel Tower in recognition of his contribution.

[4] George Green (1793-1841): British mathematical physicist, who was almost entirely self-taught, most known for his introduction of the concepts underlying Green's Theorem.

defined maintaining computational efficiency and ease of implementation. Multiple studies have been conducted by which an intermediate configuration resulting from growth is included, in which some have updated the reference configuration at each time step to be the previous intermediate configuration, such that growth results in a stress free state of newly deposited material (cf. [8]). In the case of this work, the concept of an incompatible growth configuration is made use of by which the reference configuration at time $t = 0$ is maintained. However, with the use of an intermediate configuration to capture the effects of growth without an influence on the stress, the concept of split kinematics is adopted much the same as Göktepe et al. [42].

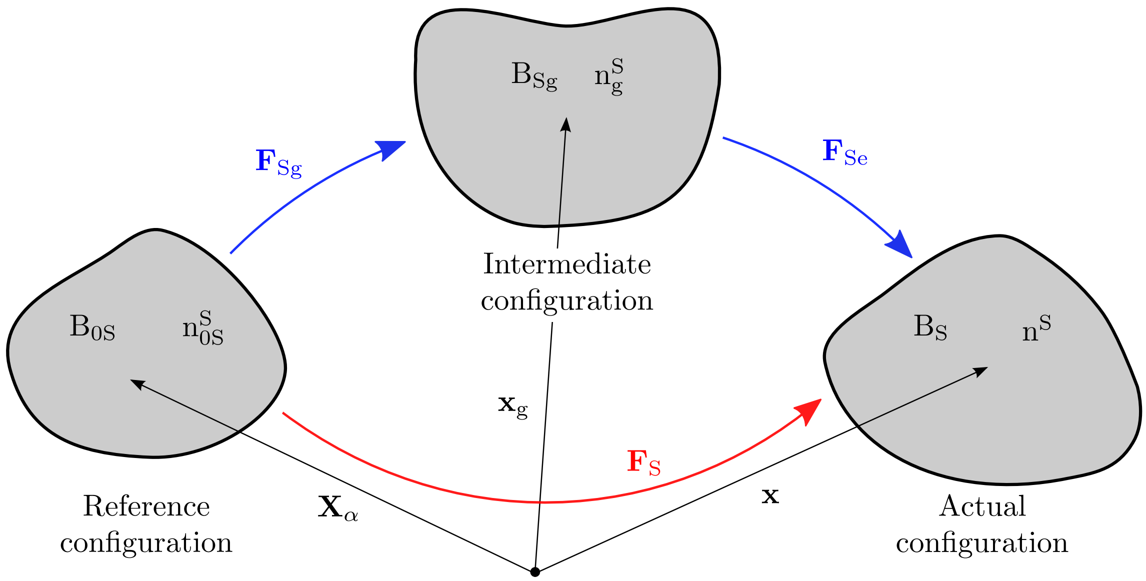

Figure 3.3. Kinematics of finite growth showing the multiplicative split of the deformation gradient, and the volume fractions. In the case of no growth, the intermediate and reference configurations coincide.

The fundamental key kinematic assumption of finite growth is the multiplicative decomposition of the deformation gradient $\mathbf{F}_S$, relating to the solid, into its elastic and growth dependant parts namely $\mathbf{F}_{Se}$ and $\mathbf{F}_{Sg}$ respectively (see [90]):

$$\mathbf{F}_S = \mathbf{F}_{Se}\,\mathbf{F}_{Sg} \tag{3.40}$$

adopting a concept originally introduced in the context of finite elasto-plasticity first proposed by Lee [68]. Following the split of $\mathbf{F}_S$, the solid Jacobian J_S is multiplicatively split into its elastic parts J_{Se} and J_{Sg} respectively via

$$J_S = J_{Se} \cdot J_{Sg}. \tag{3.41}$$

In the literature, growth has been generally introduced into the kinematics via an internal iteration of the growth multiplier ϑ (see Göktepe et al. [42]), however, due to the additional degree of freedom n^S within the model, it proves more efficient to include the growth into the kinematics via the growth part of the Jacobian J_{Sg} via

$$\mathrm{J_{Sg}} = \frac{\rho^S_{0S} + \rho^L_{0L}}{\rho^S_g + \rho^L_g} = \frac{\mathrm{n^S_{0S}}(\rho^{\mathrm{SR}}_{\mathrm{0S}} - \rho^{\mathrm{LR}}_{\mathrm{0L}}) + \rho^{\mathrm{LR}}_{\mathrm{0L}}}{\mathrm{n^S_g}(\rho^{\mathrm{SR}}_{\mathrm{0S}} - \rho^{\mathrm{LR}}_{\mathrm{0L}}) + \rho^{\mathrm{LR}}_{\mathrm{0L}}} \qquad [107,\ 108] \tag{3.42}$$

wherein the growth part of the volume fraction in the intermediate configuration $\mathrm{n^S_g}$ is found using the relation

$$\mathrm{n^S_g} = \mathrm{n^S_{0S}} + \sum_{\mathrm{t=0}}^{\mathrm{t}} \frac{\hat{\rho}^{\mathrm{S}}}{\rho^{\mathrm{SR}}_{\mathrm{0S}}} \qquad [35] \tag{3.43}$$

in which the growth part of the volume fraction is determined from the mass supplied, making use of the relation $\hat{\mathrm{n}}^{\mathrm{S}} = \hat{\rho}^{\mathrm{S}}/\rho^{\mathrm{SR}}_{\mathrm{0S}}$ which is valid for the case of an incompressible solid phase where $\rho^{\mathrm{SR}} = \rho^{\mathrm{SR}}_{\mathrm{0S}}$. In the case of eccentric growth, the growth multiplier is introduced, which is smaller than one in the case of shrinkage, larger than one in the case of stretching and unity in the case of no growth. As introduced in Chapter 2, three orthonormal directions of the cardiomyocyte are defined. However, during eccentric growth, stretch is only observed to occur along the fibre direction $\mathbf{f}_0$, along which the growth multiplier ϑ^{f} ([42]) is applied and defined as:

$$\vartheta_{\mathrm{Sg}} = \mathrm{J}^{1/3}_{\mathrm{Sg}}. \qquad [107] \tag{3.44}$$

Due to the lack of causative evidence which links dilation to a stress overload, it is reasonable to define eccentric growth via a stretch-driven approach which has proven to be successful when used by Göktepe et al. [42], Kerckhoffs et al. [60]. As such, the total cardiomyocyte stretch ϵ is introduced via

$$\epsilon = \sqrt{\mathbf{f}_0 \cdot \mathbf{F}^{\mathrm{T}}_{\mathrm{S}} \cdot \mathbf{F}_{\mathrm{S}} \cdot \mathbf{f}_0} \tag{3.45}$$

which follows the multiplicative decomposition into its elastic and growth parts ϵ^{e} and ϵ^{g} respectively as

$$\epsilon = \epsilon^{\mathrm{e}}\epsilon^{\mathrm{g}} \tag{3.46}$$

which allows the definition of $\mathbf{F}_{\mathrm{Sg}}$ in terms of the eccentric cardiomyocyte stretch as

$$\mathbf{F}^{\mathrm{S}}_{\mathrm{g}} = \mathbf{1} + [\epsilon^{\mathrm{g}} - 1]\,\mathbf{M}_0 \qquad [42] \tag{3.47}$$

where the structural tensor $\mathbf{M}_0$ in the reference configuration is defined as

$$\mathbf{M}_0 = \mathbf{f}_0 \otimes \mathbf{f}_0. \tag{3.48}$$

Subsequently, the inverse of $\mathbf{F}_{\mathrm{Sg}}$ is explicitly obtained via the *Sherman-Morrison* formula as:

$$\mathbf{F}^{-1}_{\mathrm{Sg}} = \mathbf{1} - \frac{\epsilon^{\mathrm{g}} - 1}{\epsilon^{\mathrm{g}}}\mathbf{M}_0. \tag{3.49}$$

Making use of eq. (3.49), the elastic part of the deformation gradient $\mathbf{F}_{\mathrm{Se}}$ is obtained as

$$\mathbf{F}_{\mathrm{Se}} = \mathbf{F}_{\mathrm{S}}\,\mathbf{F}^{-1}_{\mathrm{Sg}}. \tag{3.50}$$

As such, the following relations for the split Jacobian are able to be obtained:

$$\mathrm{J}_{\mathrm{Se}} = \det \mathbf{F}_{\mathrm{Se}} \quad \text{and} \quad \mathrm{J}_{\mathrm{Sg}} = \det \mathbf{F}_{\mathrm{Sg}}. \tag{3.51}$$

In analogy to the split of the deformation gradient, the right and left *Cauchy-Green* deformation tensors $\mathbf{C}_{\mathrm{S}}$ and $\mathbf{B}_{\mathrm{S}}$ as defined in eq. (3.38) are multiplicatively split and the elastic parts $\mathbf{C}_{\mathrm{Se}}$ and $\mathbf{B}_{\mathrm{Se}}$ respectively are defined as:

$$\mathbf{C}_{\mathrm{Se}} = \mathbf{F}^{\mathrm{T}}_{\mathrm{Se}} \mathbf{F}_{\mathrm{Se}} , \qquad \mathbf{B}_{\mathrm{Se}} = \mathbf{F}_{\mathrm{Se}} \mathbf{F}^{\mathrm{T}}_{\mathrm{Se}}. \tag{3.52}$$

3.5 Balance equations

The balance equations for porous media are the additive balance equations of the constituents φ^α taken from mixture theory which yield the balance equations of mass, momentum, moment of momentum and energy in analogy to those of a one component continua. Therefore, it is required that the equations are established for each constituent [5], meaning that all quantities which influence φ^α including the interaction effects are considered within the balance equations for each φ^α. Following the analogy of the equations for a one component continua, the interaction effects are required to be introduced in a manner such that the summation of the balance equations for all constituents κ result in the balance equations for one material following superimposition, known as the third principle of *Truesdell* [7] (cf. Truesdell [97]), which includes the criteria that all interaction effects must sum to zero. For detailed discussion relating to the balance equations, the reader is referred to de Boer [28], from where the following theory has been summarised and in places elaborated upon.

The following balance equations are formulated in the local and global forms for each individual constituent taking into consideration the interaction effects.

3.5.1 Balance of mass

For individual constituents φ^α, the balance of mass requires that the rate of the mass M^α equals the mass which is supplied with

$$(\mathrm{M}^\alpha)'_\alpha = \int\limits_{\mathrm{B}_\alpha} \hat{\rho}^\alpha \, \mathrm{dv} \, , \tag{3.53}$$

where $\hat{\rho}^\alpha$ represents the local mass supply and

$$\mathrm{M}^\alpha = \int\limits_{\mathrm{B}_\alpha} \rho^\alpha \, \mathrm{dv} = \int\limits_{\mathrm{B}_\alpha} \rho^{\alpha\mathrm{R}} \, \mathrm{dv}^\alpha \tag{3.54}$$

---

[5] as called for by von Terzaghi [6] [103] which was the first book recognised worldwide as a substantial book on soil mechanics, along with a series of articles published in the English language - see [104].

[7] Clifford Truesdell (1919-2000): American mathematician, natural philosopher and historian of science, employed by the U.S. navy to conduct mechanics research, and founder and editor-in-chief of the journals *Archive for Rational Mechanics and Analysis* and *Archive for History of Exact Science*.

denotes the mass of the constituent. The local mass supply occurs as a result from exchange of mass from one constituent to another, which are both physically present at the point $\mathbf{x}$ at time t, and may occur due to phase transformation. Making use of the transport theorem

$$(\mathrm{dv})'_\alpha = \operatorname{div} \mathbf{x}'_\alpha \, \mathrm{dv} \tag{3.55}$$

the rate of mass leads to

$$(\mathrm{M}^\alpha)'_\alpha = \int\limits_{\mathrm{B}_\alpha} [(\rho^\alpha)'_\alpha + \rho^\alpha \operatorname{div} \mathbf{x}'_\alpha] \, \mathrm{dv} \,, \tag{3.56}$$

and the resulting balance of mass is given by

$$\int\limits_{\mathrm{B}_\alpha} [(\rho^\alpha)'_\alpha + \rho^\alpha \operatorname{div} \mathbf{x}'_\alpha] \, \mathrm{dv} = \int\limits_{\mathrm{B}_\alpha} \hat{\rho}^\alpha \, \mathrm{dv}. \tag{3.57}$$

In the local form, eq. (3.57) reads

$$(\rho^\alpha)'_\alpha + \rho^\alpha \operatorname{div} \mathbf{x}'_\alpha = \hat{\rho}^\alpha. \tag{3.58}$$

Following the third metaphysical principle of *Truesdell*, the summation of eq. (3.57) results in

$$\sum_{\alpha=1}^{\kappa} [\,(\rho^\alpha)'_\alpha + \rho^\alpha \operatorname{div} \mathbf{x}'_\alpha] = \sum_{\alpha=1}^{\kappa} \hat{\rho}^\alpha \overset{!}{=} 0 \tag{3.59}$$

which is only able to be fulfilled if

$$\sum_{\alpha=1}^{\kappa} \hat{\rho}^\alpha \overset{!}{=} 0\,. \tag{3.60}$$

In equation eq. (3.60), it is clear that mass gained by one constituent is as a direct result of an equal loss of another, resulting in a transfer of mass. For the special case where no mass exchange is present, eq. (3.58) can be integrated leading to the relation

$$\rho^\alpha = \rho^\alpha_{0\alpha} \mathrm{J}_\mathrm{S}^{-1}. \tag{3.61}$$

3.5.2 Balance of momentum

The balance equation of momentum states that the material time derivative of the momentum is equal to the sum of the external forces, leading to

$$(\mathbf{l}^\alpha)'_\alpha = \mathbf{k}^\alpha + \int\limits_{\mathrm{B}_\alpha} \hat{\mathbf{p}}^\alpha \, \mathrm{dv} \tag{3.62}$$

where the quantities

$$\mathbf{l}^\alpha = \int\limits_{\mathrm{B}_\alpha} \rho^\alpha\,\mathbf{x}'_\alpha\,\mathrm{dv} \tag{3.63}$$

and

$$\mathbf{k}^\alpha = \int\limits_{\mathrm{B}_\alpha} \rho^\alpha\,\mathbf{b}^\alpha\,\mathrm{dv} + \int\limits_{\partial\mathrm{B}_\alpha} \mathbf{t}^\alpha\,\mathrm{da} \tag{3.64}$$

describe the momentum and resulting external forces respectively. The external forces $\mathbf{k}^\alpha$ are given by the sum of the forces acting on the constituents as local volume forces $\rho^\alpha\mathbf{b}^\alpha$ which are integrated over the volume of the actual configuration, and the surface forces $\mathbf{t}^\alpha$, as well as the interaction forces $\hat{\mathbf{p}}^\alpha$ which also belong to the volume forces, with

$$\int\limits_{\partial\mathrm{B}_\alpha} \mathbf{t}^\alpha\,\mathrm{da} = \int\limits_{\partial\mathrm{B}_\alpha} \mathbf{T}^\alpha\,\mathbf{n}\,\mathrm{da} = \int\limits_{\partial\mathrm{B}_\alpha} \mathbf{T}^\alpha\,\mathrm{d}\mathbf{a}. \tag{3.65}$$

where $\mathbf{T}^\alpha$ denotes the *Cauchy* stress tensor, $\mathrm{d}\mathbf{a} = \mathbf{n}\,\mathrm{da}$ represents the outward pointing surface element in the actual placement and $\mathbf{n}$ is the outward pointing unit normal at the surface of the individual constituent body. The local supply term is given by the interaction force (such as friction):

$$\hat{\mathbf{p}}^\alpha = \hat{\mathbf{p}}^\alpha\,(\mathbf{x},\,\mathrm{t}). \tag{3.66}$$

Making use of the material time derivative of the momentum in the form

$$(\mathbf{l}^\alpha)'_\alpha = \int\limits_{\mathrm{B}_\alpha} (\rho^\alpha\,\mathbf{x}''_\alpha + \hat{\rho}^\alpha\,\mathbf{x}'_\alpha)\,\mathrm{dv} \tag{3.67}$$

and under consideration of the divergence theorem

$$\int\limits_{\partial\mathrm{B}_\alpha} \mathbf{T}^\alpha\,\mathbf{n}\,\mathrm{da} = \int\limits_{\mathrm{B}_\alpha} \mathrm{div}\,\mathbf{T}^\alpha\,\mathrm{dv}, \tag{3.68}$$

including eq. (3.63) and eq. (3.64), the balance equation of momentum reads

$$\int\limits_{\mathrm{B}_\alpha} (\rho^\alpha\,\mathbf{x}''_\alpha + \hat{\rho}^\alpha\,\mathbf{x}'_\alpha)\,\mathrm{dv} = \int\limits_{\mathrm{B}_\alpha} (\mathrm{div}\,\mathbf{T}^\alpha + \rho^\alpha\,\mathbf{b}^\alpha)\,\mathrm{dv} + \int\limits_{\mathrm{B}_\alpha} \hat{\mathbf{p}}^\alpha\,\mathrm{dv} \tag{3.69}$$

or in the local form

$$\mathrm{div}\,\mathbf{T}^\alpha + \rho^\alpha\,(\mathbf{b}^\alpha - \mathbf{x}''_\alpha) = \hat{\rho}^\alpha\,\mathbf{x}'_\alpha - \hat{\mathbf{p}}^\alpha\,. \tag{3.70}$$

In eq. (3.69), the expression $\hat{\rho}^\alpha\,\mathbf{x}'_\alpha$ represents the exchange of linear momentum as a result of a change in density due to a transfer of mass from one phase to another. For the mixture of the body, the balance of momentum can be obtained by the superimposition of the momentum of all κ constituents φ^α, assuming a common velocity $\mathbf{v}$ and acceleration $\mathbf{a}$, as well as a common external acceleration $\mathbf{b}$ for all φ^α:

$$\sum_{\alpha=1}^{\kappa} [\,\mathrm{div}\,\mathbf{T}^\alpha + \rho^\alpha\,(\mathbf{b}^\alpha - \mathbf{x}''_\alpha)\,] = \sum_{\alpha=1}^{\kappa} [\,\hat{\rho}^\alpha\,\mathbf{x}'_\alpha - \hat{\mathbf{p}}^\alpha\,]\,. \tag{3.71}$$

Taking into account the condition of the local conservation law for a one component body, the condition

$$\sum_{\alpha=1}^{\kappa} \hat{\mathbf{p}}^\alpha \overset{!}{=} \mathbf{0} \tag{3.72}$$

must once again be fulfilled. The local form of the balance of momentum therefore reads

$$\mathrm{div}\,\mathbf{T}^\alpha + \rho^\alpha\,(\mathbf{b}^\alpha - \mathbf{x}''_\alpha) = (\mathbf{l}^\alpha)'_\alpha. \tag{3.73}$$

3.5.3 Balance of moment of momentum

Under the assumption of non-polar materials, the balance of moment of momentum states that the material time derivative of the moment of momentum is equal to the moments of all forces, where the moments are referred to a fixed point 0:

$$(\mathbf{h}^\alpha_{(0)})'_\alpha = \mathbf{m}^\alpha_{(0)} + \hat{\mathbf{h}}^\alpha_{(0)} \tag{3.74}$$

where

$$\mathbf{h}^\alpha_{(0)} = \int\limits_{\mathrm{B}_\alpha} \mathbf{x} \times \rho^\alpha\,\mathbf{x}'_\alpha\,\mathrm{dv} \tag{3.75}$$

is the moment of momentum,

$$\mathbf{m}^\alpha_{(0)} = \int\limits_{\mathrm{B}_\alpha} \mathbf{x} \times \rho^\alpha\,\mathbf{b}^\alpha\,\mathrm{dv} + \int\limits_{\partial\mathrm{B}_\alpha} \mathbf{x} \times \mathbf{T}^\alpha\,\mathrm{d}\mathbf{a} \tag{3.76}$$

denotes the moment of external forces and

$$\hat{\mathbf{h}}^\alpha_{(0)} = \int\limits_{\mathrm{B}_\alpha} \mathbf{x} \times \hat{\mathbf{p}}^\alpha\,\mathrm{dv} \tag{3.77}$$

represents the moment which results from the interaction forces. From the material time derivative of the moment of momentum

$$(\mathbf{h}^\alpha_{(0)})'_\alpha = \int\limits_{\mathrm{B}_\alpha} \mathbf{x} \times (\,\rho^\alpha\,\mathbf{x}''_\alpha + \hat{\rho}^\alpha\,\mathbf{x}'_\alpha\,)\,\mathrm{dv} \tag{3.78}$$

and by application of the divergence theorem in the form

$$\int\limits_{\partial\mathrm{B}_\alpha} \mathbf{x} \times \mathbf{T}^\alpha\,\mathbf{n}\,\mathrm{da} = \int\limits_{\mathrm{B}_\alpha} (\,\mathbf{x} \times \mathrm{div}\,\mathbf{T}^\alpha + \mathbf{I} \times \mathbf{T}^\alpha\,)\,\mathrm{dv} \tag{3.79}$$

the balance of moment of momentum yields

$$\int_{\mathrm{B}_\alpha} \mathbf{x} \times (\, \rho^\alpha \, \mathbf{x}''_\alpha + \hat{\rho}^\alpha \, \mathbf{x}'_\alpha \,) = \int_{\mathrm{B}_\alpha} [\, \mathbf{x} \times (\, \mathrm{div}\, \mathbf{T}^\alpha + \rho^\alpha \, \mathbf{b}^\alpha) + \mathbf{I} \times \mathbf{T}^\alpha \,] \, \mathrm{dv} + \int_{\mathrm{B}_\alpha} \mathbf{x} \times \hat{\mathbf{p}}^\alpha \, \mathrm{dv} \tag{3.80}$$

or in the local form

$$\mathbf{x} \times [\, \mathrm{div}\, \mathbf{T}^\alpha + \rho^\alpha \, (\, \mathbf{b}^\alpha - \mathbf{x}''_\alpha \,) + \hat{\mathbf{p}}^\alpha - \hat{\rho}^\alpha \, \mathbf{x}'_\alpha \,] + \mathbf{I} \times \mathbf{T}^\alpha = \mathbf{0} \, . \tag{3.81}$$

Taking into consideration the local balance of momentum eq. (3.73), the local balance of the moment of momentum simplifies to

$$\mathbf{I} \times \mathbf{T}^\alpha = \mathbf{0} \tag{3.82}$$

which is fulfilled if the partial *Cauchy* stress tensor is symmetric:

$$\mathbf{T}^\alpha = (\mathbf{T}^\alpha)^{\mathrm{T}} \, . \tag{3.83}$$

Therefore, the result of evaluation of the balance of moment of momentum is that the stress tensor in this investigation is symmetric.

3.5.4 Balance of energy

The first law of thermodynamics, otherwise known as the balance of energy, is important to describe the thermo-mechanical effects of a material, in this case a multi-component material with effects such as phase transition. In the former case, it states that the sum of the material time derivatives of the internal and kinetic energies equals the rates of mechanical work and heat. Thus, a coupling is obtained between thermal fields such as temperature, heat flux and internal heat supply with mechanical fields such as motion, velocity, acceleration and deformation. When transferred to the individual constituents, the following balance of energy is obtained:

$$(\mathrm{E}^\alpha)'_\alpha + (\mathrm{K}^\alpha)'_\alpha = \mathrm{W}^\alpha + \mathrm{Q}^\alpha + \int_{\mathrm{B}_\alpha} \hat{\mathrm{e}}^\alpha \, \mathrm{dv} \tag{3.84}$$

where

$$\mathrm{E}^\alpha = \int_{\mathrm{B}_\alpha} \rho^\alpha \, \varepsilon^\alpha \, \mathrm{dv} \tag{3.85}$$

is the internal energy with the specific energy $\varepsilon^\alpha = \varepsilon^\alpha \, (\mathbf{x}, \mathrm{t})$ of the constituent φ^α,

$$\mathrm{K}^\alpha = \int_{\mathrm{B}_\alpha} \frac{1}{2} \, \rho^\alpha \, \mathbf{x}'_\alpha \cdot \mathbf{x}'_\alpha \, \mathrm{dv} \tag{3.86}$$

is the kinetic energy

$$\mathrm{W}^\alpha = \int\limits_{\mathrm{B}_\alpha} \mathbf{x}'_\alpha \cdot \rho^\alpha\, \mathbf{b}^\alpha\, \mathrm{dv} + \int\limits_{\partial \mathrm{B}_\alpha} \mathbf{x}'_\alpha \cdot \mathbf{T}^\alpha\, \mathrm{d}\mathbf{a} \tag{3.87}$$

is the increment of mechanical work and

$$\mathrm{Q}^\alpha = \int\limits_{\mathrm{B}_\alpha} \rho^\alpha\, \mathrm{r}^\alpha\, \mathrm{dv} + \int\limits_{\partial \mathrm{B}_\alpha} \mathbf{q}^\alpha \cdot \mathrm{d}\mathbf{a} \tag{3.88}$$

is the increment of non-mechanical work (rate of heat) with the partial energy source $\mathrm{r}^\alpha = \mathrm{r}^\alpha\,(\mathbf{x}, \mathrm{t})$ and the partial heat flux vector $\mathbf{q}^\alpha = \mathbf{q}^\alpha\,(\mathbf{x}, \mathbf{t})$, which is defined as positive when entering the body. The local energy supply of φ^α is represented by $\hat{\mathrm{e}}^\alpha$ which is caused by the remaining $\kappa - 1$ constituents. Taking into consideration the material time derivatives

$$(\mathrm{E}^\alpha)'_\alpha = \int\limits_{\mathrm{B}_\alpha} [\, \rho^\alpha\, (\varepsilon^\alpha)'_\alpha + \hat{\rho}^\alpha\, \varepsilon^\alpha\,]\, \mathrm{dv}\,, \qquad \text{and}$$

$$(\mathrm{K}^\alpha)'_\alpha = \int\limits_{\mathrm{B}_\alpha} (\, \rho^\alpha\, \mathbf{x}''_\alpha + \frac{1}{2}\hat{\rho}^\alpha\, \mathbf{x}'_\alpha\,) \cdot \mathbf{x}'_\alpha\, \mathrm{dv} \tag{3.89}$$

with the relations

$$\int\limits_{\partial \mathrm{B}_\alpha} \mathbf{x}'_\alpha \cdot \mathbf{T}^\alpha\, \mathbf{n}\, \mathrm{da} = \int\limits_{\mathrm{B}_\alpha} (\, \mathrm{div}\, \mathbf{T}^\alpha \cdot \mathbf{x}'_\alpha + \mathbf{T}^\alpha \cdot \mathbf{L}_\alpha\,)\, \mathrm{dv}\,, \qquad \text{and} \tag{3.90}$$

$$\int\limits_{\partial \mathrm{B}_\alpha} \mathbf{q}^\alpha \cdot \mathbf{n}\, \mathrm{da} = \int\limits_{\mathrm{B}_\alpha} \mathrm{div}\, \mathbf{q}^\alpha\, \mathrm{dv}\,, \tag{3.91}$$

the balance of energy is transformed to:

$$\begin{aligned} &\int\limits_{\mathrm{B}_\alpha} [\, \rho^\alpha\, (\varepsilon^\alpha)'_\alpha + \hat{\rho}^\alpha\, \varepsilon^\alpha\,]\, \mathrm{dv} + \int\limits_{\mathrm{B}_\alpha} (\, \rho^\alpha\, \mathbf{x}''_\alpha + \frac{1}{2}\, \hat{\rho}^\alpha\, \mathbf{x}'_\alpha\,) \cdot \mathbf{x}'_\alpha\, \mathrm{dv} \; = \\ &= \int\limits_{\mathrm{B}_\alpha} [\, (\, \mathrm{div}\, \mathbf{T}^\alpha + \rho^\alpha\, \mathbf{b}^\alpha\,) \cdot \mathbf{x}'_\alpha + \mathbf{T}^\alpha \cdot \mathbf{L}_\alpha\,]\, \mathrm{dv} \; + \int\limits_{\mathrm{B}_\alpha} (\rho^\alpha\, \mathrm{r}^\alpha - \mathrm{div}\, \mathbf{q}^\alpha\,)\, \mathrm{dv} + \int\limits_{\mathrm{B}_\alpha} \hat{\mathrm{e}}^\alpha\, \mathrm{dv}\,, \end{aligned} \tag{3.92}$$

or in the local form:

$$\begin{aligned} &\rho^\alpha\, (\varepsilon^\alpha)'_\alpha + \hat{\rho}^\alpha\, (\, \varepsilon^\alpha + \frac{1}{2}\, \mathbf{x}'_\alpha \cdot \mathbf{x}'_\alpha\,) = \\ &= [\, \mathrm{div}\, \mathbf{T}^\alpha + \rho^\alpha\, (\, \mathbf{b}^\alpha - \mathbf{x}''_\alpha\,)\,] \cdot \mathbf{x}'_\alpha + \mathbf{T}^\alpha \cdot \mathbf{L}_\alpha + \rho^\alpha\, \mathrm{r}^\alpha - \mathrm{div}\, \mathbf{q}^\alpha + \hat{\mathrm{e}}^\alpha\,. \end{aligned} \tag{3.93}$$

Making use of the local statement for the balance equation of momentum eq. (3.70), under consideration of the symmetry of the partial *Cauchy* stress tensor (cf. eq. (3.83)), which allows the replacement of $\mathbf{L}_\alpha$ by $\mathbf{D}_\alpha$, the alternative local form of the balance of energy is obtained:

$$\rho^\alpha\, (\varepsilon^\alpha)'_\alpha - \mathbf{T}^\alpha \cdot \mathbf{D}_\alpha - \rho^\alpha\, \mathrm{r}^\alpha + \mathrm{div}\, \mathbf{q}^\alpha = \hat{\mathrm{e}}^\alpha - \hat{\mathbf{p}}^\alpha \cdot \mathbf{x}'_\alpha - \hat{\rho}^\alpha\, (\, \varepsilon^\alpha - \frac{1}{2}\, \mathbf{x}'_\alpha \cdot \mathbf{x}'_\alpha\,)\,. \tag{3.94}$$

Summation of eq. (3.94) over all constituents κ leads to

$$\sum_{\alpha=1}^{\kappa} [\, \rho^\alpha \, (\varepsilon^\alpha)'_\alpha - \mathbf{T}^\alpha \cdot \mathbf{D}_\alpha - \rho^\alpha \, \mathrm{r}^\alpha + \mathrm{div}\, \mathbf{q}^\alpha \,] = \tag{3.95}$$

$$= \sum_{\alpha=1}^{\kappa} [\hat{\mathrm{e}}^\alpha - \hat{\mathbf{p}}^\alpha \cdot \mathbf{x}'_\alpha - \hat{\rho}^\alpha \, (\, \varepsilon^\alpha - \frac{1}{2}\, \mathbf{x}'_\alpha \cdot \mathbf{x}'_\alpha \,)\,] \, . \tag{3.96}$$

When compared to the law of energy conservation to a single component material, the condition

$$\sum_{\alpha=1}^{\kappa} \hat{\mathrm{e}}^\alpha = 0 \tag{3.97}$$

is sufficient to fulfil *Truesdell's* third metaphysical principle. Alternatively, the local balance of energy eq. (3.94) can be formulated with the use of the partial *Helmholtz* free energy:

$$\psi^\alpha = \varepsilon^\alpha - \theta^\alpha \, \eta^\alpha \tag{3.98}$$

and its corresponding material time derivative:

$$(\psi^\alpha)'_\alpha = (\varepsilon^\alpha)'_\alpha - (\theta^\alpha)'_\alpha \, \eta^\alpha - \theta \, (\eta^\alpha)'_\alpha \tag{3.99}$$

where $\eta^\alpha = \eta^\alpha \, (\mathbf{x}, \mathrm{t})$ and $\theta = \theta \, (\mathbf{x}, \mathrm{t})$ denote the partial specific entropy and the partial temperature respectively. As such, eq. (3.94) can be transformed to

$$\begin{aligned} &\rho^\alpha \, [\, (\psi^\alpha)'_\alpha + (\theta^\alpha)'_\alpha \, \eta^\alpha + \theta^\alpha \, (\eta^\alpha)'_\alpha \,] - \mathbf{T}^\alpha \cdot \mathbf{D}_\alpha - \rho^\alpha \, \mathrm{r}^\alpha + \mathrm{div}\, \mathbf{q}^\alpha = \\ &= \hat{\mathrm{e}}^\alpha - \hat{\mathbf{p}}^\alpha \cdot \mathbf{x}'_\alpha - \hat{\rho}^\alpha \, (\, \psi^\alpha + \theta^\alpha \, \eta^\alpha - \frac{1}{2}\, \mathbf{x}'_\alpha \cdot \mathbf{x}'_\alpha \,) \, . \end{aligned} \tag{3.100}$$

3.6 Entropy inequality

A much debated topic in the field, the second law of thermodynamics, known as the entropy inequality, has been usefully applied in order to gain constitutive relations for the material in continuum mechanics, mixture theory and TPM. Originally created by Coleman and Noll [26], this inequality in its classical form is used, namely as the sum of all entropy inequalities for the individual constituents. The assumption that the inequality is fulfilled for every individual constituent φ^α is a sufficient condition, albeit too restrictive, and is thus defined as

$$\sum_{\alpha=1}^{\kappa} (\mathrm{H}^\alpha)'_\alpha \geq \sum_{\alpha=1}^{\kappa} \int_{\mathrm{B}_\alpha} \frac{1}{\theta^\alpha} \, \rho^\alpha \, \mathrm{r}^\alpha \, \mathrm{dv} - \sum_{\alpha=1}^{\kappa} \int_{\partial \mathrm{B}_\alpha} \frac{1}{\theta^\alpha} \, \mathbf{q}^\alpha \cdot \mathrm{d}\mathbf{a} \tag{3.101}$$

for the mixture body, where the entropy

$$\mathrm{H}^\alpha = \int_{\mathrm{B}_\alpha} \rho^\alpha \, \eta^\alpha \, \mathrm{dv} \tag{3.102}$$

has been used. Insertion of the material time derivative of the entropy

$$(\mathrm{H}^\alpha)'_\alpha = \int\limits_{\mathrm{B}_\alpha} [\, \rho^\alpha\, (\eta^\alpha)'_\alpha + \hat{\rho}^\alpha\, \eta^\alpha \,]\, \mathrm{dv}, \tag{3.103}$$

where the local statement of the balance of mass eq. (3.58) has been used, and the relation

$$\int\limits_{\partial \mathrm{B}_\alpha} \frac{1}{\theta^\alpha}\, \mathbf{q}^\alpha \cdot \mathrm{d}\mathbf{a} = \int\limits_{\mathrm{B}_\alpha} \mathrm{div}\, (\, \frac{1}{\theta^\alpha}\, \mathbf{q}^\alpha \,)\, \mathrm{dv} \tag{3.104}$$

leads to

$$\sum_{\alpha=1}^{\kappa} \int\limits_{\mathrm{B}_\alpha} [\, \rho^\alpha\, (\eta^\alpha)'_\alpha + \hat{\rho}^\alpha\, \eta^\alpha \,]\, \mathrm{dv} \geq \sum_{\alpha=1}^{\kappa} \int\limits_{\mathrm{B}_\alpha} [\, \frac{1}{\theta^\alpha}\, \rho^\alpha\, \mathrm{r}^\alpha \, - \mathrm{div}\, (\, \frac{1}{\theta^\alpha}\, \mathbf{q}^\alpha \,)\,]\, \mathrm{dv}\, . \tag{3.105}$$

Under consideration of the *Helmholtz* free energy function, its derivative, the local balance of energy eq. (3.94) with

$$\rho^\alpha\, \mathrm{r}^\alpha = -\rho^\alpha\, (\varepsilon^\alpha)'_\alpha + \mathbf{T}^\alpha \cdot \mathbf{D}_\alpha - \mathrm{div}\, \mathbf{q}^\alpha - \hat{\mathrm{e}}^\alpha + \hat{\mathbf{p}}^\alpha \cdot \mathbf{x}'_\alpha + \hat{\rho}^\alpha\, (\, \varepsilon^\alpha + \frac{1}{2}\, \mathbf{x}'_\alpha \cdot \mathbf{x}'_\alpha \,)\, . \tag{3.106}$$

and the relation

$$\mathrm{div}\, (\, \frac{1}{\theta^\alpha}\, \mathbf{q}^\alpha \,) = -\frac{1}{\theta^\alpha}\, \mathrm{grad}\, \theta^\alpha \cdot \mathbf{q}^\alpha + \mathrm{div}\, \mathbf{q}^\alpha\, , \tag{3.107}$$

the local entropy inequality is given as

$$\begin{aligned} &\sum_{\alpha=1}^{\kappa} \frac{1}{\theta^\alpha}\, \{\, -\rho^\alpha [(\psi^\alpha)'_\alpha + (\theta^\alpha)'_\alpha\, \eta^\alpha\,] - \hat{\rho}^\alpha\, (\, \psi^\alpha - \frac{1}{2}\, \mathbf{x}'_\alpha \cdot \mathbf{x}'_\alpha \,) + \\ &+ \mathbf{T}^\alpha \cdot \mathbf{D}_\alpha - \hat{\mathbf{p}}^\alpha \cdot \mathbf{x}'_\alpha - \frac{1}{\theta^\alpha}\, \mathbf{q}^\alpha \cdot \mathrm{grad}\, \theta^\alpha + \hat{\mathrm{e}}^\alpha \} \geq 0\, , \end{aligned} \tag{3.108}$$

which is sufficient and convenient in order to gain restrictions for constitutive modelling and therefore no other possible forms will be considered here.

Chapter 4

Biphasic material model

Based upon the fundamental porous media theory, one may proceed with the tailoring of the kinematics and constitutive relations within the balance equations in order to augment and specialise the model in accordance with the theoretical background required for the analysis of cardiac tissue. As such, the basic theory of porous media is expanded upon in a more specialised manner in the following.

For the purposes of cardiac modelling, the specialised case of a biphasic porous body is chosen such that all constituents are deemed to be incompressible. Additionally, the number of constituents is limited to the case of two, namely solid (φ^{S}) and fluid (φ^{F}), such that $\alpha \in \{\mathrm{S},\ \mathrm{F}\}$. It is assumed that there is no difference in temperatures between the two phases, leading to a uniform mixture temperature θ and heat flux $\mathbf{q}$:

$$\theta = \theta^{\mathrm{S}} = \theta^{\mathrm{F}} \qquad \text{and} \qquad \mathbf{q} = \mathbf{q}^{\mathrm{S}} = \mathbf{q}^{\mathrm{F}}, \tag{4.1}$$

respectively. Generally, with the inclusion of solidification or change of phases (for e.g. ice/water/gas), the theoretical option exists for the use of different phase temperatures. In the case of cardiac modelling, however, the assumption that the fluid within the tissue and pericardial fluid surrounding the heart are at an equal temperature is reasonable. Following eq. (4.1), it is clear that the energy supplies (which result from a difference in phase temperature) $\hat{\mathrm{e}}^{\alpha}$ must be zero:

$$\hat{\mathrm{e}}^{\alpha} = 0, \qquad \forall\, \alpha \in \{\mathrm{S},\ \mathrm{F}\}. \tag{4.2}$$

Concerning the motion, the dynamic effects are ignored in the fact that a quasi-static approach is adopted such that

$$\mathbf{x}''_{\alpha} = \mathbf{0}, \qquad \forall\, \alpha \in \{\mathrm{S},\ \mathrm{F}\} \tag{4.3}$$

from which the seepage velocity is able to be determined explicitly via the use of the quasi-static *Darcy* [1] formulation. Due to the incompressibility of the phases, the real density remains constant leading to:

$$\rho^{\mathrm{SR}} = \rho^{\mathrm{SR}}_{0\mathrm{S}} = \text{const.} \Rightarrow (\rho^{\mathrm{SR}})'_{\mathrm{S}} = (\rho^{\mathrm{SR}}_{0\mathrm{S}})'_{\mathrm{S}} = 0 \Rightarrow (\rho^{\mathrm{S}})'_{\mathrm{S}} = (\mathrm{n}^{\mathrm{S}})'_{\mathrm{S}}\, \rho^{\mathrm{SR}}_{0\mathrm{S}} \tag{4.4}$$

along with a constant density of the liquid phase:

---

[1] Henry Darcy (1803-1858): French engineer who made important contributions to the field of hydraulics. He is credited for the development of Darcy's Law for flow in porous media, invented the modern Pitot tube and was appointed chief engineer for the department of Côte d'Or in eastern France in 1840.

$$\rho^{\mathrm{FR}} = \rho^{\mathrm{FR}}_{0\mathrm{F}} = \text{const.} \Rightarrow (\rho^{\mathrm{FR}})'_{\mathrm{F}} = (\rho^{\mathrm{FR}}_{0\mathrm{F}})'_{\mathrm{F}} = 0 \Rightarrow (\rho^{\mathrm{F}})'_{\mathrm{F}} = (\mathrm{n}^{\mathrm{F}})'_{\mathrm{F}}\, \rho^{\mathrm{FR}}_{0\mathrm{F}} \tag{4.5}$$

where the fluid phase denoted by F is interchangeable with the liquid phase denoted by L as no other constituents are contained within the liquid phase.

4.1 Local forms of the balance laws - field equations

Along with the constitutive relations developed, the field equations form the calculation concept for the saturated porous body. Continuing from the derivation of the balance equations, and with the use of $\rho^\alpha = \mathrm{n}^\alpha \rho^{\alpha\mathrm{R}}$ substituted into eq. (3.58) and with the use of eq. (4.4) and eq. (4.5) the balance of mass for the solid and fluid respectively yields

$$\left(\mathrm{n}^{\mathrm{S}}\right)'_{\mathrm{S}} + \mathrm{n}^{\mathrm{S}} \operatorname{div} \mathbf{x}'_{\mathrm{S}} = \frac{\hat{\rho}^{\mathrm{S}}}{\rho^{\mathrm{SR}}} \qquad \text{and} \qquad \left(\mathrm{n}^{\mathrm{F}}\right)'_{\mathrm{F}} + \mathrm{n}^{\mathrm{F}} \operatorname{div} \mathbf{x}'_{\mathrm{F}} = \frac{\hat{\rho}^{\mathrm{F}}}{\rho^{\mathrm{FR}}}. \tag{4.6}$$

Making use of the local equations for the balance of momentum eq. (3.70), separated into the solid and fluid parts respectively yields

$$\operatorname{div} \mathbf{T}^{\mathrm{S}} + \rho^{\mathrm{S}}\mathbf{b} + \hat{\mathbf{p}}^{\mathrm{S}} - \hat{\rho}^{\mathrm{S}}\mathbf{x}''_{\mathrm{S}} = \mathbf{0} \qquad \text{and} \qquad \operatorname{div} \mathbf{T}^{\mathrm{F}} + \rho^{\mathrm{F}}\mathbf{b} + \hat{\mathbf{p}}^{\mathrm{F}} - \hat{\rho}^{\mathrm{F}}\mathbf{x}''_{\mathrm{F}} = \mathbf{0}. \tag{4.7}$$

In order to describe the thermal behaviour of the mixture body, the energy balance equation is essential (see eq. (3.96)):

$$\sum_{\alpha}^{\mathrm{S,F}} [\, \rho^\alpha\, (\varepsilon^\alpha)'_\alpha - \mathbf{T}^\alpha \cdot \mathbf{D}_\alpha - \rho^\alpha\, \mathrm{r}^\alpha + \operatorname{div} \mathbf{q}^\alpha \,] = \sum_{\alpha}^{\mathrm{S,F}} [-\hat{\mathbf{p}}^\alpha \cdot \mathbf{x}'_\alpha - \hat{\rho}^\alpha\, (\, \varepsilon^\alpha - \frac{1}{2}\mathbf{x}'_\alpha \cdot \mathbf{x}'_\alpha\,)\,] \tag{4.8}$$

where the internal energy $\epsilon^\alpha = \psi^\alpha + \theta\eta^\alpha$ is considered (see eq. (3.99)). Furthermore, the saturation condition, and requirements for the interaction forces and mass supplies are used respectively as

$$\mathrm{n}^{\mathrm{S}} + \mathrm{n}^{\mathrm{F}} = 1, \qquad \hat{\mathbf{p}}^{\mathrm{S}} + \hat{\mathbf{p}}^{\mathrm{F}} = \mathbf{0} \qquad \text{and} \qquad \hat{\rho}^{\mathrm{S}} + \hat{\rho}^{\mathrm{F}} = 0 \tag{4.9}$$

which are taken into account as physical constraint conditions.

4.1.1 Closure problem and saturation constraint

In mixture theory, the basis of porous media theory, the sum of constitutive equations and balance equations is equal to the number of unknown fields resulting in a closed system, which is easily proven by adding the number of field equations and constitutive quantities and subtracting the number of unknown field quantities. However, due to the introduction of the volume fractions which touch on the micro-scale level as the method of obtaining a smeared continua, a problem arises in which a field equation is missing. In this regard, porous media theory differs greatly from that of mixture theory and classical continuum mechanics.

In order to gain a realistic calculation concept for the pore pressure λ and to close the equation system, the saturation condition (see eq. (3.13)) along with the balance of mass is made use of and added to the entropy inequality. As a starting point, the material time derivative of the saturation condition is considered with respect to the solid motion:

$$\left(\mathrm{n^S}\right)'_\mathrm{S} + \left(\mathrm{n^F}\right)'_\mathrm{S} = 0. \tag{4.10}$$

With the definition of $\mathrm{n}^\alpha = \mathrm{n}^\alpha \left[\mathbf{x}\left(\mathbf{X}_\alpha, \mathrm{t}\right), \mathrm{t}\right]$ it follows that the material time derivative for the solid volume fraction with respect to the solid motion yields

$$\left(\mathrm{n^S}\right)'_\mathrm{S} = \frac{\partial \mathrm{n^S}}{\partial \mathrm{t}} + \operatorname{grad} \mathrm{n^S} \cdot \mathbf{x}'_\mathrm{S}$$

and for the fluid volume fraction with respect to the fluid motion

$$\left(\mathrm{n^F}\right)'_\mathrm{F} = \frac{\partial \mathrm{n^F}}{\partial \mathrm{t}} + \operatorname{grad} \mathrm{n^F} \cdot \mathbf{x}'_\mathrm{F}. \tag{4.11}$$

Additionally, the material time derivative of the fluid volume fraction with respect to the solid motion is considered yielding

$$\left(\mathrm{n^F}\right)'_\mathrm{S} = \left(\mathrm{n^F}\right)'_\mathrm{F} - \operatorname{grad} \mathrm{n^F} \cdot \mathbf{w}_\mathrm{FS}.$$

As such, the material time derivative of the saturation condition reads:

$$\left(\mathrm{n^S}\right)'_\mathrm{S} + \left(\mathrm{n^F}\right)'_\mathrm{F} - \operatorname{grad} \mathrm{n^F} \cdot \mathbf{w}_\mathrm{FS} = 0. \tag{4.12}$$

Now, by dividing the mass balance of the balance of mass eq. (3.58) we obtain the volume balance of mass :

$$\left(\mathrm{n}^\alpha\right)'_\alpha + \mathrm{n}^\alpha \operatorname{div}\, \mathbf{x}'_\alpha = \frac{\hat{\rho}^\alpha}{\rho^{\alpha\mathrm{R}}}. \tag{4.13}$$

With the use of div $\mathbf{x}'_\alpha = \operatorname{grad} \mathbf{x}'_\alpha \cdot \mathbf{1} = \mathbf{L}_\alpha : \mathbf{1} = \mathbf{D}_\alpha : \mathbf{1}$ we gain

$$\left(\mathrm{n}^\alpha\right)'_\alpha - \mathrm{n}^\alpha\, \mathbf{D}_\alpha : \mathbf{1} = \frac{\hat{\rho}^\alpha}{\rho^{\alpha\mathrm{R}}}. \tag{4.14}$$

Therefore, eq. (4.12) and eq. (4.14) are multiplied by respective *Lagrange* multipliers λ, κ^S and κ^F and thus a relation between the volume fractions, pressure and filter velocity is obtained, as a solution to the neglected dependency resulting from the addition of the volume fractions into the equation system.

4.2 Constitutive theory

In order to address the closure problem, The *Lagrange* multiplier λ, identified as the pore pressure, has been introduced. Therefore, the resulting set of unknown quantities of the equation system yields

$$\mathcal{U} = \left\{ \mathbf{u}_{\mathrm{S}}, \mathrm{n}^{\mathrm{S}}, \lambda \right\}. \tag{4.15}$$

The remaining constitutive quantities, under consideration that the external acceleration due to gravity $\mathbf{b}$ is known, are determined as

$$\mathcal{C} = \left\{ \mathbf{T}^{\mathrm{S}}, \mathbf{T}^{\mathrm{F}}, \psi^{\mathrm{S}}, \psi^{\mathrm{F}}, \hat{\rho}^{\mathrm{S}}, \hat{\mathbf{p}}^{\mathrm{S}} \right\} \tag{4.16}$$

which require further assumptions to close the set of equations. Taking into account the evaluation of the entropy inequality in analogy to Coleman and Noll [26], the following set of process variables are chosen:

$$\mathcal{P} = \left\{ \mathbf{C}_{\mathrm{S}}, \mathrm{J}_{\mathrm{F}}, \mathrm{n}^{\mathrm{S}}, \mathrm{n}^{\mathrm{F}}, \mathbf{w}_{\mathrm{FS}}, \operatorname{grad} \mathrm{n}^{\mathrm{F}} \right\} \tag{4.17}$$

where apart from the usual volume fractions and seepage velocity $\mathbf{w}_{\mathrm{FS}}$, the right *Cauchy-Green* deformation tensor and fluid Jacobian J_{F} have been chosen. This is because of the assumed mass transfer between phases, leading to a non-standard description of the volume fractions departing from the usual description via the solid Jacobian which in the case of no mass exchange is simply determined via integration of the balance of mass for the mixture.

4.2.1 Evaluation of the entropy inequality

In order to restrict the complexity of this investigation to a reasonable scope, and to maintain a consistent formulation with consideration of an intermediate stress-free configuration, the dependencies of the *Helmholtz* free energy for the solid and fluid phases are defined as

$$\psi^{\mathrm{S}} = \psi^{\mathrm{S}} \left(\mathbf{C}_{\mathrm{Se}}, \mathrm{n}^{\mathrm{S}} \right) \qquad \text{and} \qquad \psi^{\mathrm{F}} = \psi^{\mathrm{F}} \left(\mathrm{n}^{\mathrm{F}} \right) \tag{4.18}$$

respectively. From eq. (3.108), the terms $\rho^{\mathrm{S}} \left(\psi^{\mathrm{S}} \right)'_{\mathrm{S}}$ and $\rho^{\mathrm{F}} \left(\psi^{\mathrm{F}} \right)'_{\mathrm{F}}$ are required to be expanded upon. Therefore, making use of the relation

$$\mathbf{C}_{\mathrm{Se}} = \mathbf{F}_{\mathrm{Sg}}^{-\mathrm{T}} \, \mathbf{C}_{\mathrm{S}} \, \mathbf{F}_{\mathrm{Sg}}^{-1} \tag{4.19}$$

allows for the derivative of the *Helmholtz* free energy function with respect to $\mathbf{C}_{\mathrm{S}}$ to be taken, which leads to the relations

$$\rho^{\mathrm{S}} \left(\psi^{\mathrm{S}} \right)'_{\mathrm{S}} = \rho^{\mathrm{S}} \frac{\partial \psi^{\mathrm{S}}}{\partial \mathrm{n}^{\mathrm{S}}} \left(\mathrm{n}^{\mathrm{S}} \right)'_{\mathrm{S}} + 2 \rho^{\mathrm{S}} \mathbf{F}_{\mathrm{S}} \frac{\partial \psi^{\mathrm{S}}}{\partial \mathbf{C}_{\mathrm{S}}} \mathbf{F}_{\mathrm{S}}^{\mathrm{T}} : \mathbf{D}_{\mathrm{S}} \qquad \text{and} \tag{4.20}$$

$$\rho^{\mathrm{F}} \left(\psi^{\mathrm{F}} \right)'_{F} = \rho^{\mathrm{F}} \frac{\psi^{\mathrm{F}}}{\partial \mathrm{n}^{\mathrm{F}}} \left(\mathrm{n}^{\mathrm{F}} \right)'_{\mathrm{F}}. \tag{4.21}$$

Bearing in mind the methods employed to address the saturation constraint and closure problem, the material time derivative of the saturation condition eq. (4.12) and volume balance of mass eq. (4.14) are added to the entropy inequality via a multiplication of the respective *Lagrange* multipliers, where κ^α are weighted multipliers associated with the compressibility of the pore fluid (see [28]):

$$\lambda\left\{\left(\mathrm{n}^{\mathrm{S}}\right)'_{\mathrm{S}}+\left(\mathrm{n}^{\mathrm{F}}\right)'_{\mathrm{F}}-\operatorname{grad}\mathrm{n}^{\mathrm{F}}\cdot\mathbf{w}_{\mathrm{FS}}\right\}=0,\qquad\text{and}\qquad\kappa^\alpha\left\{\left(\mathrm{n}^\alpha\right)'_\alpha-\mathrm{n}^\alpha\,\mathbf{D}_\alpha:\mathbf{1}=\frac{\hat\rho^\alpha}{\rho^{\alpha\mathrm{R}}}\right\}\tag{4.22}$$

and added to the entropy inequality eq. (3.108) yielding:

$$\begin{aligned}\Gamma=&-\rho^{\mathrm{S}}\frac{\partial\psi^{\mathrm{S}}}{\partial\mathrm{n}^{\mathrm{S}}}\left(\mathrm{n}^{\mathrm{S}}\right)'_{\mathrm{S}}-2\rho^{\mathrm{S}}\mathbf{F}_{\mathrm{S}}\frac{\partial\psi^{\mathrm{S}}}{\partial\mathbf{C}_{\mathrm{S}}}\mathbf{F}^{\mathrm{T}}_{\mathrm{S}}\cdot\mathbf{D}_{\mathrm{S}}-\rho^{\mathrm{F}}\frac{\psi^{\mathrm{F}}}{\partial\mathrm{n}^{\mathrm{F}}}\left(\mathrm{n}^{\mathrm{F}}\right)'_{\mathrm{F}}-\\&-\hat\rho^{\mathrm{S}}\left(\psi^{\mathrm{S}}-\frac{1}{2}\mathbf{x}'_{\mathrm{S}}\cdot\mathbf{x}'_{\mathrm{S}}\right)-\hat\rho^{\mathrm{F}}\left(\psi^{\mathrm{F}}-\frac{1}{2}\mathbf{x}'_{\mathrm{F}}\cdot\mathbf{x}'_{\mathrm{F}}\right)+\mathbf{T}^{\mathrm{S}}\cdot\mathbf{D}_{\mathrm{S}}+\mathbf{T}^{\mathrm{F}}\cdot\mathbf{D}_{\mathrm{F}}-\\&-\hat{\mathbf{p}}^{\mathrm{S}}\cdot\mathbf{x}'_{\mathrm{S}}-\hat{\mathbf{p}}^{\mathrm{F}}\cdot\mathbf{x}'_{\mathrm{F}}-\lambda\left[\left(\mathrm{n}^{\mathrm{S}}\right)'_{\mathrm{S}}+\left(\mathrm{n}^{\mathrm{F}}\right)'_{\mathrm{F}}-\operatorname{grad}\mathrm{n}^{\mathrm{F}}\mathbf{w}_{\mathrm{FS}}\right]+\\&+\kappa^{\mathrm{S}}\left[\left(\mathrm{n}^{\mathrm{S}}\right)'_{\mathrm{S}}+\mathrm{n}^{\mathrm{S}}\mathbf{D}_{\mathrm{S}}\cdot\mathbf{I}-\frac{\hat\rho^{\mathrm{S}}}{\rho^{\mathrm{SR}}}\right]+\kappa^{\mathrm{F}}\left[\left(\mathrm{n}^{\mathrm{F}}\right)'_{\mathrm{F}}+\mathrm{n}^{\mathrm{F}}\mathbf{D}_{\mathrm{F}}\cdot\mathbf{I}-\frac{\hat\rho^{\mathrm{F}}}{\rho^{\mathrm{FR}}}\right]\geq0.\end{aligned}\tag{4.23}$$

Inserting the constitutive relations

$$\hat{\mathbf{p}}^{\mathrm{S}}=-\hat{\mathbf{p}}^{\mathrm{F}}\qquad\text{and}\qquad\hat\rho^{\mathrm{S}}=-\hat\rho^{\mathrm{F}}\tag{4.24}$$

as proposed by Ricken and Bluhm [85] and making use of the simplification

$$\hat{\mathbf{p}}^{\mathrm{S}}\,\mathbf{x}'_{\mathrm{S}}+\hat{\mathbf{p}}^{\mathrm{F}}\,\mathbf{x}'_{\mathrm{F}}=\hat{\mathbf{p}}^{\mathrm{F}}\left(\mathbf{x}'_{\mathrm{F}}-\mathbf{x}'_{\mathrm{S}}\right)=\hat{\mathbf{p}}^{\mathrm{F}}\,\mathbf{w}_{\mathrm{FS}}\tag{4.25}$$

yields

$$\begin{aligned}\Gamma=&+\mathbf{D}_{\mathrm{S}}\cdot\left\{\mathbf{T}^{\mathrm{S}}+\kappa^{\mathrm{S}}\mathrm{n}^{\mathrm{S}}\mathbf{I}-2\rho^{\mathrm{S}}\mathbf{F}_{\mathrm{S}}\frac{\partial\psi^{\mathrm{S}}}{\partial\mathbf{C}_{\mathrm{S}}}\mathbf{F}^{\mathrm{T}}_{\mathrm{S}}\right\}+\mathbf{D}_{\mathrm{F}}\cdot\left\{\mathbf{T}^{\mathrm{F}}+\kappa^{\mathrm{F}}\mathrm{n}^{\mathrm{F}}\mathbf{I}-\rho^{\mathrm{F}}\mathrm{J}_{\mathrm{F}}\frac{\partial\psi^{\mathrm{F}}}{\partial\mathrm{J}_{\mathrm{F}}}\mathbf{I}\right\}-\\&-\left(\mathrm{n}^{\mathrm{S}}\right)'_{\mathrm{S}}\left\{\left(\lambda-\kappa^{\mathrm{S}}\right)+\rho^{\mathrm{S}}\frac{\partial\psi^{\mathrm{S}}}{\partial\mathrm{n}^{\mathrm{S}}}\right\}-\left(\mathrm{n}^{\mathrm{F}}\right)'_{\mathrm{F}}\left\{\left(\lambda-\kappa^{\mathrm{F}}\right)+\rho^{\mathrm{F}}\frac{\partial\psi^{\mathrm{F}}}{\partial\mathrm{n}^{\mathrm{F}}}\right\}-\\&-\hat\rho^{\mathrm{F}}\left\{\left(\psi^{\mathrm{F}}-\frac{1}{2}\,\mathbf{x}'_{\mathrm{F}}\cdot\mathbf{x}'_{\mathrm{F}}\right)-\left(\psi^{\mathrm{S}}-\frac{1}{2}\,\mathbf{x}'_{\mathrm{S}}\cdot\mathbf{x}'_{\mathrm{S}}\right)+\frac{\kappa^{\mathrm{F}}}{\rho^{\mathrm{FR}}}-\frac{\kappa^{\mathrm{S}}}{\rho^{\mathrm{SR}}}\right\}-\\&-\mathbf{w}_{\mathrm{FS}}\left\{\hat{\mathbf{p}}^{\mathrm{F}}-\lambda\mathrm{grad}\mathrm{n}^{\mathrm{F}}\right\}\geq0\end{aligned}\tag{4.26}$$

which, as stated by Ricken and Bluhm [85] must hold for fixed values of the process variables and arbitrary values of freely available quantities which contain selected derivatives contained within $\mathcal{P}$. Thus, considering the energy preserving parts connected with $(\mathrm{n}^{\mathrm{S}})'_{\mathrm{S}}$ and $(\mathrm{n}^{\mathrm{F}})'_{\mathrm{F}}$ yields

$$\begin{aligned}&\lambda-\kappa^{\mathrm{S}}+\rho^{\mathrm{S}}\frac{\partial\psi^{\mathrm{S}}}{\partial\mathrm{n}^{\mathrm{S}}}=0\implies\kappa^{\mathrm{S}}=\lambda+\rho^{\mathrm{S}}\frac{\partial\psi^{\mathrm{S}}}{\partial\mathrm{n}^{\mathrm{S}}}\qquad\text{and}\\&\lambda-\kappa^{\mathrm{F}}+\rho^{\mathrm{F}}\frac{\partial\psi^{\mathrm{F}}}{\partial\mathrm{n}^{\mathrm{F}}}=0\implies\kappa^{\mathrm{F}}=\lambda+\rho^{\mathrm{F}}\frac{\partial\psi^{\mathrm{F}}}{\partial\mathrm{n}^{\mathrm{F}}}\end{aligned}\tag{4.27}$$

respectively which allow sufficient conditions for the second law of thermodynamics to be obtained. Considering the dissipation, the following must hold true for the entropy inequality to be fulfilled:

$$
\begin{aligned}
&-\rho^{\mathrm{F}}\underbrace{\left\{\left[\psi^{\mathrm{F}}-\frac{1}{2}\,\mathbf{x}'_{F}\cdot\mathbf{x}'_{F}+\frac{\lambda}{\rho^{\mathrm{FR}}}+\mathrm{n}^{\mathrm{F}}\frac{\partial\psi^{\mathrm{F}}}{\partial\mathrm{n}^{\mathrm{F}}}\right]-\left[\psi^{\mathrm{S}}-\frac{1}{2}\,\mathbf{x}'_{\mathrm{S}}\cdot\mathbf{x}'_{\mathrm{S}}+\frac{\lambda}{\rho^{\mathrm{SR}}}+\mathrm{n}^{\mathrm{S}}\frac{\partial\psi^{\mathrm{S}}}{\partial\mathrm{n}^{\mathrm{S}}}\right]\right\}}_{\bar{\Psi}^{\mathrm{F}}-\bar{\Psi}^{\mathrm{S}}}-\\
&-\mathbf{w}_{\mathrm{FS}}\left\{\hat{\mathbf{p}}^{\mathrm{F}}-\lambda\mathrm{grad}\mathrm{n}^{\mathrm{F}}\right\}\geq 0
\end{aligned}
\tag{4.28}
$$

where the postulations for the chemical potentials $\bar{\Psi}^{\alpha}$ have been outlined. Therefore, the following postulations for $\hat{\rho}^{\mathrm{F}}$ and $\hat{\mathbf{p}}^{\mathrm{F}}$ are made in order to fulfil the dissipation ([85])

$$
\hat{\rho}^{\mathrm{F}}=-\delta^{\mathrm{SF}}\left(\bar{\Psi}^{\mathrm{F}}-\bar{\Psi}^{\mathrm{S}}\right),\qquad \delta^{\mathrm{SF}}\geq 0\qquad\text{and}
\tag{4.29}
$$

$$
\hat{\mathbf{p}}^{\mathrm{F}}=\lambda\mathrm{grad}\mathrm{n}^{\mathrm{F}}-\mathbf{S}_{\mathrm{F}}\mathbf{w}_{\mathrm{FS}}
\tag{4.30}
$$

and thus allow for further constitutive modelling for the stress, mass exchange and interaction forces.

4.2.2 Stress

For the energy preserving parts connected with $\mathbf{D}_{\mathrm{S}}$ and $\mathbf{D}_{\mathrm{F}}$ considering eq. (4.26), and under the assumption $\partial\psi^{\mathrm{F}}/\partial\mathrm{n}^{\mathrm{F}}=0$ (cf. [85]) we gain the relations for the *Cauchy* stress for the solid and fluid respectively as

$$
\mathbf{T}^{\mathrm{S}}=-\mathrm{n}^{\mathrm{S}}\lambda\mathbf{I}-\mathrm{n}^{\mathrm{S}}\rho^{\mathrm{S}}\frac{\partial\psi^{\mathrm{S}}}{\partial\mathrm{n}^{\mathrm{S}}}+2\rho^{\mathrm{S}}\mathbf{F}_{\mathrm{S}}\frac{\partial\psi^{\mathrm{S}}}{\partial\mathbf{C}_{\mathrm{S}}}\mathbf{F}_{\mathrm{S}}^{\mathrm{T}}\qquad\text{and}\qquad\mathbf{T}^{\mathrm{F}}=-\mathrm{n}^{\mathrm{F}}\lambda\mathbf{I}.
\tag{4.31}
$$

The total stress is defined as the sum of the partial stresses, and making use of the saturation condition yields:

$$
\mathbf{T}=\mathbf{T}^{\mathrm{S}}+\mathbf{T}^{\mathrm{F}}=\mathbf{T}_{\mathrm{E}}^{\mathrm{S}}-\lambda\mathbf{1}
\tag{4.32}
$$

from which the second and first *Piola-Kirchhoff* stress tensors are defined respectively as

$$
\mathbf{S}=\mathrm{J}_{\mathrm{S}}\mathbf{F}_{\mathrm{S}}^{-1}\,\mathbf{T}\,\mathbf{F}_{\mathrm{S}}^{-\mathrm{T}}\qquad\text{and}\qquad\mathbf{P}=\mathbf{F}_{\mathrm{S}}\,\mathbf{S}.
\tag{4.33}
$$

4.2.3 Filter velocity

Due to the *Lagrangian* description of motion used for the solid, and the calculation concept that the solid displacements are solved for, the motion of the fluid is determined relative to the solid, via the seepage velocity $\mathbf{w}_{\mathrm{FS}}=\mathbf{x}'_{\mathrm{F}}-\mathbf{x}'_{\mathrm{S}}$, which are connected via the interaction forces $\hat{\mathbf{p}}^{\mathrm{F}}=-\hat{\mathbf{p}}^{\mathrm{S}}$. From evaluation of the entropy inequality, the following relation is gained:

$$
\hat{\mathbf{p}}^{\mathrm{F}}=\lambda\mathrm{grad}\mathrm{n}^{\mathrm{F}}-\mathbf{S}_{\mathrm{F}}\mathbf{w}_{\mathrm{FS}}
\tag{4.34}
$$

for which the following representation of the anisotropic permeability proposed by Ricken et al. [87] has been used:

$$\mathbf{S}_{\mathrm{F}} = \alpha_{\mathrm{F0}}\left[(1-\alpha_{\mathrm{F}})\,\mathbf{1} + \alpha_{\mathrm{F}}\mathbf{M}_{\mathrm{f}}\right]^{-1} \tag{4.35}$$

where $\alpha_{\mathrm{F}} \in [0,1]$ is a factor which defines the range of permeability from fully isotropic to fully transverse isotropic and the permeability tensor in the actual configuration is denoted $\mathbf{M}_{\mathrm{f}} = \mathbf{f}_{\mathrm{f}} \otimes \mathbf{f}_{\mathrm{f}}$ wherein $\mathbf{f}_{\mathrm{f}} = \mathbf{F}_{\mathrm{S}}\mathbf{f}_0$ is the fibre direction in the actual configuration. For further analysis, it is assumed that the factor $\alpha_{\mathrm{F}} = 1$, causing a fully transverse isotropic permeability at all times. With the use of $\mathbf{T}^{\mathrm{F}} = -\lambda \mathrm{n}^{\mathrm{F}}\mathbf{1}$ and the balance of momentum in the form

$$\operatorname{div}\mathbf{T}^{\mathrm{F}} + \rho^{\mathrm{F}}\mathbf{b} + \hat{\mathbf{p}}^{\mathrm{F}} = \mathbf{0}, \tag{4.36}$$

we continue as follows for the balance of momentum:

$$-\operatorname{div}\left(\mathrm{n}^{\mathrm{F}}\lambda\mathbf{1}\right) + \rho^{\mathrm{F}}\mathbf{b} + \hat{\mathbf{p}}^{\mathrm{F}} = \mathbf{0}. \tag{4.37}$$

Continuing in index notation with $\operatorname{div}(\mathrm{n}^{\mathrm{F}}\lambda\mathbf{1})$ we have

$$\left(\mathrm{n}^{\mathrm{F}}\lambda\delta_{\mathrm{ij}}\right)_{,\mathrm{j}} = \mathrm{n}^{\mathrm{F}}_{,\mathrm{j}}\lambda\delta_{\mathrm{ij}} + \mathrm{n}^{\mathrm{F}}\lambda_{,\mathrm{j}}\delta_{\mathrm{ij}} \tag{4.38}$$

which yields

$$\operatorname{div}\left(\mathrm{n}^{\mathrm{F}}\lambda\mathbf{1}\right) = \lambda\operatorname{grad}\mathrm{n}^{\mathrm{F}} + \mathrm{n}^{\mathrm{F}}\operatorname{grad}\lambda. \tag{4.39}$$

We therefore have for the balance of momentum

$$-\lambda\operatorname{grad}\mathrm{n}^{\mathrm{F}} - \mathrm{n}^{\mathrm{F}}\operatorname{grad}\lambda + \rho^{\mathrm{F}}\mathbf{b} + \lambda\operatorname{grad}\mathrm{n}^{\mathrm{F}} - \mathbf{S}_{\mathrm{F}}\mathbf{w}_{\mathrm{FS}} = 0. \tag{4.40}$$

Making use of $\rho^{\mathrm{F}} = \mathrm{n}^{\mathrm{F}}\rho^{\mathrm{FR}}$ and rearranging the above we have for the seepage velocity

$$\mathrm{n}^{\mathrm{F}}\mathbf{w}_{\mathrm{FS}} = \frac{\left(\mathrm{n}^{\mathrm{F}}\right)^2}{\alpha_{\mathrm{F0}}}\left[(1-\alpha_{\mathrm{F}})\,\mathbf{1} + \alpha_{\mathrm{F}}\mathbf{M}_0\right]\left(-\mathrm{grad}\lambda + \rho^{\mathrm{FR}}\mathbf{b}\right). \tag{4.41}$$

In the reference configuration, the seepage velocity is as follows:

$$\begin{aligned}\mathrm{n}^{\mathrm{F}}\mathbf{w}_{\mathrm{FS0}} &= \mathrm{n}^{\mathrm{F}}\mathrm{J}_{\mathrm{S}}\mathbf{F}_{\mathrm{S}}^{-1}\mathbf{w}_{\mathrm{FS}} &(4.42)\\ &= \frac{\left(\mathrm{n}^{\mathrm{F}}\right)^2}{\alpha_{\mathrm{FS}}}\mathrm{J}_{\mathrm{S}}\mathbf{F}_{\mathrm{S}}^{-1}\left[(1-\alpha_{\mathrm{F}})\,\mathbf{1} + \alpha_{\mathrm{F}}\mathbf{M}\right]\left(-\mathrm{grad}\lambda + \rho^{\mathrm{FR}}\mathbf{b}\right). &(4.43)\end{aligned}$$

With the use of $\mathrm{grad}\lambda = \mathrm{Grad}\lambda\,\mathbf{F}_{\mathrm{S}}^{-1}$ and the factor $\alpha_{\mathrm{F}} = 1$, the final seepage velocity in the reference configuration yields:

$$\mathrm{n}^{\mathrm{F}}\mathbf{w}_{\mathrm{FS0}} = \frac{\left(\mathrm{n}^{\mathrm{F}}\right)^2}{\alpha_{\mathrm{FS}}}\mathrm{J}_{\mathrm{S}}\,\mathbf{M}_0\left(-\mathrm{Grad}\lambda + \rho^{\mathrm{FR}}\mathbf{b}\right). \tag{4.44}$$

In order to determine the material parameter α_{FS}, the following two options may be used (Ricken et al. [87]):

$$\frac{\left(\mathrm{n^F}\right)^2}{\alpha_{\mathrm{FS}}} = \frac{\mathrm{K_{0S}^S}}{\mu^{\mathrm{FR}}}\left[\frac{\mathrm{n^F}}{\mathrm{n^F_{0F}}}\right]^{\mathrm{m}} \qquad \text{or} \qquad \frac{\left(\mathrm{n^F}\right)^2}{\alpha_{\mathrm{FS}}} = \frac{\mathrm{K_{0S}^F}}{\gamma^{\mathrm{FR}}}\left[\frac{\mathrm{n^F}}{\mathrm{n^F_{0F}}}\right]^{\mathrm{m}} \tag{4.45}$$

where $\mathrm{K_{0S}^S}$ is the intrinsic solid permeability ($\mathrm{m^2}$), μ^{FR} is the dynamic viscosity ($\mathrm{N \cdot s/m^2}$), $\mathrm{K_{0S}^F}$ is the *Darcy* permeability (m/s), γ^{FR} is the bulk density of the fluid ($\mathrm{N/m^3}$) and m is a dimensionless parameter which accounts for the change of permeability due to deformation. With the use of eq. $(4.45)_2$, the seepage velocity takes the form of

$$\mathrm{n^F}\mathbf{w}_{\mathrm{FS0}} = \mathrm{K^F}\left[\frac{\mathrm{n^F}}{\mathrm{n^F_{0F}}}\right]^{\mathrm{m}} \mathrm{J_S}\,\mathbf{M}_0\left(-\mathrm{Grad}\lambda + \rho^{\mathrm{FR}}\mathbf{b}\right). \tag{4.46}$$

where the combination of the terms $\mathrm{K_{0S}^F}/\gamma^{\mathrm{FR}}$ leads to the simplified permeability term $\mathrm{K^F}\,[\mathrm{m^4}/\left(\mathrm{N \cdot s}\right)]$. The term related to the volume fractions allows for a change in initial permeability due to a change in pore space and interstitial fluid volume, which has been shown by Dongaonkar et al. [30] to significantly decrease the hearts function and is required to be accounted for.

4.2.4 Mass exchange

With the absence of a nutrient phase within the model, it is assumed that the mass exchange only acts between the solid and fluid phase, meaning that no external source terms are considered such that $\hat{\rho}^{\mathrm{S}} = -\hat{\rho}^{\mathrm{L}}$. Following the evaluation of the entropy inequality, and making use of the postulations proposed by Ricken et al. [86], the mass supply term is formulated directly due to a lack of knowledge available in the formulation of the liquid free energy function. Therefore, in light of a stretch driven mass supply function, the following postulation is made:

$$\hat{\rho}^{\mathrm{S}} = \hat{\rho}^{\mathrm{S}}\left(\epsilon^{\mathrm{e}}\right) \tag{4.47}$$

where ϵ^{e} is the elastic cardiomyocyte stretch. Here it is assumed that cardiac dilation is a non-reversible process, and as such it is not necessary that the mass supply is able to change signs, leading to only a positive mass supply from the liquid phase to the solid (see figure 4.1). In order to define the stretch dependency on the mass exchange, a growth function $\mathrm{k^g}$ suggested by Göktepe et al. [42] is introduced as

$$\mathrm{k^g} = \frac{1}{\tau}\left[\frac{\epsilon^{\max} - \phi}{\epsilon^{\max} - 1}\right]^{\gamma} \tag{4.48}$$

where τ denotes the adaptation speed, γ calibrates the shape of the adaptation curve and ϕ is a growth criterion defined as

$$\phi = 1 + \epsilon^{\mathrm{e}} - \epsilon^{\mathrm{c}} \tag{4.49}$$

which is linked to a restriction such that growth only occurs if the elastic stretch of the cardiomyocyte exceeds a critical threshold ϵ^{c}:

$$\hat{\rho}^{\mathrm{S}} = \begin{cases} \hat{\rho}^{\mathrm{S}}\left\{\epsilon^{e}\right\}, & \text{if } \epsilon^{\mathrm{e}} > \epsilon^{\mathrm{c}} \\ 0, & \text{if } \epsilon^{\mathrm{e}} < \epsilon^{\mathrm{c}} \text{ or } \hat{\rho}^{\mathrm{S}} > \hat{\rho}^{\mathrm{S}}_{\max} \end{cases} \tag{4.50}$$

where the maximum pathological cardiomyocyte stretch is defined as $\epsilon^{\max}$. The mass supply is thus linked to the stretch via the growth function with the definition

$$\hat{\rho}^{\mathrm{S}} = \hat{\rho}^{\mathrm{S}}_{\max}\left(1 - \mathrm{k}^{\mathrm{g}}\right) \tag{4.51}$$

where $\hat{\rho}^{\mathrm{S}}_{\max}$ $[\mathrm{kg}/(\mathrm{s}\cdot\mathrm{m}^3)]$ is a scaling factor, leading to the formal definition of the mass supply as:

$$\hat{\rho}^{\mathrm{S}} = \hat{\rho}^{\mathrm{S}}_{\max}\left\{1 - \frac{1}{\tau}\left[\frac{\epsilon^{\max} - \phi}{\epsilon^{\max} - 1}\right]^{\gamma}\right\}. \tag{4.52}$$

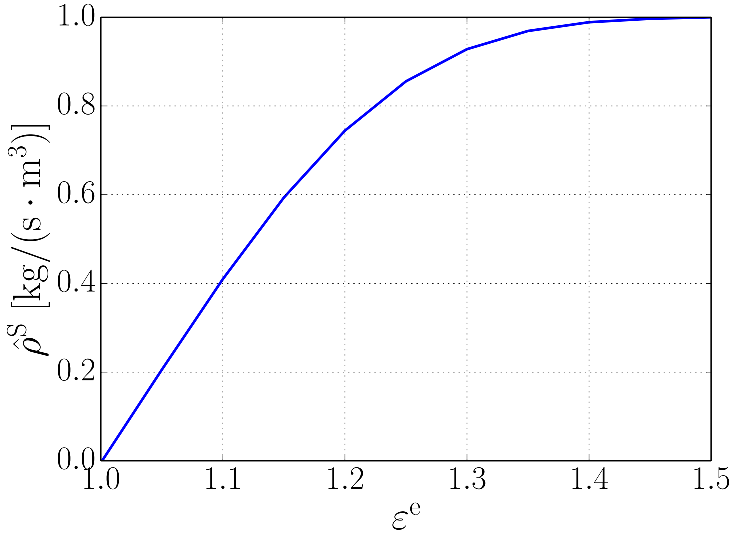

Figure 4.1. Mass transfer rate - showing the dependency of the mass supply on the elastic cardiomyocyte stretch - for the case where $\hat{\rho}^{\mathrm{S}}_{\max} = 1$ $[\mathrm{kg}/(\mathrm{s}\cdot\mathrm{m}^3)]$, $\epsilon^{\mathrm{c}} = 1.001$, $\epsilon^{\max} = 1.5$, $\tau = 1$ and $\gamma = 4$. The value of $\hat{\rho}^{\mathrm{S}}_{\max}$ is later calibrated during patient specific investigation, while the remaining constants have been taken from Göktepe et al. [42].

4.3 Weak forms for the biphasic approach

In the following, the weak forms for the biphasic model are developed addressing the balance of momentum and mass for the mixture, and additionally the balance of mass for the solid phase.

4.3.1 Weak form of the balance of momentum

From eq. (3.71), and combining eq. $(4.7)_1$ and eq. $(4.7)_2$ making use of eq. (4.46) and casting the result in integral form we obtain the global form of the balance of momentum for the mixture for a biphasic problem:

$$\int_{\mathrm{B_S}} \left\{ \operatorname{div} \mathbf{T} + \left(\rho^{\mathrm{S}} + \rho^{\mathrm{F}}\right) \mathbf{b} - \hat{\rho}^{\mathrm{S}} \mathbf{w}_{\mathrm{FS}} \right\} \mathrm{dv} = \mathbf{0}, \tag{4.53}$$

where use has been made of the relations stipulated in eq. $(4.24)_2$ and eq. (4.25) where $\mathbf{w}_{\mathrm{FS}} = \mathbf{x}'_{\mathrm{F}} - \mathbf{x}'_{\mathrm{S}}$. In the case of cardiac growth, changes due to volume overload generally occur over a long enough time period such that it is reasonable to assume that the momentum production due to growth is negligible in relation to the stress and body force terms; thus for the balance of momentum it is assumed that $\hat{\rho}^{\mathrm{S}} \mathbf{w}_{\mathrm{FS}} \approx \mathbf{0}$. Therefore, under consideration of the abbreviations

$$\mathbf{T} = \mathrm{J_S^{-1}} \mathbf{F}_{\mathrm{S}} \, \mathbf{S} \, \mathbf{F}_{\mathrm{S}}^{\mathrm{T}} \qquad \text{and} \qquad \overset{+}{\mathbf{F}}_{\mathrm{S}} = \mathbf{F}_{\mathrm{S}}^{-\mathrm{T}} \mathrm{J_S}, \tag{4.54}$$

and the transport theorems

$$\mathrm{d}\mathbf{a} = \overset{+}{\mathbf{F}}_{\mathrm{S}} \, \mathrm{d}\mathbf{A}_{0\mathrm{S}} = \mathrm{J_S} \mathbf{F}_{\mathrm{S}}^{-\mathrm{T}} \, \mathrm{dA_{0S}} \qquad \text{and} \qquad \mathrm{dv} = \mathrm{J_S} \, \mathrm{dV_{0S}}, \tag{4.55}$$

the global form of the balance of momentum reads

$$\int_{\mathrm{B_S}} \operatorname{div} \mathbf{T} + \left(\rho^{\mathrm{S}} + \rho^{\mathrm{F}}\right) \mathbf{b} \, \mathrm{dv} = \int_{\mathrm{B_{0S}}} \operatorname{Div} \mathbf{P} + \left(\rho^{\mathrm{S}} + \rho^{\mathrm{F}}\right) \mathrm{J_S} \mathbf{b} \, \mathrm{dV_{0S}} = \mathbf{0} \tag{4.56}$$

which is multiplied by the arbitrary test function $\delta \mathbf{u}_{\mathrm{S}}$

$$\int_{\mathrm{B_{0S}}} \left\{ \operatorname{Div} \mathbf{P} \cdot \delta \mathbf{u}_{\mathrm{S}} + \left(\rho^{\mathrm{S}} + \rho^{\mathrm{F}}\right) \mathrm{J_S} \mathbf{b} \cdot \delta \mathbf{u}_{\mathrm{S}} \right\} \mathrm{dV_{0S}} = 0. \tag{4.57}$$

With the use of *Gauss's* [2] divergence theorem we find its corresponding weak form:

$$\begin{aligned}
&\int_{\mathrm{B_{0S}}} \mathbf{P} : \operatorname{Grad}(\delta \mathbf{u}_{\mathrm{S}}) \, \mathrm{dV_{0S}} - \int_{\mathrm{B_{0S}}} \left(\mathrm{n^S} \rho^{\mathrm{SR}} + \mathrm{n^F} \rho^{\mathrm{FR}}\right) \mathrm{J_S} \mathbf{b} \cdot \delta \mathbf{u}_{\mathrm{S}} \, \mathrm{dV_{0S}} - \\
&\qquad - \int_{\mathrm{B_{0S}}} \operatorname{Div} \left(\mathbf{P}^{\mathrm{T}} \delta \mathbf{u}_{\mathrm{S}}\right) \mathrm{dV_{0S}} \\
&= \int_{\mathrm{B_{0S}}} \mathbf{P} : \operatorname{Grad}(\delta \mathbf{u}_{\mathrm{S}}) \, \mathrm{dV_{0S}} - \int_{\mathrm{B_{0S}}} \left(\mathrm{n^S} \rho^{\mathrm{SR}} + \mathrm{n^F} \rho^{\mathrm{FR}}\right) \mathrm{J_S} \mathbf{b} \cdot \delta \mathbf{u}_{\mathrm{S}} \, \mathrm{dV_{0S}} - \\
&\qquad - \int_{\partial \mathrm{B_{0S}}} \mathbf{P} \mathbf{n}_{0\mathrm{S}} \cdot \delta \mathbf{u}_{\mathrm{S}} \, \mathrm{dA_{0S}} = 0
\end{aligned} \tag{4.58}$$

where $\mathbf{n}_{0\mathrm{S}}$ denotes the outward orientated unit surface normal acting on $\partial \mathrm{B_{0S}}$. Reformulating the stress in order of the second *Piola-Kirchhoff* stress yields

---

[2] Johann CF Gauss (1777 - 1855): German mathematician and son of illiterate parents who contributed to a multitude of fields, with one of his most notable discoveries being the prediction of when the asteroid *Ceres* would next appear in the sky. He was been referred to as *princeps mathematicorum*, Latin for the *prince of mathematics*.

$$\mathrm{G}^{\mathrm{mix}}_{\mathrm{mom}} = \int_{\mathrm{B_{0S}}} \mathbf{S} : \delta\mathbf{E}_{\mathrm{S}}\,\mathrm{dV_{0S}} - \int_{\mathrm{B_{0S}}} \left(\mathrm{n^S}\rho^{\mathrm{SR}} + \mathrm{n^F}\rho^{\mathrm{FR}}\right) \mathrm{J_S}\mathbf{b}\cdot\delta\mathbf{u}_{\mathrm{S}}\,\mathrm{dV_{0S}} - \\ - \int_{\partial\mathrm{B_{0S}}} \mathbf{p}_0\cdot\delta\mathbf{u}_{\mathrm{S}}\,\mathrm{dA_{0S}} = 0 \tag{4.59}$$

where the traction vector in the reference configuration reads $\mathbf{p}_0 = \mathbf{p}_{\mathrm{S0}} + \mathbf{p}_{\mathrm{F0}} = \mathbf{P}\,\mathbf{n}_{\mathrm{0S}}$; which is further formulated in terms of the right *Cauchy-Green* deformation tensor for the stress term yielding the final balance of momentum in the reference configuration:

$$\mathrm{G}^{\mathrm{mix}}_{\mathrm{mom}} = \int_{\mathrm{B_{0S}}} \frac{1}{2}\mathbf{S} : \delta\mathbf{C}_{\mathrm{S}}\,\mathrm{dV_{0S}} - \int_{\mathrm{B_{0S}}} \left(\mathrm{n^S}\rho^{\mathrm{SR}} + \mathrm{n^F}\rho^{\mathrm{FR}}\right) \mathrm{J_S}\mathbf{b}\cdot\delta\mathbf{u}_{\mathrm{S}}\,\mathrm{dV_{0S}} - \\ - \int_{\partial B_{0S}} \mathbf{p}_0\cdot\delta\mathbf{u}_{S}\,\mathrm{dA_{0S}} = 0, \tag{4.60}$$

which is sufficient to solve for the unknown displacement field $\mathbf{u}_{\mathrm{S}}$.

4.3.2 Weak forms of the balance of mass

In addition to the unknown displacement field well known in conventional solid mechanics, the *Lagrange* multiplier λ and the solid volume fraction $\mathrm{n^S}$ contribute two additional unknown quantities to the equation system. With regards to the volume fractions, the usual expression $\mathrm{n}^\alpha = \mathrm{n}^\alpha_{0\alpha}\mathrm{J_S^{-1}}$ obtained from integration of the local balance of mass is not admissible due to the inclusion of the mass supply terms $\hat{\rho}^\alpha$. However, making use of the saturation condition, only one unknown volume fraction exists, where the fluid volume fraction may be solved using the relation $\mathrm{n^F} = 1 - \mathrm{n^S}$. As such, the balance of mass for the mixture is considered with relation to the unknown pore pressure, and the balance of mass for the solid phase is considered for the unknown solid volume fraction.

Balance of mass for the mixture

Combining eq. (4.6)$_1$ and eq. (4.6)$_2$ and casting the result in integral form we obtain the global form of the balance of mass for the mixture for a biphasic problem:

$$\int_{\mathrm{B_S}} \left\{ \left(\mathrm{n^S}\right)'_{\mathrm{S}} + \left(\mathrm{n^F}\right)'_{\mathrm{F}} + \mathrm{n^S}\mathrm{div}\,\mathbf{x}'_{\mathrm{S}} + \mathrm{n^F}\mathrm{div}\,\mathbf{x}'_{\mathrm{F}} - \frac{\hat{\rho}^{\mathrm{S}}}{\rho^{\mathrm{SR}}} - \frac{\hat{\rho}^{\mathrm{F}}}{\rho^{\mathrm{FR}}} \right\} \mathrm{dv} = 0. \tag{4.61}$$

With the material time derivative of the saturation condition from eq. (4.12) as

$$\left(\mathrm{n^S}\right)'_{\mathrm{S}} + \left(\mathrm{n^F}\right)'_{\mathrm{F}} - \mathrm{grad}\mathrm{n^F}\cdot\mathbf{w}_{\mathrm{FS}} = 0, \tag{4.62}$$

and making use of the relation $\hat{\rho}^{\mathrm{S}} = -\hat{\rho}^{\mathrm{F}}$ we have

$$\int_{\mathrm{B_S}} \left\{ \mathrm{grad}(\mathrm{n^F})\cdot\mathbf{w}_{\mathrm{FS}} + \mathrm{n^S}\mathrm{div}\,\mathbf{x}'_{\mathrm{S}} + \mathrm{n^F}\mathrm{div}\,\mathbf{x}'_{\mathrm{F}} + \hat{\rho}^{\mathrm{S}}\left(\frac{1}{\rho^{\mathrm{FR}}} - \frac{1}{\rho^{\mathrm{SR}}}\right) \right\} \mathrm{dv} = 0. \tag{4.63}$$

We now consider the relation

$$\mathrm{div}\,\left(\mathrm{n}^\mathrm{F}\mathbf{w}_\mathrm{FS}\right) = \mathrm{grad}(\mathrm{n}^\mathrm{F}) \cdot \mathbf{w}_\mathrm{FS} + \mathrm{n}^\mathrm{F}\ \mathrm{div}\ \left(\mathbf{x}'_\mathrm{F}\right) - \mathrm{n}^\mathrm{F}\mathrm{div}\ \left(\mathbf{x}'_\mathrm{S}\right) \tag{4.64}$$

which yields

$$\mathrm{grad}(\mathrm{n}^\mathrm{F}) \cdot \mathbf{w}_\mathrm{FS} = \mathrm{div}\,\left(\mathrm{n}^\mathrm{F}\mathbf{w}_\mathrm{FS}\right) + \mathrm{n}^\mathrm{F}\ \mathrm{div}\ \mathbf{x}'_\mathrm{S} - \mathrm{n}^\mathrm{F}\ \mathrm{div}\ \mathbf{x}'_\mathrm{F}. \tag{4.65}$$

Therefore, we have

$$\begin{aligned} &\int_{\mathrm{B_S}} \left\{\mathrm{grad}(\mathrm{n}^\mathrm{F}) \cdot \mathbf{w}_\mathrm{FS} + \mathrm{n}^\mathrm{S}\ \mathrm{div}\ \mathbf{x}'_\mathrm{S} + \mathrm{n}^\mathrm{F}\ \mathrm{div}\ \mathbf{x}'_\mathrm{F}\right\} \mathrm{dv} \\ &= \int_{\mathrm{B_S}} \left\{\mathrm{div}\,\left(\mathrm{n}^\mathrm{F}\mathbf{w}_\mathrm{FS}\right) + \left(\mathrm{n}^\mathrm{F} + \mathrm{n}^\mathrm{S}\right)\ \mathrm{div}\ \mathbf{x}'_\mathrm{S}\right\} \mathrm{dv} = 0, \end{aligned} \tag{4.66}$$

which leads to the strong form for the balance of mass of the mixture:

$$\int_{\mathrm{B_S}} \left\{\mathrm{div}\ \left(\mathbf{x}'_\mathrm{S} + \mathrm{n}^\mathrm{F}\mathbf{w}_\mathrm{FS}\right) + \hat{\rho}^\mathrm{S}\left(\frac{1}{\rho^\mathrm{FR}} - \frac{1}{\rho^\mathrm{SR}}\right)\right\}\mathrm{dv} = 0. \tag{4.67}$$

Furthermore, making use of *Greens's* theorem yields

$$\int_{\partial\mathrm{B_S}} \left(\mathbf{x}'_\mathrm{S} + \mathrm{n}^\mathrm{F}\mathbf{w}_\mathrm{FS}\right)\ \mathrm{d}\mathbf{a} + \hat{\rho}^\mathrm{S}\left(\frac{1}{\rho^\mathrm{FR}} - \frac{1}{\rho^\mathrm{SR}}\right)\mathrm{dv} = 0, \tag{4.68}$$

and making use of eq. (4.55) allows the balance of mass to be formulated in the reference configuration as

$$\int_{\partial\mathrm{B_{0S}}} \left(\mathbf{x}'_\mathrm{S} + \mathrm{n}^\mathrm{F}\mathbf{w}_\mathrm{FS}\right) \overset{+}{\mathbf{F}}_\mathrm{S}\ \mathrm{d}\mathbf{A}_\mathrm{0S} + \int_{\mathrm{B_{0S}}} \mathrm{J_S}\,\hat{\rho}^\mathrm{S}\left(\frac{1}{\rho^\mathrm{FR}} - \frac{1}{\rho^\mathrm{SR}}\right)\mathrm{dV_{0S}} = 0. \tag{4.69}$$

Additionally, making use of eq. (4.54) and once again *Green's* theorem, yields for the reference configuration:

$$\begin{aligned} &\int_{\partial\mathrm{B_{0S}}} \mathrm{J_S}\left(\mathbf{x}'_\mathrm{S} + \mathrm{n}^\mathrm{F}\mathbf{w}_\mathrm{FS}\right)\mathbf{F}_\mathrm{S}^{-\mathrm{T}}\ \mathrm{d}\mathbf{A}_\mathrm{0S} + \int_{\mathrm{B_{0S}}} \mathrm{J_S}\,\hat{\rho}^\mathrm{S}\left(\frac{1}{\rho^\mathrm{FR}} - \frac{1}{\rho^\mathrm{SR}}\right)\mathrm{dV_{0S}} \\ &= \int_{\mathrm{B_{0S}}} \mathrm{Div}\ \left(\mathrm{J_S}\mathbf{x}'_\mathrm{S}\,\mathbf{F}_\mathrm{S}^{-\mathrm{T}} + \mathrm{J_S}\mathrm{n}^\mathrm{F}\mathbf{w}_\mathrm{FS}\,\mathbf{F}_\mathrm{S}^{-\mathrm{T}}\right)\ \mathrm{dV_{0S}} + \int_{\mathrm{B_{0S}}} \mathrm{J_S}\,\hat{\rho}^\mathrm{S}\left(\frac{1}{\rho^\mathrm{FR}} - \frac{1}{\rho^\mathrm{SR}}\right)\mathrm{dV_{0S}} = 0. \end{aligned} \tag{4.70}$$

Multiplying eq. (4.70) by an arbitrary test function $\delta\lambda$ and using the calculation rule

$$\mathrm{div}\,(\mathbf{v})\,\delta\lambda = \mathrm{div}\,(\mathbf{v}\delta\lambda) - \mathbf{v} \cdot \mathrm{grad}(\delta\lambda) \tag{4.71}$$

yields the weak form of the balance of mass for the mixture:

$$\begin{aligned}
&\int_{\mathrm{B_{0S}}} \left\{ \mathrm{Div}\left(\mathrm{J_S} \mathbf{x}'_\mathrm{S}\, \mathbf{F}_\mathrm{S}^{-\mathrm{T}} + \mathrm{J_S n^F} \mathbf{w}_\mathrm{FS}\, \mathbf{F}_\mathrm{S}^{-\mathrm{T}} \right) + \mathrm{J_S}\, \hat{\rho}^\mathrm{S} \left(\frac{1}{\rho^\mathrm{FR}} - \frac{1}{\rho^\mathrm{SR}} \right) \right\} \delta\lambda \, \mathrm{dV_{0S}} \\
&= \int_{\mathrm{B_{0S}}} \left\{ -\mathrm{n^F} \mathbf{w}_\mathrm{FS0} \cdot \mathrm{Grad}\,(\delta\lambda) + \mathrm{Div}\left(\mathrm{J_S} \mathbf{x}'_\mathrm{S} \mathbf{F}_\mathrm{S}^{-\mathrm{T}} \right) \delta\lambda + \mathrm{J_S}\, \hat{\rho}^\mathrm{S} \left(\frac{1}{\rho^\mathrm{FR}} - \frac{1}{\rho^\mathrm{SR}} \right) \delta\lambda \right\} \mathrm{dV_{0S}} + \\
&\qquad + \int_{\partial \mathrm{B_{0S}}} \mathrm{n^F} \mathbf{w}_\mathrm{FS0} \cdot \mathbf{n}_\mathrm{0S}\, \delta\lambda \, \mathrm{dA_{0S}} = 0,
\end{aligned} \tag{4.72}$$

where the relation $\mathrm{J_S n^F} \mathbf{w}_\mathrm{FS}\, \mathbf{F}_\mathrm{S}^{-\mathrm{T}} = \mathrm{n^F} \mathbf{w}_\mathrm{FS0}$ has been used for the seepage velocity. We continue with the relation

$$\int_{\mathrm{B_{0S}}} \mathrm{Div}\left(\mathbf{x}'_\mathrm{S} \mathrm{J_S} \mathbf{F}_\mathrm{S}^{-\mathrm{T}} \right) \mathrm{dV} = \int_{\mathrm{B_{0S}}} \mathrm{J_S}\, (\mathbf{E}_\mathrm{S})'_\mathrm{S} : \mathbf{C}_\mathrm{S}^{-1} \mathrm{dV}$$

where $(\mathbf{E}_\mathrm{S})'_\mathrm{S} = \mathbf{F}_\mathrm{S}^\mathrm{T} \mathbf{D}_\mathrm{S} \mathbf{F}_\mathrm{S}$ denotes the material time derivative of the *Green* strain tensor $\mathbf{E}_\mathrm{S} = \frac{1}{2}\,(\mathbf{C}_\mathrm{S} - \mathbf{1})$ (see eq. (B.2)); yielding the final weak form of the balance of mass for the mixture in the reference configuration as follows:

$$\begin{aligned}
\mathrm{G^{mix}_{mass}} =& -\int_{\mathrm{B_{0S}}} \mathrm{n^F} \mathbf{w}_\mathrm{FS0} \cdot \mathrm{Grad}\delta\lambda \mathrm{dV} + \int_{\mathrm{B_{0S}}} \mathrm{J_S}\, (\mathbf{E}_\mathrm{S})'_\mathrm{S} : \mathbf{C}_\mathrm{S}^{-1} \delta\lambda \mathrm{dV} \\
&+ \int_{\mathrm{B_{0S}}} \mathrm{J_S}\, \hat{\rho}^\mathrm{S} \left(\frac{1}{\rho^\mathrm{FR}} - \frac{1}{\rho^\mathrm{SR}} \right) \delta\lambda \mathrm{dV} + \int_{\partial \mathrm{B_{0S}}} \mathrm{n^F} \mathbf{w}_\mathrm{FS0} \cdot \mathbf{n}_\mathrm{0S} \delta\lambda \mathrm{dA} = 0
\end{aligned} \tag{4.73}$$

where, by standard continuum mechanics relations, the term related to the strain rate may be simplified to $(\mathbf{E}_\mathrm{S})'_\mathrm{S} : \mathbf{C}_\mathrm{S}^{-1} = \mathrm{tr}\, \mathbf{D}_\mathrm{S}$.

4.3.3 Balance of mass for the solid phase

For the balance of mass for the solid phase, we cast only eq. $(4.6)_1$ in integral form and obtain the global form for the balance of mass for the solid phase:

$$\mathrm{G^s_{mass}} = \int_{\mathrm{B_S}} \left\{ (\mathrm{n^S})'_\mathrm{S} + \mathrm{n^S}\, \mathrm{div}\, \mathbf{x}'_\mathrm{S} - \frac{1}{\rho^\mathrm{SR}} \hat{\rho}^\mathrm{S} \right\} \mathrm{dv} = 0, \tag{4.74}$$

which, following the methods employed for the balance of mass for the mixture and use of the test function $\delta \mathrm{n^S}$ leads to the weak form in the reference configuration as

$$\mathrm{G^s_{mass}} = \int_{\mathrm{B_{0S}}} \left\{ \mathrm{J_S} (\mathrm{n^S})'_\mathrm{S} + \mathrm{J_S n^S}\, \mathrm{tr}\, \mathbf{D}_\mathrm{S} - \frac{\mathrm{J_S}}{\rho^\mathrm{SR}} \hat{\rho}^\mathrm{S} \right\} \delta \mathrm{n^S}\, \mathrm{dV} = 0. \tag{4.75}$$

In eq. (4.75), there is no explicitly defined boundary condition, however, the initial solid volume fraction $\mathrm{n^S_{0S}}$ is applied to the body as an initial value following calculation of the solid volume fraction degree of freedom $\mathrm{n^S}$ in each time step.

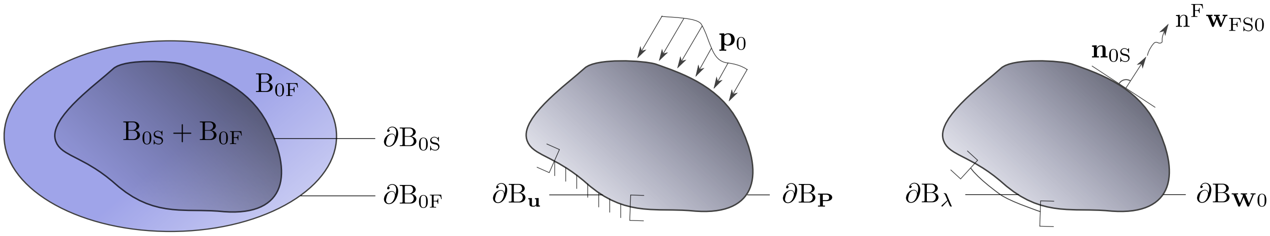

Figure 4.2. Boundary conditions of the porous body: (left) the partition of the solid body $\mathrm{B_{0S}}$ and fluid body $\mathrm{B_{0F}}$; (center) the surface partition of *Dirichlet* $^5\partial\mathrm{B}_{\mathbf{u}}$ and *Neumann* $^6\partial\mathrm{B}_{\mathbf{P}}$ boundary for displacement and traction vector respectively; (right) the surface partition for *Dirichlet* $\partial\mathrm{B}_\lambda$ and *Neumann* $\partial\mathrm{B_{W0}}$ boundary for pressure and fluid volume flux $\mathrm{e_{F0}} = \mathrm{n^F}\mathbf{w}_{\mathrm{FS0}} \cdot \mathbf{n}_{0\mathrm{S}}$ respectively.

4.4 Numerical treatment

We consider the solid body $\mathrm{B_0} = \mathrm{B_{0S}}$ with the surface $\partial\mathrm{B_0} = \partial\mathrm{B_{0S}}$, where $\mathrm{B_0} = \mathrm{B_{0S}} \cup \mathrm{B_{0F}}$, noting that in the case of the fluid $\partial\mathrm{B_{0S}}$ is a non-material surface, meaning that the material surface of the fluid $\partial\mathrm{B_{0F}}$ is always outside the body (see Figure 4.2). The given boundary values are defined with

$$\begin{array}{ll}
\mathbf{u}_\mathrm{S} = \bar{\mathbf{u}}_\mathrm{S} & \text{on } \partial\mathrm{B}_{\mathbf{u}}, \\
\mathbf{p}_0 = \mathbf{P}_{\mathrm{n_{0S}}} = \bar{\mathrm{p}} & \text{on } \partial\mathrm{B}_{\mathbf{P}}, \\
\lambda = \bar{\lambda} & \text{on } \partial\mathrm{B}_\lambda, \\
\mathrm{e_F} = \mathrm{n^F}\mathbf{w}_{\mathrm{FS0}} \cdot \mathbf{n}_{0\mathrm{S}} = \bar{\mathrm{e}}_\mathrm{F} & \text{on } \partial\mathrm{B}_{\mathbf{W}},
\end{array} \tag{4.76}$$

where $\mathbf{p}$ represents the mechanical traction vector, $\mathbf{P} = \mathbf{P}^\mathrm{S} + \mathbf{P}^\mathrm{F}$ defines the sum of stresses, $\mathbf{n}_{0\mathrm{S}}$ denotes the outward orientated normal vector and $\mathrm{e_F}$ is the fluid volume flux. Under consideration of the constitutive relations, the biphasic mixture body can be described by a three field problem with the set $\mathcal{U}$ of unknown quantities, where

$$\mathcal{U} = \left\{\mathbf{u}_S, \lambda, \mathrm{n^S}\right\}. \tag{4.77}$$

The structure of the linearised weak formulations of the field equations is given according to the general form

$$(\delta\varphi)^\mathrm{T}\left(\mathrm{D}\mathbf{K} + \mathrm{D}\dot{\mathbf{K}}\right) = (\delta\varphi)^\mathrm{T}\left(\mathbf{b} + \mathbf{R}^{\partial\mathrm{B_{0S}}}\right), \tag{4.78}$$

wherein the transpose vector of the variation of the unknown field quantities $(\delta\varphi)^\mathrm{T}$ multiplied by $\mathrm{D}\mathbf{K}$ and $\mathrm{D}\dot{\mathbf{K}}$ represent the share of stiffness and the share of damping, respectively, which are given as

$$\mathrm{D}\mathbf{K} = \begin{bmatrix} \mathrm{MO}_{,\mathbf{u_s}} & \mathrm{MO}_{,\lambda} & \mathrm{MO}_{,\mathrm{n^S}} \\ \mathrm{MA}_{,\mathbf{u_s}} & \mathrm{MA}_{,\lambda} & \mathrm{MA}_{,\mathrm{n^S}} \\ \mathrm{MA^S}_{,\mathbf{u_s}} & \mathrm{MA^S}_{,\lambda} & \mathrm{MA^S}_{,\mathrm{n^S}} \end{bmatrix} \begin{bmatrix} \Delta\mathbf{u}_\mathrm{s} \\ \Delta\lambda \\ \Delta\mathrm{n^S} \end{bmatrix} \quad \text{and} \quad \mathrm{D}\dot{\mathbf{K}} = \begin{bmatrix} 0 & 0 & 0 \\ \mathrm{MA}_{,\mathbf{u_s}} & 0 & 0 \\ \mathrm{MA^S}_{,\mathbf{u_s}} & 0 & 0 \end{bmatrix} \begin{bmatrix} \Delta\mathbf{u}_\mathrm{s} \\ \Delta\lambda \\ \Delta\mathrm{n^S} \end{bmatrix}, \tag{4.79}$$

wherein the quantities MO, MA and $\mathrm{MA^S}$ represent the weak formulations of the balance equations of momentum and mass with eq. (4.60) = MO, eq. (4.73) = MA and eq. (4.75) = $\mathrm{MA^S}$, with the subscripts $\mathbf{u}_\mathrm{S}$, λ and $\mathrm{n^S}$ representing the quantities which the balance equations were linearised with respect to. Furthermore, **b** denotes the vector of known quantities, which are in this case the body forces, and $\mathbf{R}^{\partial \mathrm{B_{0S}}}$ represents the vector concerning the boundary conditions acting on the surface $\partial\mathrm{B_{0S}}$ of the porous body $\mathrm{B_{0S}}$, where

$$\mathbf{R}^{\partial \mathrm{B_{0S}}} = \begin{bmatrix} \mathrm{R^{MO}} \\ \mathrm{R^{MA}} \\ \mathrm{R^{MA^S}} \end{bmatrix} = \begin{bmatrix} \mathbf{p}_{0\mathrm{S}} \\ \mathrm{e}_{\mathrm{F_{0S}}} \\ 0 \end{bmatrix} \tag{4.80}$$

where the boundary conditions $\mathbf{p}_0 = \mathbf{p}_{\mathrm{S}0} + \mathbf{p}_{\mathrm{F}0} = \mathbf{P}\,\mathbf{n}_{0\mathrm{S}}$ and $\mathbf{n}_{0\mathrm{S}}$ the outward orientated unit surface normal on the boundary $\partial\mathrm{B_{0S}}$, and where the fluid mass efflux $\mathrm{e}_{\mathrm{F_{0S}}} = \mathrm{n^F}\,\mathrm{J_S}\mathbf{F}_\mathrm{S}^{-1}\mathbf{w}_\mathrm{FS}\cdot\mathbf{n}_{0\mathrm{S}}$ acts on the *Neumann* boundary in the reference configuration acting also on the boundary $\partial\mathrm{B_{0S}}$. In the case of a three dimensional problem with five degrees of freedom, D**K** is implemented as follows:

$$\mathrm{D}\mathbf{K} = \begin{bmatrix} \mathrm{MO},_{\mathrm{u_S}} & \mathrm{MO},_{\mathrm{u_S}} & \mathrm{MO},_{\mathrm{u_S}} & \mathrm{MO},_{\lambda} & \mathrm{MO},_{\mathrm{n^S}} \\ \mathrm{MO},_{\mathrm{u_S}} & \mathrm{MO},_{\mathrm{u_S}} & \mathrm{MO},_{\mathrm{u_S}} & \mathrm{MO},_{\lambda} & \mathrm{MO},_{\mathrm{n^S}} \\ \mathrm{MO},_{\mathrm{u_S}} & \mathrm{MO},_{\mathrm{u_S}} & \mathrm{MO},_{\mathrm{u_S}} & \mathrm{MO},_{\lambda} & \mathrm{MO},_{\mathrm{n^S}} \\ \mathrm{MA},_{\mathrm{u_S}} & \mathrm{MA},_{\mathrm{u_S}} & \mathrm{MA},_{\mathrm{u_S}} & \mathrm{MA},_{\lambda} & \mathrm{MA},_{\mathrm{n^S}} \\ \mathrm{MA}^\mathrm{S},_{\mathrm{u_S}} & \mathrm{MA}^\mathrm{S},_{\mathrm{u_S}} & \mathrm{MA}^\mathrm{S},_{\mathrm{u_S}} & \mathrm{MA}^\mathrm{S},_{\lambda} & \mathrm{MA}^\mathrm{S},_{\mathrm{n^S}} \end{bmatrix} \begin{bmatrix} \Delta\mathrm{u_s} \\ \Delta\mathrm{u_s} \\ \Delta\mathrm{u_s} \\ \Delta\lambda \\ \Delta\mathrm{n^S} \end{bmatrix} \tag{4.81}$$

where the balance equations are linearised analytically in the following manner:

$$\mathit{\Delta}\mathrm{G} = \frac{\partial\mathrm{G}}{\partial\mathbf{u}_\mathrm{S}}\Delta\mathbf{u}_\mathrm{S} + \frac{\partial\mathrm{G}}{\partial\lambda}\Delta\lambda + \frac{\partial\mathrm{G}}{\partial\mathrm{n^S}}\Delta\mathrm{n^S} \qquad \text{where} \qquad \mathrm{G} = \mathrm{G^{mix}_{mom}} + \mathrm{G^{mix}_{mass}} + \mathrm{G^{S}_{mass}}. \tag{4.82}$$

Due to the non-linearity of the equation system given in eq. (4.78), the system is solved incrementally and iteratively employing the *Newton* [7]-*Raphson* [8] technique.

4.4.1 Time discretisation

In order to ensure a stable finite element approximation, the Newmark method [75] is employed for time discretisation purposes making use of a linear interpolation between discrete time steps. Therefore, the following *Newmark* parameters are defined as

$$\alpha = \frac{1}{4} \qquad \text{and} \qquad \beta = \frac{1}{2}. \tag{4.83}$$

---

[6] Johann Dirichlet (1805 - 1859): German mathematician who made significant contributions to number theory and is credited with the accolade of being one of the first mathematicians to give the modern formal definition of a function.

[6] Carl Neumann (1832 - 1925): German mathematician who dealt with physical problems and was honoured with membership to several academies such as the Berlin Academy.

[7] Isaac Newton (1642 - 1727): English physicist and mathematician credited for his theory of gravity and as one of the great minds of the 17th century Scientific Revolution.

[8] Joseph Raphson (1668 - 1715, unconfirmed): English mathematician mostly known for the Newton-Raphson method, but was however made a member of the Royal Society in 1689 two years before he graduated from Jesus College, Cambridge in 1692.

Temporary displacement, velocity and acceleration variables, $\bar{\mathbf{u}}_{\mathrm{S(t)}}$, $\bar{\mathbf{v}}_{\mathrm{S(t)}}$ and $\bar{\mathbf{a}}_{\mathrm{S(t)}}$ respectively where $\bar{\mathbf{u}}_{\mathrm{S}}, \bar{\mathbf{v}}_{\mathrm{S}}, \bar{\mathbf{a}}_{\mathrm{S}} \in \left\{\mathbf{u}_{\mathrm{S}}, \lambda, \mathrm{n}^{\mathrm{S}}\right\}$, at time $\mathrm{t}_{\mathrm{n+1}}$ are thus is defined as

$$\bar{\mathbf{u}}_{\mathrm{S(t)}} = \bar{\mathbf{u}}_{\mathrm{S(n)}} + \Delta \mathrm{t} \bar{\mathbf{v}}_{\mathrm{S(n)}} + \frac{\Delta \mathrm{t}^2}{2}(1-2\alpha)\,\bar{\mathbf{a}}_{\mathrm{S(n)}} \qquad \text{and} \qquad \bar{\mathbf{v}}_{\mathrm{S(t)}} = \bar{\mathbf{v}}_{\mathrm{S(n)}} + \Delta \mathrm{t}(1-\beta)\,\bar{\mathbf{a}}_{\mathrm{S(n)}} \tag{4.84}$$

where $\Delta \mathrm{t}$ is the time increment, $\bar{\mathbf{v}}_{\mathrm{S(n)}}$ and $\bar{\mathbf{a}}_{\mathrm{S(n)}}$ are the velocities and accelerations in the previous converged loading step n. The acceleration and velocity at time $\mathrm{t}_{\mathrm{n+1}}$ are therefore defined respectively as

$$\bar{\mathbf{a}}_{\mathrm{S(n+1)}} = \frac{\bar{\mathbf{u}}_{\mathrm{S(n)}} - \bar{\mathbf{u}}_{\mathrm{S(t)}}}{\alpha \Delta \mathrm{t}^2} \qquad \text{and} \qquad \bar{\mathbf{v}}_{\mathrm{S(n+1)}} = \bar{\mathbf{v}}_{\mathrm{S(t)}} + \Delta \mathrm{t} \beta \bar{\mathbf{a}}_{\mathrm{S(n+1)}} \tag{4.85}$$

where the degrees of freedom at the previous converged time step is defined as $\bar{\mathbf{u}}_{\mathrm{S(n)}}$. For linearisation purposes, the following are therefore substituted into the linearised balance equations:

$$\Delta \dot{\mathbf{u}}_{\mathrm{S}} = \frac{\beta}{\alpha \Delta \mathrm{t}} \Delta \mathbf{u}_{\mathrm{S}}, \qquad \Delta \dot{\lambda} = \frac{\beta}{\alpha \Delta \mathrm{t}} \Delta \lambda \qquad \text{and} \qquad \Delta(\mathrm{n}^{\dot{\mathrm{S}}})'_{\mathrm{S}} = \frac{\beta}{\alpha \Delta \mathrm{t}} \Delta(\mathrm{n}^{\mathrm{S}})'_{\mathrm{S}} \tag{4.86}$$

where $\Delta(\Gamma)$ is the second variation the degree of freedom $\Gamma \in (\mathbf{u}, \lambda, \mathrm{n}^{\mathrm{S}})$.

4.5 Numerical examples

In order to validate the developed model, two examples of an academic nature were run for testing purposes. Initially, in order to test the performance of the TPM model with regards to the pore pressure degree of freedom, a cube under compression was used with an unsymmetric pore pressure boundary condition aimed at developing an unsymmetric pore pressure gradient. In order to validate the performance of the stretch driven growth model, a cantilever beam under axial loading was considered, inducing a stretch along the fibre axis.

4.5.1 Unsymmetric cube

The cube under compression, with problem statement outlined in Figure 4.3 is placed under an uniform compression load on the free surface, by means of a traction *Neumann* boundary condition causing a vertical displacement of $\mathrm{u}_{\mathrm{y}} = -5$ mm per loading step. The base of the cube is fixed displacement wise in all *Cartesian* [9] degrees of freedom, while one quarter of the surface is assigned a pore pressure of 0 kPa via a *Dirichlet* boundary condition, thus leaving the fluid free to leave or enter the cube at this position.

In order to verify the implementation of the first additional degree of freedom λ, along with the TPM additions to the standard mechanics which influence the displacement field $\mathbf{u}_{\mathrm{S}}$, it is essential to ensure that a sufficient pore pressure gradient is developed, and thus the *Darcy*

---

[9] René Descartes (1596 - 1650): a prominent French western philosopher and mathematician credited with invention of the Cartesian coordinate system, named after the adjectival form of the Latin translation of his surname, “Cartesian”.

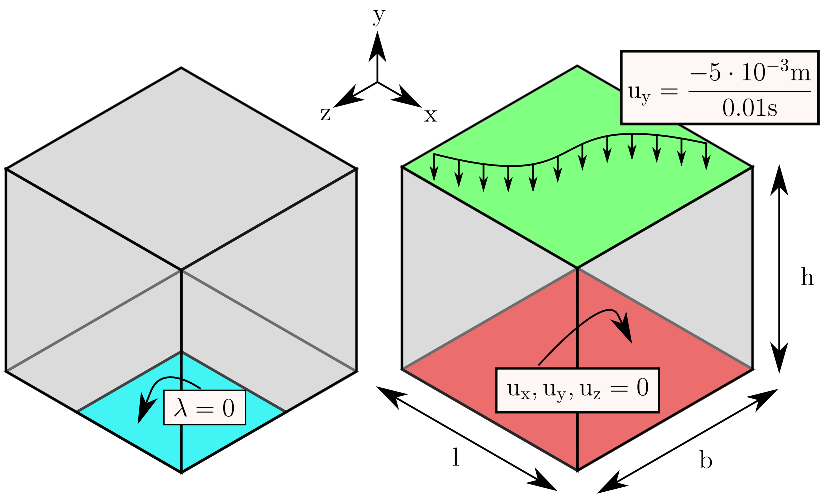

Parameter	Value	Unit
$l = b = h$	1	m
μ^S	10000	Pa
λ^S	10000	Pa
ρ_{0S}^{SR}	100	kg/m^3
ρ_{0F}^{FR}	1000	kg/m^3
n^S	0.75	–
n^L	0.25	–
K^F	⋆	$m^4/(N\cdot s)$
δt	0.01	s

⋆ varied during example

Figure 4.3. Unsymmetric compressed cube - problem statement and material parameters; showing the pore pressure boundary conditions (left), the *Neumann* and *Dirichlet* boundary conditions (middle) and material parameters (right).

permeability values were varied accordingly. Furthermore, the effect of the permeability of the pore pressure is illustrated.

In Figure 4.4 it is clear that a lower permeability illustrated by the blue line results in a larger pore pressure being developed, as the flow within the pores is hindered. In this particular example, another phenomena is illustrated by which, at a certain permeability value the flow reaches an equilibrium by which a stable pore pressure is developed following an initial increase, as seen for $K_D = 10^{-2}\ m^4/(N\cdot s)$ indicated by the red line. For a permeability value $K_D = 10^{-3}\ m^4/(N\cdot s)$ an increasing pore pressure during the simulation is observed to a value of ≈ 1 MPa, while convergence of the simulation continued quadratically, leading to the conclusion that the pore pressure degree of freedom has been implemented successfully. Additionally, the contour plots of the displacement field $\mathbf{u}_S$ illustrate the effect of pore pressure and unsymmetric flow on the mechanics of the system, showing that a lower pore pressure allows for greater displacement as expected.

Following an initial investigation into the permeability, discussion of the choice of the magnitude chosen is prudent due to its possible effects on the equation system and results. Clearly, a high magnitude of permeability results in a pressure gradient not being developed as no resistance to flow is encountered and the problem is in essence reduced to a standard solid mechanics problem as the pore pressure is negligible and tends to oscillate around zero. A second and not so clear limiting issue to the choice of permeability may also be encountered (in a problem specific manner) and requires to be fulfilled is termed the inf sup condition, referred to as the *Babuška-Brezzi* condition (cf. [14] for a detailed explanation) which is a pertinent aspect of dealing with mixed discretions and saddle point problems. The condition, presented by Babuška [10] and Brezzi [21], in the context of this investigation arises due to the term $MA,_{\lambda}$ on the diagonal entry of the stiffness matrix in eq. (4.81), which is directly associated with the permeability factor K^F. In the case that the magnitude chosen is below a certain value the stiffness matrix is ill-conditioned and computational solving of the equation

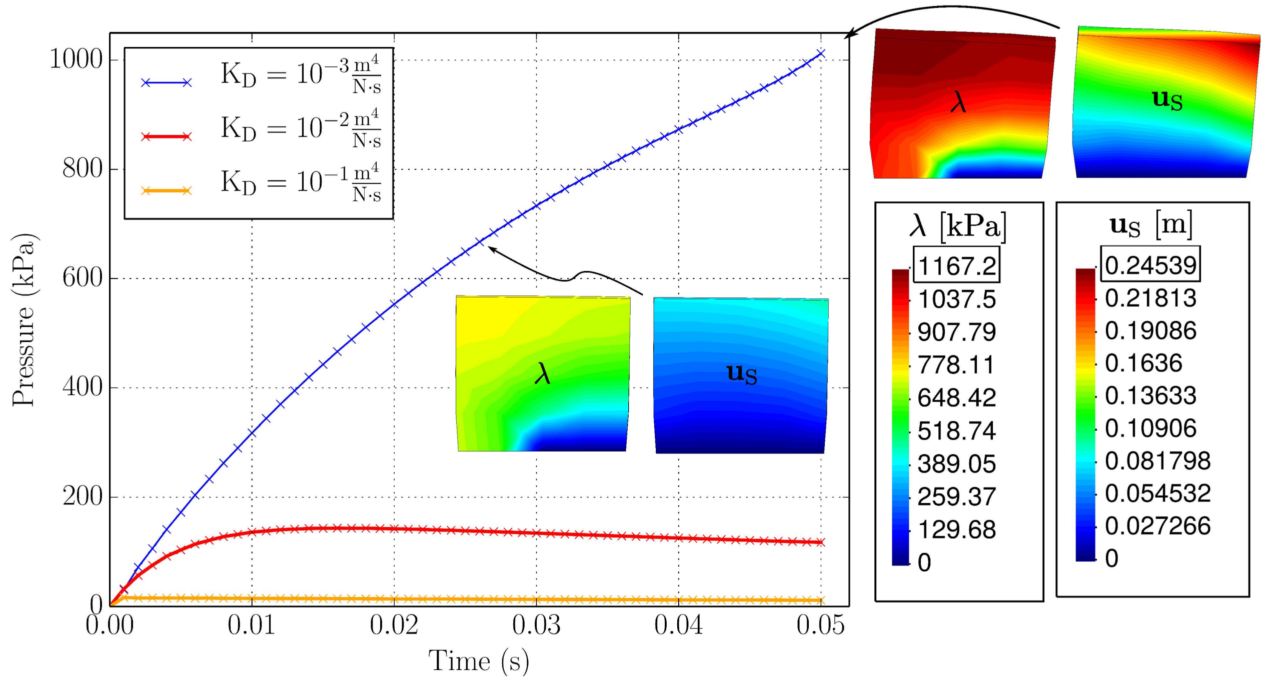

Figure 4.4. Unsymmetric compressed cube simulation results; showing the pore pressure versus time evolution for three values of permeability, along with contour plots of the pore pressure λ and displacement field $\mathbf{u}_S$ at the middle and end points of the simulation.

system fails. In this case, it is common to employ a mixed set of shape functions and use of Taylor-Hood elements (see [109]) to address the problem.

4.5.2 Axially stretched beam

Considering the degree of freedoms $\mathbf{u}_S$, λ and n^S, the beam under axial loading, with problem statement outlined in Figure 4.5, is placed under an even axial traction load on the free surface, by means of a *Neumann* boundary condition of 2 kPa / 0.01 s causing an initial displacement increment of ≈ 0.5 m per loading step; the loading increment being chosen in order to verify the numerical performance at larger loading increments. The fixed end of the beam is fixed displacement wise in all *Cartesian* degrees of freedom, while no pore pressure boundary conditions ware assigned, thus allowing no flow out of the system. The beam is loaded to 8 kPa in the positive x direction, after which the loading is incremented back to the initial value of 0 kPa, leaving only residual effects due to remodelling via a change in the volume fractions, and growth driven changes which are considered to be irreversible. Therefore, this example serves a verification purpose of the implemented volume fraction degree of freedom, the implemented growth law and additionally the visco-plastic like effects of the inclusion of the fluid via the volume fractions which do not necessarily return to the original state following unloading but rather to an optimised state. For purposes of comparison, two simulations of the beam were carried out, one for the case of no growth ($\hat{\rho}^S_{\max} = 0$) and another for the case of growth, in order to differentiate between the effects of remodelling and growth, of which the results are illustrated via the blue and red curves

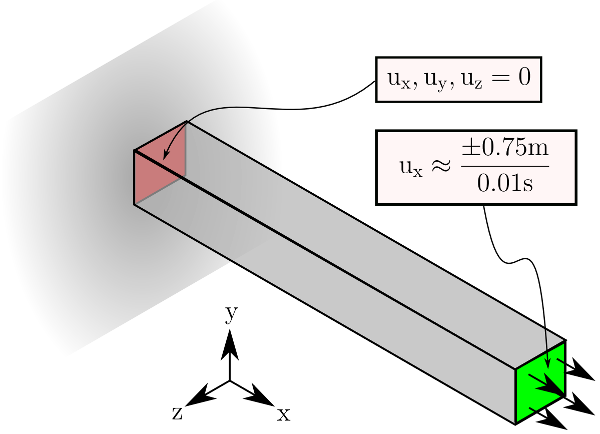

Parameter	Value	Unit
l	10	m
b = h	1	m
μ^S	10000	Pa
λ^S	10000	Pa
ρ_{0S}^{SR}	100	kg/m^3
ρ_{0F}^{FR}	1000	kg/m^3
n^S	0.5	–
n^L	0.5	–
K^F	10^{-6}	$m^4/(N \cdot s)$
$\hat{\rho}^S_{max}$	1.0	$kg/(s \cdot m^3)$
δt	0.01	s

Figure 4.5. Axially stretched beam problem statement; showing beam geometry and boundary conditions (left) and material parameters (right).

in Figure 4.6. For the case of no growth, it is clear that remodelling of the pore structure has taken place, as the end displacement of the beam does not return to its original state, as during deformation, the largest compression experienced by the beam was near the fixed end resulting in a shift of fluid to the areas of the beam under less compression due to stretch, leaving a growth-independent elongation of the beam; nothing that if a slower rate of unloading were used, a complete return to the undeformed state would be experienced, in contrast to that of the case including growth. In the case of growth, a further elongation is illustrated whereby there has been a non-reversible addition of length to the fibres aligned in the positive x direction.

During the simulations, quadratic convergence was once again observed, with meaningful values for the volume fraction degree of freedom n^S being obtained, leading to the conclusion that the fifth degree of freedom n^S has been successfully implemented within the SESKA toolbox.

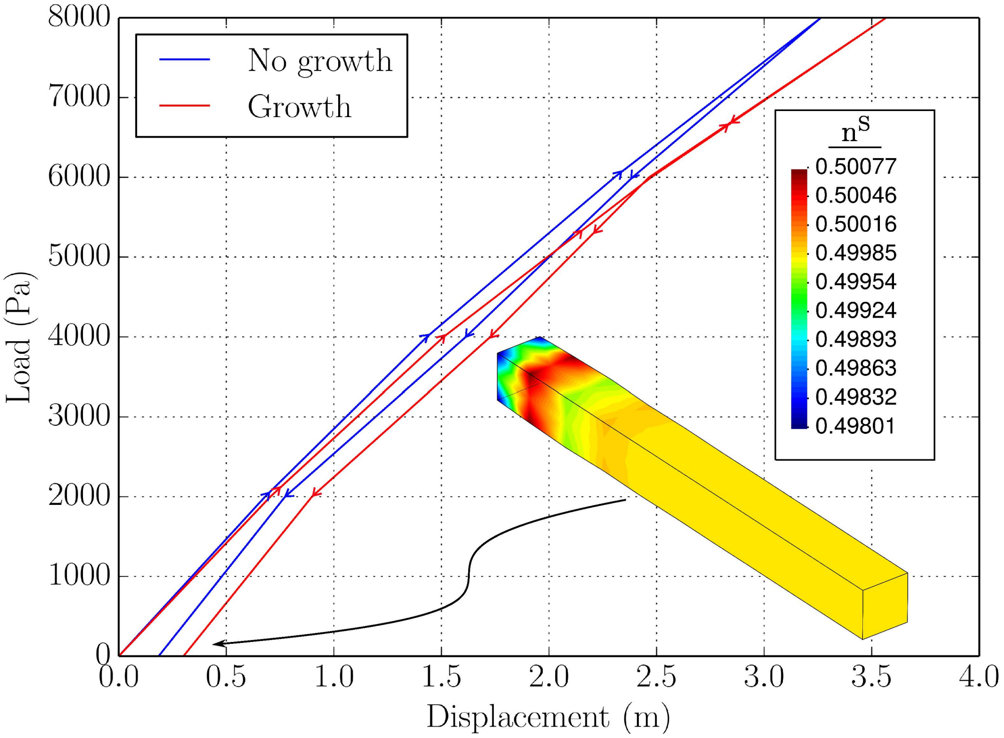

Figure 4.6. Axially stretched beam results; showing the remodelling effects in the absence of growth (blue curve) and growth effects leading to a further elongation after unloading of the beam (red curve) with an increased solid volume fraction due to growth.

Chapter 5

Cardiac mechanics

In Chapter 2, the basic physiology of the human heart has been addressed, including the general anatomical structure, behaviour, and function of the human heart. For the purposes of numerical investigation, the general behaviour is approximated via the use of cardiac specific material responses and boundary conditions which are expounded within this chapter along with certain cardiac indicators of performance which allow for conclusions to be drawn. This chapter serves as a summary of the salient aspects of the cardiac mechanics model, and by no means is an exhaustive explanation of all the involved theory. As such, for further information, the reader is referred to the works of Legner et al. [69], Skatulla and Sansour [92] and Essack [36] from which the following is drawn.

5.1 Constitutive modelling

In Chapter 4, following the evaluation of the entropy inequality, constitutive relations for the stress were developed. However, the relations were left in the form of the strain energy function ψ^{S} and thus require further treatment in order to arrive at suitable derivations for the stress of the material.

During diastolic filling, the myocardium is deformed as a response to an increased ventricular pressure via a passive manner resulting in a passive strain energy response captured with the strain energy function ψ^{S} [46]. However, with the left ventricle under concern, in order to achieve an ejection of blood and allow the cavity to return to a volume which is able to receive more blood, a ventricular pressure is required which overcomes the aortic pressure allowing the aortic valve to open [23], allowing the heart to pump blood into the circulatory system. This pressure and pumping action are achieved by an active contraction of the myocardium [2], which additively adds an additional stress to the material [11, 99], termed the active stress leading to the definition of the total second *Piola-Kirchhoff* stress as

$$\mathbf{S} = \mathbf{S}_{\mathrm{P}} + \mathbf{S}_{\mathrm{A}} \tag{5.1}$$

where $\mathbf{S}_{\mathrm{P}}$ is the passive stress and $\mathbf{S}_{\mathrm{A}}$ is the active stress. From the definition of the stress obtained in eq. (4.33) the passive stress may be formulated as

$$\mathbf{S}_{\mathrm{P}} = 2\frac{\partial \psi^{\mathrm{S}}}{\partial \mathbf{C}_{\mathrm{S}}} - \mathrm{J}_{\mathrm{S}}\lambda \mathbf{C}_{\mathrm{S}}^{-1} = \mathbf{S}_{\mathrm{E}}^{\mathrm{S}} - \mathrm{J}_{\mathrm{S}}\lambda \mathbf{C}_{\mathrm{S}}^{-1}. \tag{5.2}$$

where the effective stress $\mathbf{S}_{\mathrm{E}}^{\mathrm{S}}$ has been used. The strain energy of the myocardium is defined as

$$\psi^{\mathrm{S}} = \left(\frac{\mathrm{n}^{\mathrm{S}}}{\mathrm{n}^{\mathrm{S}}_{0\mathrm{S}}}\right)^{\mathrm{n}} \psi^{\mathrm{S}}_{\mathrm{P}} \tag{5.3}$$

where the volume fraction term has been removed from the strain energy function and appears as a pre-factor, and is understood as a stiffening of the material due to added mass (see [86]). Concerning the entropy inequality, evaluation was done with respect to the total deformation. In order to introduce a stress free intermediate configuration, the strain energy dependencies were made with respect to the elastic state of deformation, that is $\psi^{\mathrm{S}} = \psi^{\mathrm{S}}(\mathbf{C}_{\mathrm{Se}})$. Therefore, making use of the chain rule and eq. (4.19), a pull-back operation for the effective stress into the reference configuration is obtained via

$$\mathbf{S}^{\mathrm{S}}_{\mathrm{E}} = 2\frac{\partial \psi^{\mathrm{S}}}{\partial \mathbf{C}_{\mathrm{S}}} = 2\frac{\partial \psi^{\mathrm{S}}}{\partial \mathbf{C}_{\mathrm{Se}}} : \frac{\partial \mathbf{C}_{\mathrm{Se}}}{\partial \mathbf{C}_{\mathrm{S}}} = 2\mathbf{F}^{-1}_{\mathrm{Sg}} \frac{\partial \psi^{\mathrm{S}}}{\partial \mathbf{C}_{\mathrm{Se}}} \mathbf{F}^{-\mathrm{T}}_{\mathrm{Sg}} \tag{5.4}$$

where the stress is related to the intermediate configuration and elastic kinematics such that the elastic part of the second *Piola-Kirchhoff* stress tensor $\mathbf{S}_{\mathrm{Pe}} = \mathbf{S}_{\mathrm{Pe}}(\mathbf{C}_{\mathrm{Se}})$ is defined as

$$\mathbf{S}_{\mathrm{Pe}} = 2\frac{\partial \psi^{\mathrm{S}}}{\partial \mathbf{C}_{\mathrm{Se}}} \tag{5.5}$$

leading to the relation

$$\mathbf{S}^{\mathrm{S}}_{\mathrm{E}} = \mathbf{F}^{-1}_{\mathrm{Sg}} \mathbf{S}_{\mathrm{Pe}} \mathbf{F}^{-\mathrm{T}}_{\mathrm{Sg}} \tag{5.6}$$

which yields a result consistent with with similar formulations such as Göktepe et al. [42]. Concerning the active stress, it is reasonable to define the active stress as related to the stress free intermediate configuration as $\mathbf{S}_{\mathrm{Ae}} = \mathbf{S}_{\mathrm{Ae}}(\mathbf{C}_{\mathrm{Se}})$ in light of the assumption that newly deposited sarcomeres are deposited in a stress free state. Thus, the pull-back operation leads to the definition of the active stress in the reference configuration given by

$$\mathbf{S}_{\mathrm{A}} = \mathbf{F}^{-1}_{\mathrm{Sg}} \mathbf{S}_{\mathrm{Ae}} \mathbf{F}^{-\mathrm{T}}_{\mathrm{Sg}}. \tag{5.7}$$

5.1.1 Passive mechanics

In order to capture the passive behaviour of the ventricular myocardium, the mechanical model proposed by Usyk et al. [99] and reformulated in terms of strain invariants by Legner et al. [69] effectively describes the nearly incompressible orthotropic myocardial material behaviour via the following strain energy function per unit undeformed volume:

$$\psi^{\mathrm{S}}_{\mathrm{P}} = \frac{\mathrm{A}}{2}\left(\exp^{\mathrm{Q}} - 1\right) + \mathrm{A}_{\mathrm{comp}}\left(\mathrm{J}_{\mathrm{Se}} \ln\left[\mathrm{J}_{\mathrm{Se}}\right] - \mathrm{J}_{\mathrm{Se}} + 1\right), \tag{5.8}$$

where A is a stiffness factor and $\mathrm{A}_{\mathrm{comp}}$ is a constant controlling the compressibility of the myocardium. Additionally, Q is defined as

$$\mathrm{Q} = \mathrm{b}_{\mathrm{ff}} \mathrm{E}^2_{\mathrm{ff}} \mathrm{b}_{\mathrm{ss}} + \mathrm{E}^2_{\mathrm{ss}} + \mathrm{b}_{\mathrm{nn}} \mathrm{E}^2_{\mathrm{nn}} + \mathrm{b}_{\mathrm{fs}}\left(\mathrm{E}^2_{\mathrm{fs}} + \mathrm{E}^2_{\mathrm{sf}}\right) + \mathrm{b}_{\mathrm{fn}}\left(\mathrm{E}^2_{\mathrm{fn}} + \mathrm{E}^2_{\mathrm{nf}}\right) + \mathrm{b}_{\mathrm{sn}}\left(\mathrm{E}^2_{\mathrm{sn}} + \mathrm{E}^2_{\mathrm{ns}}\right), \tag{5.9}$$

where b_{ij} denote the material parameters associated with the components of the elastic part of the *Green* strain tensor $\mathbf{E}_{\mathrm{Se}} = \frac{1}{2}\left(\mathbf{C}_{\mathrm{Se}} - \mathbf{1}\right)$, relative to an orthogonal coordinate system having fibre, sheet and sheet-normals (f, s and n). Following the introduction the structural tensor $\mathbf{M}_\mathrm{f}$ in Chapter 4, additional structural tensors are defined as

$$\mathbf{M}_\mathrm{n} = \mathbf{f}_\mathrm{n} \otimes \mathbf{f}_\mathrm{n} \qquad \text{and} \qquad \mathbf{M}_\mathrm{s} = \mathbf{f}_\mathrm{s} \otimes \mathbf{f}_\mathrm{s} \tag{5.10}$$

related to the normal and sheet normal fibre directions respectively allowing the principal invariants of the elastic part of the *Green* strain tensor to be defined as

$$\begin{aligned} &\mathrm{I}_4 = \mathrm{tr}\left(\mathbf{M}_\mathrm{f}\mathbf{E}_\mathrm{Se}\right), \qquad &&\mathrm{I}_5 = \mathrm{tr}\left(\mathbf{M}_\mathrm{f}\mathbf{E}_\mathrm{Se}^2\right), \qquad &&\mathrm{I}_6 = \mathrm{tr}\left(\mathbf{M}_\mathrm{s}\mathbf{E}_\mathrm{Se}\right), \\ &\mathrm{I}_7 = \mathrm{tr}\left(\mathbf{M}_\mathrm{s}\mathbf{E}_\mathrm{Se}^2\right), \qquad &&\mathrm{I}_8 = \mathrm{tr}\left(\mathbf{M}_\mathrm{n}\mathbf{E}_\mathrm{Se}\right), \qquad &&\mathrm{I}_9 = \mathrm{tr}\left(\mathbf{M}_\mathrm{n}\mathbf{E}_\mathrm{Se}^2\right) \end{aligned} \tag{5.11}$$

along with the material parameters $\mathrm{a_i}$ defined in terms of $\mathrm{b_{ij}}$

$$\begin{aligned} &\mathrm{a}_1 = \mathrm{b_{ff}} - \mathrm{b_{fs}} - \mathrm{b_{fn}} + \mathrm{b_{sn}}, \qquad &&\mathrm{a}_2 = \mathrm{b_{ss}} - \mathrm{b_{fs}} + \mathrm{b_{fn}} + \mathrm{b_{sn}} \\ &\mathrm{a}_3 = \mathrm{b_{nn}} + \mathrm{b_{fs}} - \mathrm{b_{fn}} - \mathrm{b_{sn}}, \qquad &&\mathrm{a}_4 = \mathrm{b_{fn}} + \mathrm{b_{fn}} - \mathrm{b_{sn}} \\ &\mathrm{a}_5 = \mathrm{b_{fn}} - \mathrm{b_{fn}} + \mathrm{b_{sn}}, \qquad &&\mathrm{a}_6 = -\mathrm{b_{fn}} + \mathrm{b_{fn}} + \mathrm{b_{sn}} \end{aligned} \tag{5.12}$$

leading to the definition of Q as

$$\mathrm{Q} = \mathrm{a}_1\mathrm{I}_4^2 + \mathrm{a}_2\mathrm{I}_6^2 + \mathrm{a}_3\mathrm{I}_8^2 + \mathrm{a}_4\mathrm{I}_5 + \mathrm{a}_5\mathrm{I}_7 + \mathrm{a}_6\mathrm{I}_9. \tag{5.13}$$

Thus, the elastic part of the passive stress $\mathbf{S}_\mathrm{Pe}$ is defined as

$$\mathbf{S}_\mathrm{Pe} = \left(\frac{\mathrm{n}^\mathrm{S}}{\mathrm{n}^\mathrm{S}_\mathrm{0S}}\right)^\mathrm{n} \left\{\frac{1}{2}\,\mathrm{A}\exp^\mathrm{Q}\frac{\partial \mathrm{Q}}{\partial \mathbf{E}_\mathrm{Se}} + \ \mathrm{A_{comp}}\left(\mathrm{J_{Se}}\ln\left[\mathrm{J_{Se}}\right] - \mathrm{J_{Se}} + 1\right)\mathbf{C}_\mathrm{Se}^{-1}\right\} \tag{5.14}$$

where use of the relation $\partial\mathbf{C}_\mathrm{Se} = 2\ \partial\mathbf{E}_\mathrm{Se}$ has been made and the strain energy per unit undeformed volume is included in the stress via inclusion of the Jacobian in the *Cauchy* stress via

$$\mathbf{T}^\mathrm{S} = 2\mathrm{J}_\mathrm{S}^{-1}\mathbf{F}_\mathrm{S}\frac{\partial \psi}{\partial \mathbf{C}_\mathrm{S}}\mathbf{F}_\mathrm{S}^\mathrm{T} \tag{5.15}$$

where the pull back of the stress to obtain the second *Piola-Kirchhoff* stress in eq. (4.33) remains valid and is used.

5.1.2 Active mechanics

The myocardium, similar to skeletal muscle tissue, is able to deform without application of external loads, which has been referred to earlier as an active contraction [2], with the clear advantage of being able to supply the body and lungs with blood against a pressure gradient [58]. Contraction of the entire heart does not, however, occur simultaneously but rather gradually in a wave-like manner beginning at the sinoatrial node and ending at the apex [58]. Therefore, individual cardiomyocytes contract at different points in time [95], and thus attempts have been made to couple the mechanics with electrical wave propagation to more accurately describe the contraction process (see e.g. [59, 76]).

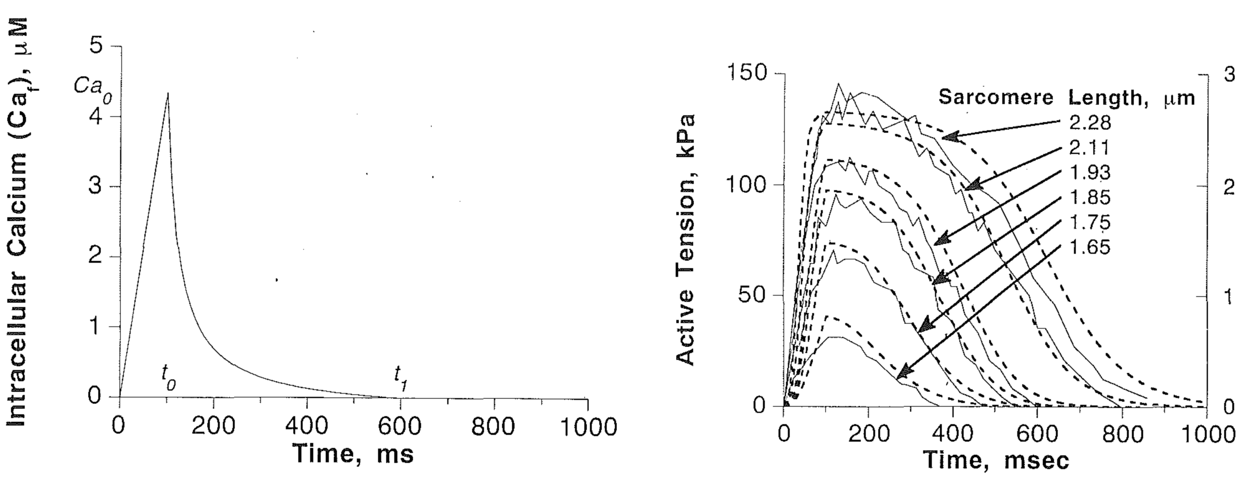

Figure 5.1. (Left) Length dependent free calcium transient that drives contraction. (Right) The effect of sarcomere length on the time course of isometric [2] tension development. [48]

For the purposes of this investigation, however, electro-mechanical coupling is not addressed, thus making the assumption that the active contraction process occurs in a synchronous manner [48]. As such, constitutive modelling has been employed resulting in a constitutive law which describes the active behaviour resulting from changes within the cell such as changes in sarcomere stretch or intracellular calcium concentration, of which the latter is considered to drive contraction (cf. Figure 5.1). Therefore, the active tension $\mathrm{T_A}$ is defined as

$$\mathrm{T_A} = \mathrm{T_{max}} \frac{\mathrm{Ca_0^2}}{\mathrm{Ca_0^2} + \mathrm{ECa_{50}^2}\,(\mathrm{l})} \mathrm{C_t}\,(\mathrm{l},\mathrm{t}) \tag{5.16}$$

where $\mathrm{T_{max}}$ is the maximum tension developed, $\mathrm{Ca_0}$ is the peak intracellular calcium contraction, $\mathrm{ECa_{50}}$ is the calcium contraction at which 50 per cent tension is present, l is the deformed sarcomere length and t is the time. Additionally, the time transient of the sarcomere stretch $\mathrm{C_t}$ is defined as

$$\mathrm{C_t} = \frac{1}{2}\,[1 - \cos\omega\,(\mathrm{l},\mathrm{t})], \quad \text{where} \quad \omega\,(\mathrm{l},\mathrm{t}) = \begin{cases} \pi \dfrac{\mathrm{t}-\mathrm{u}}{\mathrm{t_0}} & \text{for } 0 \leq \mathrm{t} < \mathrm{t_0} \\ \pi \dfrac{\mathrm{t}-\mathrm{u}-\mathrm{t_0}}{\mathrm{t_r}} & \text{for } 0 \leq \mathrm{t_0} < \mathrm{t} < \mathrm{t_0} + \mathrm{t_r} \\ 0 & \text{for } \mathrm{t} \geq \mathrm{t_0} + \mathrm{t_r} \end{cases} \tag{5.17}$$

where $\mathrm{t_0}$ is the time at peak tension, u is the depolarisation time and $\mathrm{t_r}$ is the duration of the relaxation period defined as

$$\mathrm{t_r} = \mathrm{ml} + \mathrm{b} \tag{5.18}$$

where m and b are relaxation constants. The calcium contraction at 50 per cent tension is defined as

---

[2] Muscular action in which tension is developed without contraction of the muscle.

$$\mathrm{ECa}_{50} = \begin{cases} \dfrac{[\mathrm{Ca}_0]_{\max}}{\sqrt{\exp\left[\mathrm{B}\left(\mathrm{l}-\mathrm{l}_0\right)\right]-1}} & \text{for } \mathrm{l} > \mathrm{l}_0 \\ 0 & \text{for } \mathrm{l} \leq \mathrm{l}_0 \end{cases} \tag{5.19}$$

in which B is a constant governing the shape of peak isometric tension-length relation and l_0 is the sarcomere length below which no active tension occurs. The actual sarcomere length l is defined as

$$\mathrm{l} = \mathrm{l}_\mathrm{R}\sqrt{2\,\mathrm{E}_\mathrm{ff}+1} \qquad \text{where} \qquad \mathrm{E}_\mathrm{ff} = \mathrm{tr}\left(\mathbf{M}_\mathrm{f}\mathbf{E}_\mathrm{Se}\right) \tag{5.20}$$

and l_R is the rest sarcomere length. In eq. (5.20), the sarcomere length has been formulated such that $\mathrm{l} = \mathrm{l}\left(\mathbf{E}_\mathrm{Se}\right)$, with the interpretation that during growth new cardiomyocytes are deposited in a stress free manner and thus do not contribute to the active tension. Following Guccione and McCulloch [48] where $\mathbf{S}_\mathrm{Ae} = \mathrm{T}_\mathrm{A}\mathbf{M}_\mathrm{f}$ and making use of eq. (5.7), the active stress is thus defined as

$$\mathbf{S}_\mathrm{A} = \mathbf{F}_\mathrm{Sg}^{-1} \cdot \mathrm{T}_\mathrm{A}\mathbf{M}_\mathrm{f} \cdot \mathbf{F}_\mathrm{Sg}^{-\mathrm{T}}. \tag{5.21}$$

5.2 The cardiac cycle

In order for the heart to supply oxygenated blood to the rest of the body, a specialised process governed by contraction and relaxation of the myocardium occurs known as the cardiac cycle; a continuous sequence of heartbeats. The heartbeat is initiated and controlled via electrical impulses that are generated and conducted by specialised myocardial cells in different regions of the heart [58]. The *sinoatrial node*, located at the base of the *superior vena cava*, is the source of the wave of depolarisation in a healthy heart which is propagated through atrial myocardial cells to the right atrium and then to the left. Initiation of the wave is shown as point P in Figure 5.2, a "Wiggers [3] Diagram" describing the various events of the cardiac cycle.

Thereafter, a delay is experienced in depolarisation as the wave encounters the poorly conducting atrio-ventricular node, located between the atrium and ventricle of the right and left portions of the heart respectively. Following this delay, the wave of depolarisation moves into the left and right ventricles [58]. The wave of depolarisation causes contraction of myocardial tissue and may be viewed as a wave of contraction of cardiac muscle. It is important to note that the entire heart muscle does not contract simultaneously, but rather gradually in a wave-like manner beginning at the base of the heart, and ending at the apex.

Systole (contraction of the heart) and diastole (the period following contraction during which the heart relaxes and again refills with blood) are further divided into four main phases: *ventricular filling, isovolumetric contraction, ejection* and *isovolumetric relaxation*, shown in Figure 5.3.

---

[3] Carl Wiggers (1883-1963): American physiologist and professor famous for his research into the heart and blood pressure, and is most famous for his authoring of the Wiggers Diagram. In 1952 he received the Gold Heart Award from the American Heart Association.

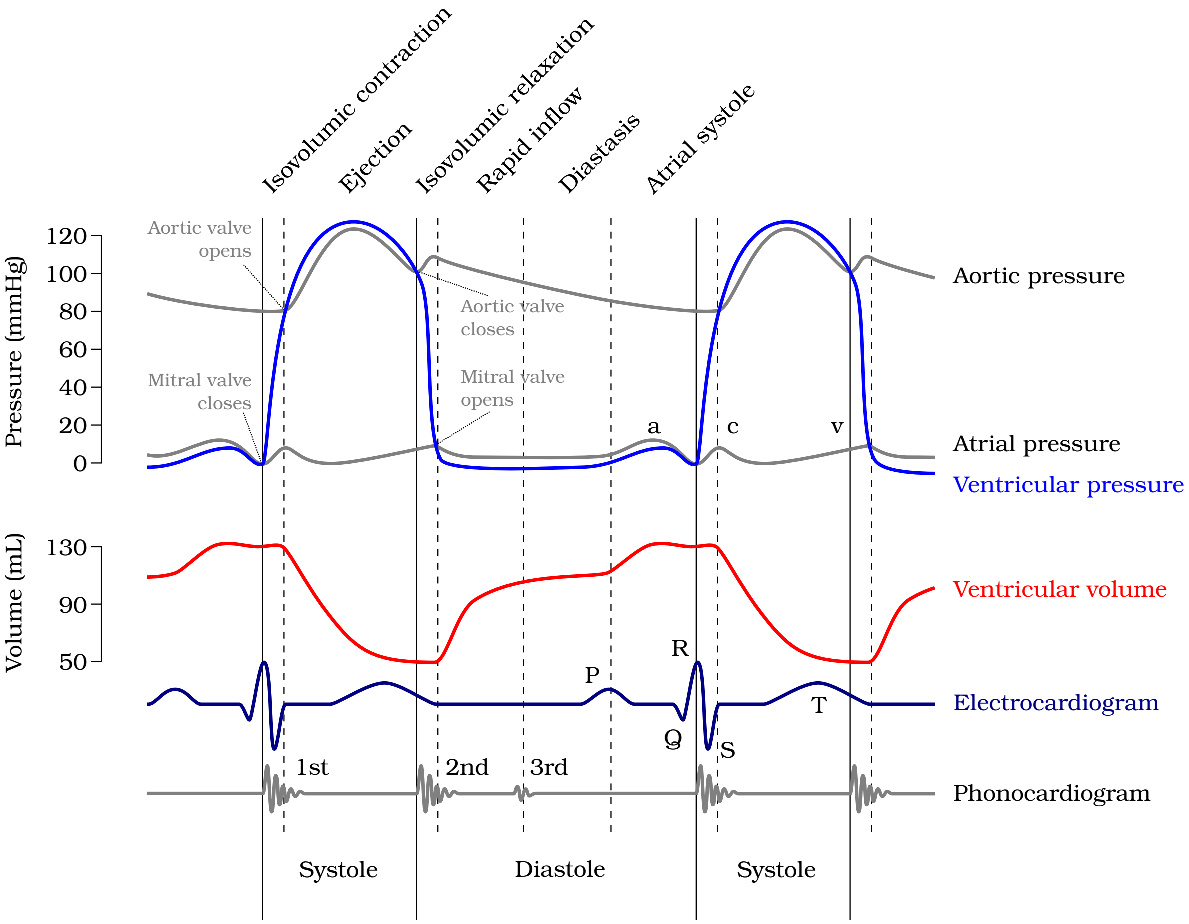

Figure 5.2. Wiggers Diagram showing various events of the cardiac cycle for the left ventricle. In the atrial pressure plot: wave "a" corresponds to atrial contraction, wave "c" corresponds to an increase in pressure from the mitral valve bulging into the atrium after closure, and wave "v" corresponds to passive atrial filling. In the electrocardiogram: wave "P" corresponds to atrial depolarization, waves "QRS" correspond to ventricular depolarization, and wave "T" corresponds to ventricular re-polarization. In the phonocardiogram: The sound labelled 1^{st} contributes to the S1 heart sound and is the reverberation of blood from the sudden closure of the mitral valve and the sound labelled 2^{nd} contributes to the S2 heart sound and is the reverberation of blood from the sudden closure of the aortic valve. [24, modified]

5.2.1 Cardiac function indicators

Various types of work are performed by the heart, of which the external work is of interest in this investigation, which propels blood from the left ventricle into the aorta [58]. In order for such propulsion, the left ventricle is filled with blood over a period known as diastolic filling, to a volume referred to as the end diastolic volume (EDV), which denotes the volume of the ventricle at the onset of ejection. Following ejection, once contraction of the myocardium has ended, a remainder volume is observed referred to as the end systolic volume (ESV). As such, the volume which is ejected by the heart during one beat is defined as the stroke volume (SV):

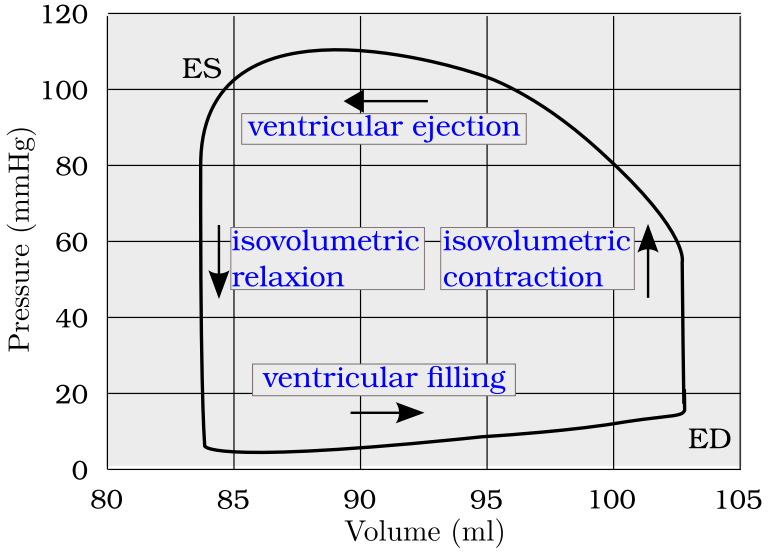

Figure 5.3. Pressure-volume loop generated by a healthy left ventricle [11, reproduced and adapted]. **Isovolumetric contraction**, the first phase of systole begins when ventricular wall stress begins to increase. As a result of the rising ventricular pressure, the mitral valve is closed and blood can no longer enter or leave the ventricle until the pressure within the ventricle reaches that of outside the aorta. During this phase, pressure increases at a constant volume and is noted as an upward deflection. **Ventricular ejection** begins when the aortic valve opens, causing the pressure-volume curve to move towards the left as a result of a reduction in ventricular volume. Systole ends when when the aortic valve once again closes and the ventricular pressure and volume reach the end-systolic pressure-volume relationship (ES). After this point blood can no longer enter or leave the ventricle again and the heart relaxes under isovolumetric conditions. **Ventricular filling** begins when the left ventricular pressure falls below that of the left atrium and the mitral valve opens and blood flows from the left atrium into the left ventricle. Filling continues until the ventricular volume and pressure reach the end-diastolic (ED) pressure-volume relationship. [58]

$$\mathrm{SV} = \mathrm{EDV} - \mathrm{ESV}. \tag{5.22}$$

Additionally, a second cardiac indicator is defined making use of the EDV and ESV, namely the ejection fraction (EF):

$$\mathrm{EF} = \frac{\mathrm{EDV} - \mathrm{ESV}}{\mathrm{EDV}} \tag{5.23}$$

which describes the amount of blood pumped out of the heart at a percentage of the total volume.

5.2.2 Diastolic filling

With regards to the left ventricle, when computationally modelled the cardiac cycle begins with an opening of the mitral valve marking the onset of passive filling. Beginning at a cavity volume V_0, blood flows from the left atrium into the left ventricle, increasing the cavity volume and pressure at a proportional rate. During diastolic filling, no active tension is developed and the mechanical response is purely passive. The gradual increase in pressure results in non-linear deformations, and is solved for using a *Newton-Raphson* iterative scheme increasing the cavity pressure from 0 kPa to 1.5 kPa. As such, the pressure is assumed to be uniform throughout the cavity and is applied via the form of a *Neumann* pressure boundary condition on the endocardium as

$$\mathrm{P}\mathbf{n} = \hat{\mathbf{p}} \text{ on } \partial\mathrm{B}_{\mathbf{P}} \tag{5.24}$$

where $\mathbf{n}_{0\mathrm{S}}$ is the outward orientated normal vector.

5.2.3 Isovolumetric contraction

Following the filling phase, the mitral valve closes and a process whereby the cavity volume remains constant with an increase in pressure, caused by development of active tension within the myocardium. Thus, the required pressure is obtained iteratively with the requirement that $\Delta\mathrm{V} = 0$, via a so-called cavity volume control process, for which the interested reader is directed to Skatulla and Sansour [92] in order to gain a detailed methodological explanation.

5.2.4 Ejection phase

The ejection phase begins following opening of the aorta, where a decrease in cavity volume is experienced, while the active contraction results in a continued increase in pressure for the majority of the ejection phase. However, due to the non-linear resistance of the outflow into the aorta, a three-element *Windkessel* model (cf. [59]) is utilised, whereby the volume decreases over time such that $\Delta\mathrm{V} \neq 0$ and the change is computed solving for the flow rate I_{ao} and the pressure in the aorta P_{ao}. As such, the governing equation for the model is given as

$$(\mathrm{C}\,\mathrm{R}_0)\,\frac{\mathrm{d}\,\mathrm{l}_{\mathrm{ao}}}{\mathrm{dt}} + \left(1 + \frac{\mathrm{R}_0}{\mathrm{R}}\right)\mathrm{l}_{\mathrm{ao}} = \mathrm{C}\frac{\mathrm{d}\,\mathrm{P}_{\mathrm{ao}}}{\mathrm{dt}} + \frac{\mathrm{P}_{\mathrm{ao}}}{\mathrm{R}} \tag{5.25}$$

where C is the arterial compliance, R_0 is the flow resistance and R is the peripheral resistance. The solution of the governing equation is solved incrementally and iteratively as detailed by Skatulla and Sansour [92].

5.2.5 Isovolumetric relaxation

Following contraction of the myocardium, the aortic valve closes as the circulatory pressure is greater than that of the cavity pressure. Once again, a constant cavity volume is retained and the active contraction ceases and the pressure drops as a result.

Chapter 6

Case study of a patient specific rheumatic heart

In the foregoing chapters, the theoretical basis for computational analysis of the rheumatic heart has been developed. This chapter therefore employs the methods outlined to conduct a patient specific study, making use of CMR scans taken over the period of two years provided for this investigation by Cape Universities Body Imaging Centre, Faculty of Health Sciences UCT, Groote Schuur Hospital, Cape Town, South Africa (CUBIC) and specialised segmentation software, Simpleware [1]. As such, the detailed methodology is outlined including the patient's background, 3D model generation, cardiac mechanics specific boundary conditions, material parameter calibration and numerical results obtained.

6.1 Patient background

The patient concerned was first evaluated by a cardiologist at Groote Schuur Hospital in 2014, with indications for CMR assessment as follows:

1. Severe rheumatic mitral stenosis;
2. Atrial fibrillation;
3. Pulmonary hypertension; and
4. Left atrium thrombus on Warfarin

for whom an assessment of left atrial (LA) function was additionally conducted. As a result, the following conclusions were made as provided by CUBIC: "Severe mitral valve (MV) stenosis (MV area 0.7cm^2) with thickened and calcified MV leaflets. Mild-moderate mitral regurgitation. Massively dilated left atrium, with no LA thrombus noted. Dilated main pulmonary artery. Mild tricuspid regurgitation. Normal biventricular size. Mildly impaired left ventricular (LV) systolic function." The patient was diagnosed with rheumatic heart disease, and due to severe mitral valve stenosis, the mitral valve was replaced in 2015. In 2016, CMR scans were repeated for research purposes.

---

[1] www.simpleware.com

6.2 Scan segmentation

In order to conduct computational analysis on the patient specific heart, a finite element mesh is required (cf. Hughes [53]). To generate the mesh and apply the boundary conditions, image processing of the CMR scans is required making use of the so-called segmentation process whereby the images are partitioned into multiple segments based on anatomical location and pixel threshold. To achieve this, the unprocessed CMR scans are imported into a digital viewer capable of visualising a DICOM file format as in common for CMR and MRI scan data. In the case of CMR investigation, a specialised type of image is obtained referred to as a cine MRI/CMR, whereby multiple images are taken over the cardiac cycle allowing one to view changes in the heart's geometry over the period of one beat, and as such providing a moving image of the beat. In this way, specific points of the cardiac cycle are able to be identified, and the shape of the heart at such points is able to be viewed.

During scanning, multiple sets of scans are obtained viewing the short axis (see Figure 6.1), providing image slices at a spacing of 8.3 mm along the long axis which allows for views of the left and right ventricles. In this investigation, RadiAnt Dicom Viewer [2] software was used to visualise short axis cine scans provided by CUBIC in 2014 and 2016 and identify the point of end systole, the point at which the heart is in its relaxed state with the smallest cavity volume before diastolic filling begins.

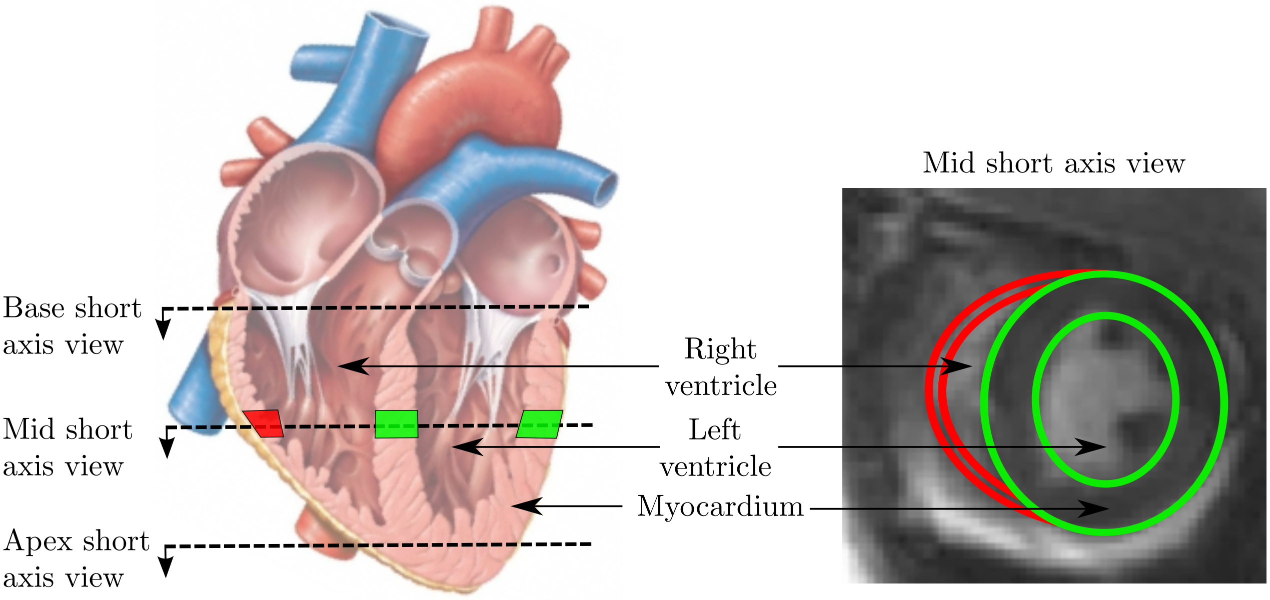

Figure 6.1. CMR image theory and anatomy: showing the location of the base, mid and apical short axis views of the heart (left), and a general CMR image obtained at the mid section outlining the left and right ventricles (right). Heart graphics on left of image sourced from [71, modified].

---

[2] www.radiantviewer.com

Following identification of required scans, DICOM files are imported into a software package with segmentation capabilities, that is functionality to separate pixels in an image to create voxels (the volumetric equivalent to pixels) which represent the 3D volume of the scanned organ. As such, Synopsis' software package Simpleware (along with the ScanIP module) was utilised for this purpose. A total of 12 slices per scan were imported, with three slices per scan illustrated in Figure 6.2.

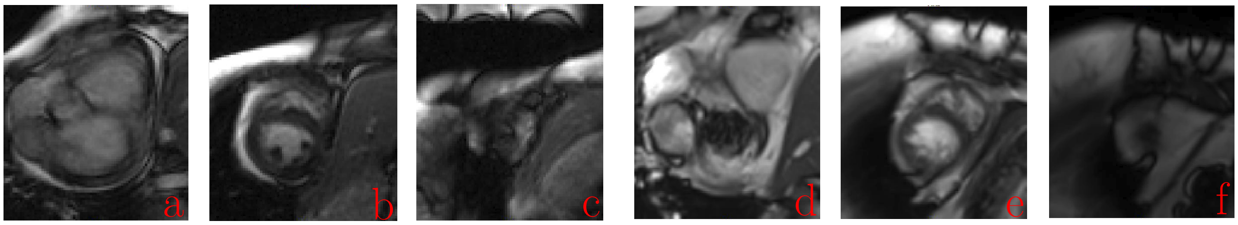

Figure 6.2. 2014 and 2016 CMR raw scans at end systole: showing the 2014 (a - c) and 2016 (d - f) base, mid and apical sections from left to right in the short axis view, as imported into Simpleware before image processing and segmentation. Note: scans have been cropped in order to view thoracic cavity areas of interest.

For this case, during the import process, images were re-sampled in order to increase the pixel density and decrease pixel size for the purpose of increasing accuracy of segmentation, leading to a cubic re-sampling being used, changing pixel spacing from 1.98 mm in the x and y directions, and 10 mm in the z direction, to 0.5 mm. Therefore, the 10 mm space between short axis slices is interpolated and can be more smoothly approximated during volume generation. During segmentation, a so-called mask (layer) is created, which allows for an image layer to be drawn over the imported raw DICOM images, shown as the green areas in Figure 6.3. Due to noise obtained during scanning along with moment of the patient such as breathing and the inherent movement of the heart during scanning, certain areas of interest may be subject to introduction of digital noise; a blurring of pixel values. As such, determination of the endocardium and epicardium limits was conducted using a threshold value separation during which pixels above a certain contrast threshold are ignored by the mask selection process, leaving the myocardium covered by the mask. In order to generate accurate cavity

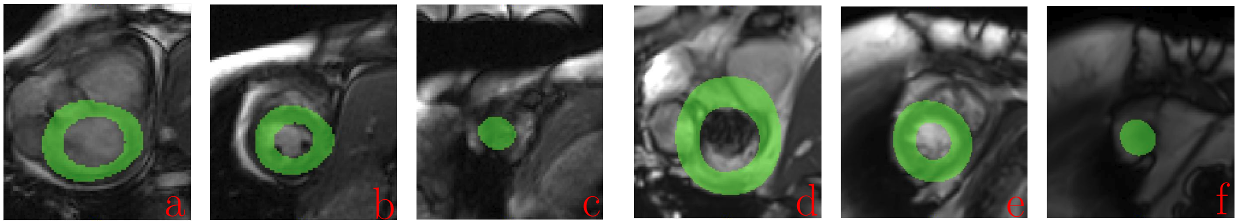

Figure 6.3. 2014 and 2016 CMR segmented scans at end systole: showing the 2014 (a - c) and 2016 (d - f) base, mid and apical sections from left to right in the short axis view. The mask illustrated in green marks the area of the left ventricular myocardium. Note: scan quality of the 2016 data (d - f) is not completely as desired due to a "poor breath hold" during scanning and re-scans to obtain less blurring and thus higher accuracy have been proposed by CUBIC.

volumes, the cavity was segmented using the same process with a lower threshold value thus creating a second mask.

6.3 Geometry and mesh generation

Following creation of the masks, a 3D approximation of the myocardium and cavity is generated and in order to increase surface smoothness primarily in the vertical direction, a recursive Gaussian smoothing algorithm was used. Following the generation of smooth volumes, the correct cavity volume of the myocardial mask was obtained using a 3D editing procedure whereby the volume of the myocardium within the cavity space was removed using the cavity volume mask as a cutting surface.

For the purposes of finite element analysis, a segmented volume is not sufficient as nodes, lines and surfaces are not available in order to generate a mesh of volume elements. Therefore, the segmented volumes may be approximated via a process of fitting a NURBS [3] surface to the volumes. To this end, the +NURBS module contained within the Simpleware software package is a powerful and applicable tool. Making use of the generated volumes during segmentation, NURBS surfaces were fitted to the 2014 and 2016 myocardial volumes, as shown in Figure 6.4.

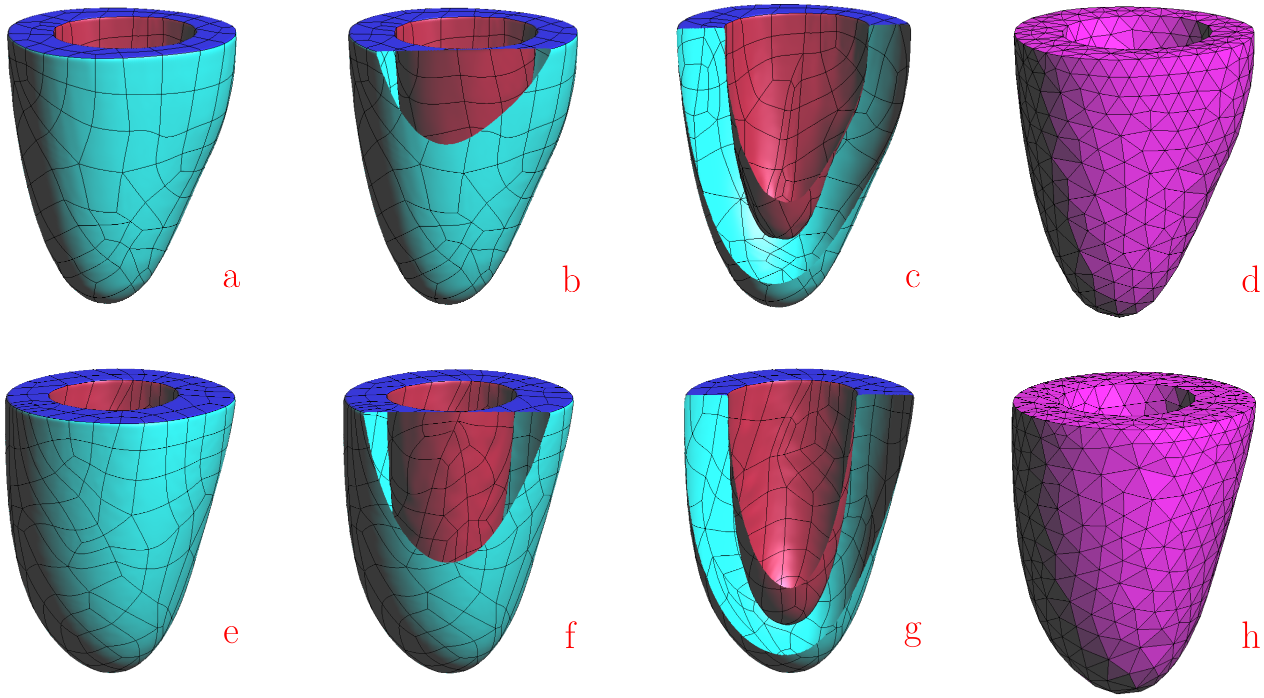

Figure 6.4. 2014 (a - d) and 2016 (e - h) NURBS surfaces and meshes: showing the fitted NURBS surfaces on the two volumes in (a - c, e -g) with 339 patches, 33 900 quadrilaterals and 364 patches, 36 400 quadrilaterals respectively and the corresponding finite element meshes in (d, h), and additionally the base (blue), endocardium (red) and epicardium (turquoise).

---

[3] Non-uniform rational Basis spline (NURBS) is a mathematical computer aided graphical design method which provides geometrical representation of complex free form and standard analytic shapes [81].

For further preprocessing, the NURBS surfaces were imported into the pre- and post-processing software GiD [4] whereby a volume was re-created using the NURBS surfaces. In order to create a realistic mesh of the volume, points and lines associated with the NURBS surface were ignored during mesh generation such that an even distribution of elements was able to be attained, with the exception of lines on the base of the models representing the endocardium and epicardium, which were included to maintain a flat basal surface needed to apply displacement boundary conditions at a later modelling stage. In Figure 6.4 images (d) and (h) which illustrate the generated meshes, the unstructured volume meshes were generated using an RSurf advancing front algorithm using tetrahedral elements, leading to mesh sizes of 2068 and 2318 elements for the 2014 and 2016 scans respectively.

6.4 Boundary conditions and input parameters

In addition to the conventional solid mechanics boundary conditions, in the developed biphasic material model for this investigation, a second *Dirichlet* boundary condition which specifies the pore pressure or alternately a *Neumann* boundary condition which specifies the fluid flux is required. In the case of the left ventricle, *Dirichlet* boundary conditions are applied in accordance with Aguado-Sierra et al. [1] such that the vertical displacement of the base is set to zero and in the isovolumetric stages of the cycle a constant cavity volume is enforced via the method proposed by Skatulla and Sansour [92] setting the change in cavity volume to $\Delta \mathrm{V} = 0$. Conventional *Neumann* boundary conditions are also specified in accordance with Aguado-Sierra et al. [1] such that during diastolic filling, the cavity pressure P increases from 0 kPa to 1.5 kPa, and an elastic line boundary condition is applied to the base-epicardium intersection to prevent excess rotation of the heart, in the form of an elastic reaction force added to the virtual external work $\mathcal{W}_{\text{ext,elastic}} = -\oint_{\mathcal{L}} \kappa_{\text{elast}} \left(\mathbf{c} \cdot \Delta \mathbf{u}_{\mathrm{S}}\right) \mathrm{d}\mathbf{s} \cdot \delta \mathbf{u}_{\mathrm{S}}$ where the unit vector $\mathbf{c} = \mathbf{F}_{\mathrm{S}}\mathbf{c}_0 / |\mathbf{F}_{\mathrm{S}}\mathbf{c}_0|$ is the circumferential tangent on the epicardium in the deformed configuration, $\mathbf{c}_0$ its analog in the undeformed configuration and $\Delta \mathbf{u}_{\mathrm{S}}$ is the displacement vector increment within the current time/loading step, with elastic constant $\kappa_{\text{elast}} = 0.1$ mN/mm. In the case of the fluid flux associated with the pore pressure, in a healthy heart no blood flow from the myocardium into the pericardium is observed and thus a no flow condition is applied to the entire heart surface. Indeed, at the basal section it is likely that an amount of flow to the atrial portion of the myocardium due to fluid redistribution during the cycle is observed in reality. However, in the case that flow is allowed through the base, a Windkessel-type boundary condition is required to describe the resistance to the outflow during the cycle and has not been included in the current approach due to reasons of scope.

Material and cardiac specific input conditions are required as material properties in order to make use of the constitutive laws employed and specialised mechanics of the myocardium. Additionally, rest sarcomere lengths on the endocardium and epicardium $\mathrm{l}_{\mathrm{R}_{\text{epi}}}$ and $\mathrm{l}_{\mathrm{R}_{\text{endo}}}$, respectively, are applied in accordance with Rodriguez et al. [89]. Fibre directions $\mathbf{f}_0$ with specified angles ϕ are applied to the endocardium and epicardium and projected by solving a *Poisson*-scalar-valued problem as presented in Wong and Kuhl [110] where interpolation through the myocardium is accomplished using a moving least squares based approximation

---

[4] `http://www.gidhome.com`

as employed by Skatulla and Sansour [92] has been used in order to obtain a helical spiral of muscle fibres as observed within the tissue.

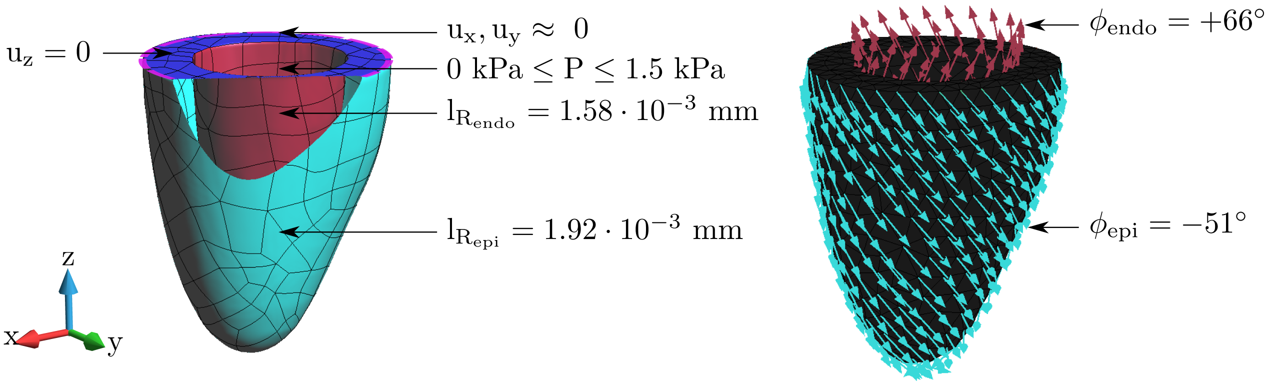

Figure 6.5. Boundary and material conditions for the left ventricle: here shown applied to the 2014 geometry, and for which the same apply to the 2016 geometry.

With the use of porous media theory, additional material parameters are required in order to effectively split the balance equations to make use of the separated material phases. Additionally, the time dependant nature of the problem is influenced by the time step chosen which is thus required to be specified. Therefore, the TPM specific material parameters used are described in Table 6.1.

Table 6.1. Porous media specific material parameters

Parameter	**Value**	**Unit**	**Source**
ρ_{0S}^{SR}	221	kg/m^3	[100]
ρ_{0F}^{FR}	830	kg/m^3	[100]
n^S	0.79	–	[100]
n^L	0.21	–	[100]
K^F	2.0×10^3	mm^4/(N·s)	[105]
δt	0.01	s	[85]
α_{F1}	1	–	[87]

6.5 Calibration and benchmarking

In the following, cardiac mechanics specific material parameters are calibrated, and subsequently used to draw comparisons against the existing SESKA toolbox and available literature.

Table 6.2. Cardiac mechanics parameters: * denotes parameters which have been calibrated in this investigation, and values in parenthesis indicate values used for the 2016 geometry which differ from that of the 2014 parameters. Values for C, R and R_0 have been modified from the original source for initial calibration parameters.

Parameter	Value	Unit	Source
$A^\star$	0.45679, (0.57468)	kPa	[99]
A_{comp}	100	kPa	[99]
a_1	-6.0	-	[99]
a_2	-5.0	-	[99]
a_3	9.0	-	[99]
a_4	12.0	-	[99]
a_5	12.0	-	[99]
a_6	-6.0	-	[99]
$T_{Max}\star$	120	kPa	[49]
C_{a_0}	4.35	μM	[49]
$[C_{a_0}]_{max}$	4.35	μM	[49]
m	1048.9	s/mm	[49]
b	-1.429	ms	[49]
B	2400.0	mm	[49]
l_0	1.58	μm	[49]
$t_0\star$	0.22	s	[49]
$C^\star$	4000 (3600)	mm^3/kPa	[67, modified]
$R^\star$	$1.0 \cdot 10^{-4}$ $(1.5 \cdot 10^{-4})$	$(kPa \cdot s)/mm^3$	[67, modified]
$R_0^\star$	$1.28 \cdot 10^{-5}$ $(1.47 \cdot 10^{-5})$	$(kPa \cdot s)/mm^3$	[67, modified]

6.5.1 Calibration of material parameters

As indicated in Table 6.2, the parameters A, T_{max}, C, R and R_0 were initially chosen, and require calibration on a patient specific basis in order to develop realistic material behaviour and thus obtain realistic pressure volume curves. In the absence of calibration, results obtained within the diastolic filling phase are not admissible as the incorrect volume is obtained for a specific filling pressure influenced by A. In the case of the ejection phase the parameters T_{max}, C, R and R_0 affect the peak cavity pressure and final end-systolic volume, with incorrect parameters leading to volumes which are not consistent with the initial filling volume in the absence of growth, acknowledging that the passive parameter A is most likely not constant when clinically observed.

Consequently, calibration of the diastolic and systolic parameters were dealt with in separate calibration phases in order to ensure that systolic parameters and behaviour remained unaffected by incorrect diastolic parameters. In order to calibrate the stiffness factor A associated with associated diastolic filling and thus the passive behaviour (see Figure 6.6), the initial cavity volume (ESV) and end diastolic cavity volume (EDV) were used as starting and target volumes at pressures of 0 kPa and 1.5 kPa respectively. The ESV was obtained during segmentation of the models and was verified with CMR scan results, with the EDV solely from CMR scan results.

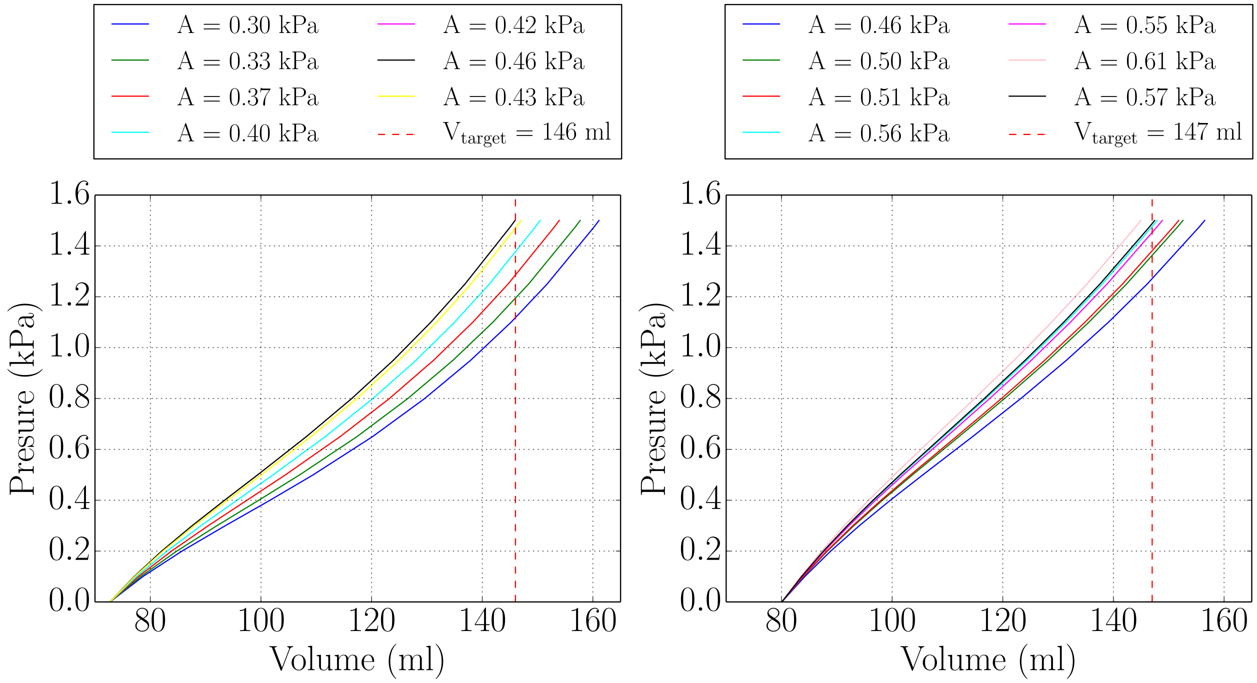

Figure 6.6. Levenberg-Marquardt calibration for the diastolic filling phase: showing a selection of trial A values at the associated pressure volume curves and final volumes for the 2014 (left) and 2016 (right) models. During calibration, a target EDV of 146 ml and 147 ml for the 2014 and 2016 models respectively is illustrated.

In order to calibrate A such that the EDV for the 2014 and 2016 scans was 146 ml and 147 ml respectively, the bounded Levenberg-Marquardt method (BVLM) [111] was used in conjunction with a pressure-controlled loading algorithm linearly incrementing the pressure. The possibility exists to use a cavity volume controlled loading algorithm linearly incrementing the cavity volume during diastolic phase, however at the onset smaller increments are required due to a lower rate of convergence when combined with the coupled problem at hand, resulting in larger computational time expenses.

The method employed is a slightly modified approach based on the work of Guyon and Le Riche [50], with an initial starting point of $A_0 = 0.3$ kPa, and bounding minimum values of $A_{min} = 0.01$ kPa and $A_{max} = 10$ kPa, respectively. An initial value of change $\delta = 0.1$ along with the least square norm of $1.0 \cdot 10^{-10}$ (the value below which the search is complete), a value of the regularisation factor $\lambda = 1$ and a value for the speed at which λ changes $\nu = 2$. At the point at which the EDV for an associated A value is reached, the simulation for the model in question is terminated and restarted at a new trial value until the global minimum has been reached, with result values of interest illustrated in Figure 6.6.

Following calibration of diastolic filling for the 2014 and 2016 models, calibration of the systolic material parameters was conducted, using once again the BLVM. However, in the case of systole and ejection associated with a Windkessel model, multiple parameter calibration is required, namely of the maximum active tension T_{max}, arterial compliance C, peripheral resistance R and flow resistance R_0.

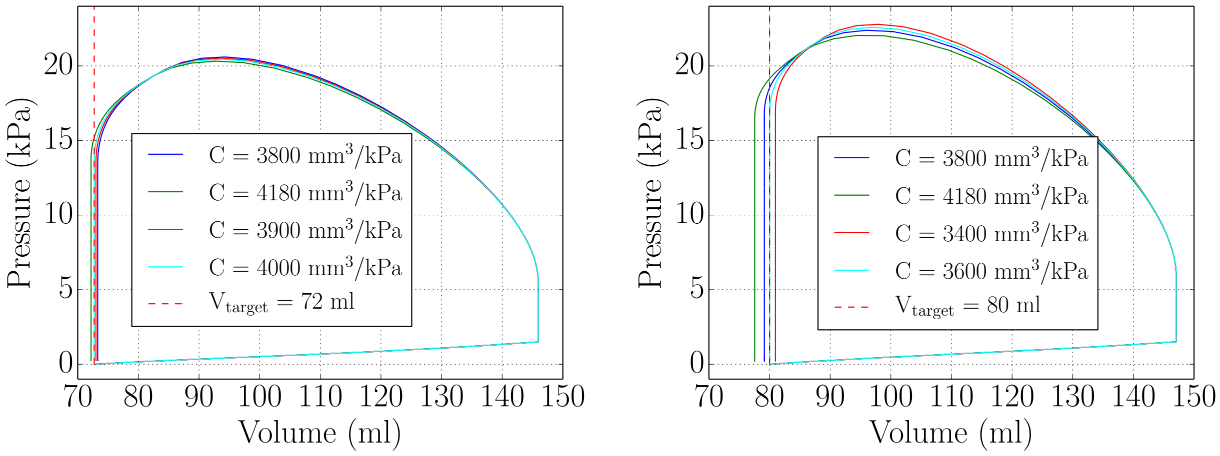

Figure 6.7. Levenberg-Marquardt calibration for the systolic material parameters: showing a selection of trial C values at the associated pressure volume curves and final volumes for the 2014 (left) and 2016 (right) models. During calibration, a target ESV of 72 ml and 80 ml for the 2014 and 2016 models respectively is illustrated.

To this end, C was initially calibrated using a similar approach as for the diastolic filling, with $\delta = 0.3$ along with the least square norm of $1.0 \cdot 10^{-5}$, $\lambda = 1$ and $\nu = 10$ for which results of interest are depicted by Figure 6.7 for the 2014 and 2016 models, in which the end systolic volumes obtained from CMR data were used as the target volumes at the end of each trial value simulation.

Table 6.3. Calibrated cardiac mechanics parameters

Parameter	2014	2016	Unit
A	0.45679	0.57468	kPa
C	4000	3600	$\mathrm{mm}^3/\mathrm{kPa}$
$\mathrm{T}_{\mathrm{max}}$	120	120	kPa
R	$1.0 \cdot 10^{-4}$	$1.5 \cdot 10^{-4}$	$(\mathrm{kPa} \cdot \mathrm{s})/\mathrm{mm}^3$
R_0	$1.28 \cdot 10^{-5}$	$1.47 \cdot 10^{-5}$	$(\mathrm{kPa} \cdot \mathrm{s})/\mathrm{mm}^3$
t_0	0.22	0.22	s

Following calibration of C to an error which remained to be modified such that the least square norm of $1.0 \cdot 10^{-10}$ was obtained $\mathrm{T}_{\mathrm{max}}$, R and R_0 were calibrated, making use of a staggered calibration approach due to the disparity in magnitudes of C and the resistance parameters, which can cause the solution scheme to diverge if handled concurrently due to the value of change δ causing too large an increment for the smaller parameters. During the second step of systolic calibration, an initial value of change $\delta = 1.0 \cdot 10^{-4}$ along with the least square norm of $1.0 \cdot 10^{-10}$, $\lambda = 1$ and $\nu = 10$ were used to obtain the final calibrated parameters for the models used in later patient specific study detailed in Table 6.3.

Discussion: there is a clear change in the material parameters between the 2014 and 2016 data, which is expected as remodelling and growth is expected to cause a change in the stiffness and contractility of the myocardium. During this investigation, the 2014 calibrated parameters are used throughout the growth cycle, such that the kinematic change of a lengthened sarcomere accounts for the change in material properties.

6.5.2 Benchmarking of implemented TPM model

In order to verify the performance of the TPM model, comparisons are made against results obtained from the existing cardiac mechanics toolbox already contained within SESKA for the mechanics aspect of the model, and against the results of Wall et al. [105] for the pore pressure degree of freedom. In the case of the volume fraction degree of freedom connected with growth, calibration and benchmarking against clinical data obtained from CUBIC is contained within the numerical results of the investigation in section 6.6.

In Figure 6.8, simulations making use of the 2014 and 2016 geometry were conducted using the existing toolbox as described by Skatulla and Sansour [92], and subsequently using the TPM model implemented within this investigation, for the case of $\hat{\rho}^{\mathrm{S}}_{\max} = 0$ thus excluding the effects of growth.

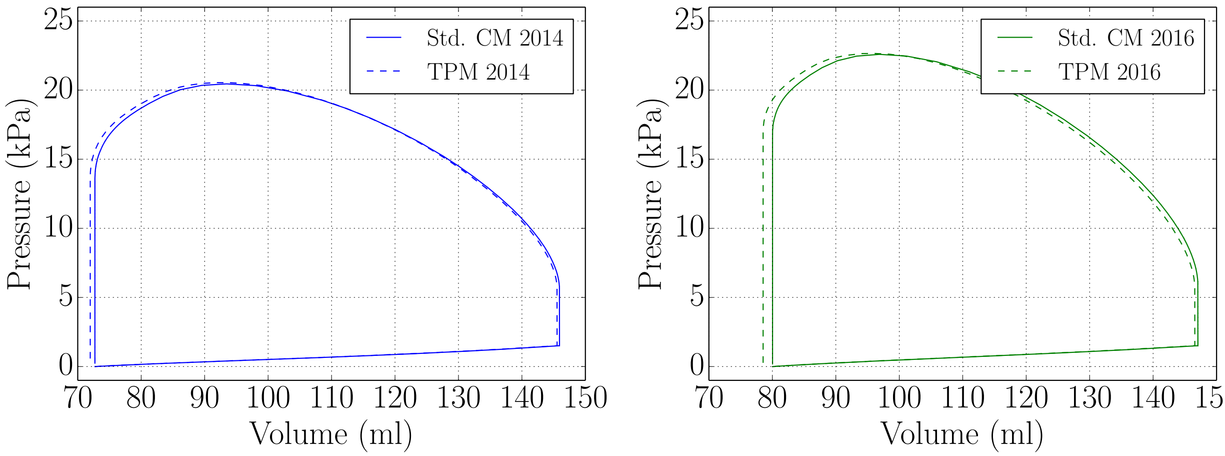

Figure 6.8. Pressure volume curves showing benchmarking against the existing SESKA toolbox using 2014 (left) and 2016 (right) CMR scans; showing the performance of the implemented TPM model, where the standard cardiac mechanics model [92] is abbreviated as “Std. CM”.

In Figure 6.8, identical calibrated material parameters were made use of for the existing and new models, allowing for a constant comparison. As expected, the implemented model does not exactly match the results benchmarked against, due to the inclusion of the effects of the fluid phase of the material and the visco-plastic nature of remodelling due to a change in distribution of pore fluid. The largest contrast in results is in the ESV, where a difference of 0.73 ml and 1.46 ml for the 2014 and 2016 models were realised respectively. The contrast appears to indicate that the TPM model behaves slightly more elastically and in turn develops a larger amount of active tension.

For the pore pressure and fluid flow behaviour, benchmarking against the work of Wall et al. [105] was conducted; who simulated the cardiac perfusion of a subject specific heart using a multi-component *Darcy* porous-media flow model for a pig's LV. While the mechanical aspect of loading was not carried out in their study, and thus deformation was ignored, it serves as a useful indicator of the pore pressures developed within the heart for benchmarking purposes of the performance of the pressure degree of freedom, and additionally provides a realistic input material parameter for the *Darcy* flow K^{F} used within the TPM model of this investigation.

As such, a permeability value of $\mathrm{K}^{\mathrm{F}} = 2.0 \times 10^3\ \mathrm{mm}^4/\ (\mathrm{N} \cdot \mathrm{s})$ was chosen in the range of magnitude of those as suggested by Wall et al. [105] and used to complete a full cycle simulation, during which the pore pressure was monitored as illustrated in Figure 6.9.

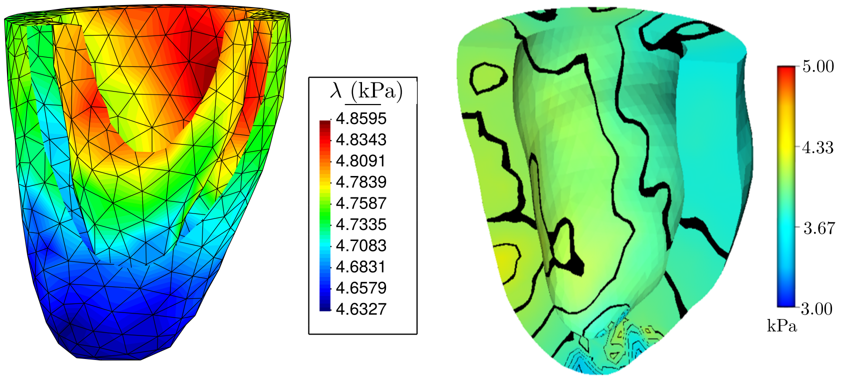

Figure 6.9. Pore pressure benchmarking against the results of Wall et al. [105] (right) for a pig's left ventricle using a three compartment *Darcy* porous media method.

During the simulation, a pressure pattern similar to that as developed by Wall et al. [105] is observed, whereby at the apex of the heart the lowest pressure is experienced, which is possibly due to the apex experiencing the lowest amount of compression and thus lowest amount of fluid flow leaving the region. Moving up to the mid and basal regions, in both cases an increase in pressure is observed with similar magnitudes of $\lambda \approx 4.7$ kPa and $\lambda \approx 4.3$ kPa for the TPM and Wall et al. [105] models at the mid section respectively. At the base, the maximum pressure is experienced at a value of $\lambda \approx 4.9$ kPa. Additionally, it is notable that in both cases, a concentration of pressure is observed around the mid section of the myocardium. While the cause is not specifically clear, the possibility exists that the geometry of the myocardium at this point is the cause. The reason for such a possibility is that while a more specific and accurate vascular structure was included by Wall et al. [105], such a structure is not included within this investigation which exhibits a similar behaviour. With the exclusion of deformation by Wall et al. [105], the possibility of a mechanical cause is thus ruled out.

Finally, in order to validate the behaviour of the developed model, the mechanical behaviour of the myocardium was observed throughout the cardiac cycle, as illustrated in Figure 6.10. Following diastolic filling, a chamber dilation is observed, primarily at the base and decreasing towards the apex. As the pre-load (end diastolic pressure) is increased, further dilation of the apical regions of the chamber is observed, showing that the basal region is first to dilate during filling and appears less mechanically stiff. Following isovolumetric contraction, a twist a

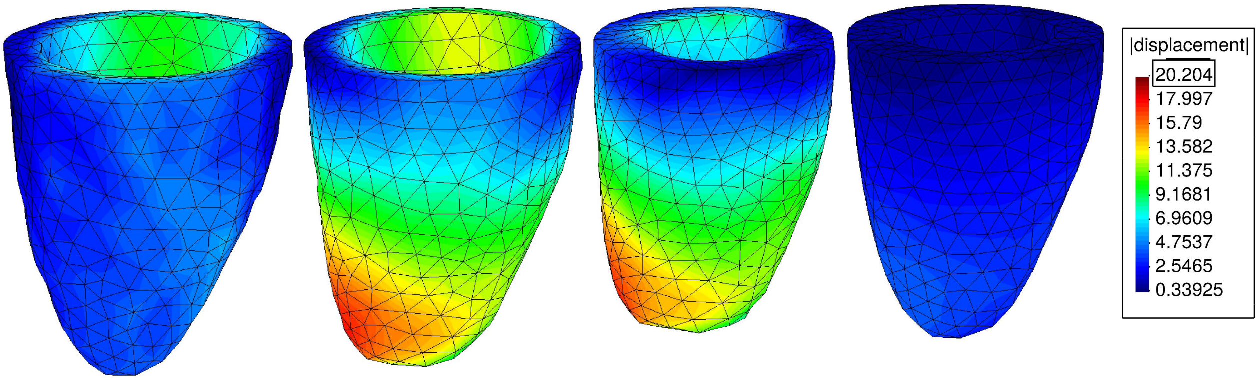

Figure 6.10. Displacement contour plot [mm] of the cardiac cycle; showing the four stages of the cardiac cycle from left to right - end diastole, end IVC, end ejection phase and end IVR, used to visualise the four stages of the cardiac cycle in terms of mechanical deformation.

shortening of the myocardium is observed, which is increased further at the end of the ejection, where a substantial twist and shortening is observed at the ESV. Following isovolumetric relaxation, most deformation has returned to that of the original structure. However, an amount of residual deformation is realised as the structure has remodelled slightly and natural optimisation of displacement and pore pressure distributions have developed.

Such behaviour is expected, as the original configuration of the geometric model is inherently in an unloaded state, which is not entirely consistent with what is experienced by the heart in-vivo, which remains in a state of loading throughout the cardiac cycle; this state of stress and strain is also the case for biological tissue growth in the absence of disease. For the purposes of this investigation, the original state of the heart has been treated as unloaded, which however may be addressed via a process similar to that of Ricken et al. [87] whereby simulation steps are utilised to obtain an optimised structural state before further analysis is conducted. This method, however, has not been used within this investigation due to computational time demands.

6.6 Numerical results

From the outset, the aims of this investigation have been to implement a computational model capable of providing initial insights into the pathophysiology of RHD, and additionally to provide a computational base model on which advances may be made to study the disease in further detail. Therefore, simulations have been conducted on the two sets of scans without mass been supplied during the simulation, allowing the behaviour of the patient's heart to be analysed at two separate points in time, namely in 2014 and 2016. Additionally, a simulation was conducted on the initial state of the heart in 2014, with the inclusion of mass supply to imitate the changes in the patient's heart as predicted numerically and thus with a mass supply $\hat{\rho}^{S} \neq 0$, which was calibrated such that the behaviour of the heart was similar to that of the 2016 behaviour following the simulation. The approach and results thereof are detailed in the remainder of this chapter.

6.6.1 Behavioural changes over a two year period excluding mass supply

The TPM model, coupled with the active myocardial contraction and the haemodynamics of the circulatory system, was used to conduct simulations on the 2014 and 2016 models making use of cardiac mechanics specific material parameters as detailed in Table 6.2. In this case, no mass supply is included allowing the state of the patient's heart in each scan to be modelled excluding the effects of added growth due to the growth law implemented within this study. Both geometric models were simulated through one full cycle, over which the growth during a two year period is apparent. Associated with the behaviour of the patient's heart over the two year period, the cardiac indicators obtained from clinical results show a deterioration in condition, as seen in Table 6.4 in which the stroke volume has decreased by 7 ml and ejection fraction by 5 %.

Table 6.4. Cardiac indicator results as observed.

Parameter	2014	2016	Unit
EDV	146 [22]	147 [22]	ml
ESV	72 [22]	80 [22]	ml
SV	74	67	ml
EF	51	46	%

This worsening of the patient's condition is illustrated numerically via the two simulations: as shown in Fig. 6.11 (left), the end systolic and end diastolic volumes increased from 72 ml and 80 ml to 146 ml and 147 ml for the 2014 and 2016 models, respectively. Following diastolic filling, the isovolumetric stage is observed to a pressure of 5.5 kPa in both models during which volumes and behaviour is as expected. In the ejection phase, while the volume decreases and pressure further increases to 20 kPa and 23 kPa, it is clear that a larger pressure is developed within the 2016 cavity with an associated end systolic volume (ESV) of 80 ml as opposed to that of the 2014 cavity of 72 ml. As such, in order to retain the end-systolic pressure relationship of the patient's heart, assuming that the mechanical stiffness and contractility were unaffected by the growth and remodelling, the maximum pressure during ejection has increased over the two year period. The larger ESV of the 2016 model may indicate growth of the patient's left ventricle in order to accommodate a volume overload due to the regurgitant mitral valve which appears to have not been fully recovered.

With the use of the porous media approach, the behaviour of the blood and other fluids contained within the myocardial tissue (i.e. not within the atrial and ventricular cavities) is able to be modelled. Due to inclusion of the dynamic effects of the fluid during the cardiac cycle, and additionally a further non-homogeneous material behaviour due to varying degrees of fluid volume throughout the location of the heart, the use of this theory thus provides a distinct modelling advantage towards accurately describing the mechanical behaviour of the beating heart. The amount of fluid present within the pore spaces of the myocardium, and its movement between such pores, is related directly to the pressure of the fluid within the pores, and is illustrated in Fig. 6.11 (right) for both simulations. Initially, during diastolic filling, a negative pressure is observed indicating that fluid is flowing towards the mid and away

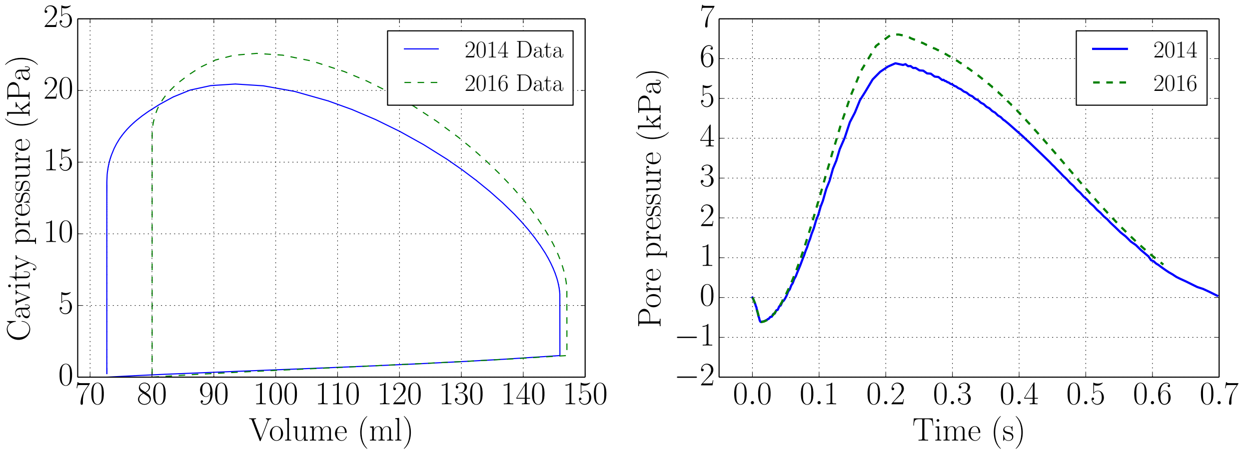

Figure 6.11. Full cycle pressure volume curves of the 2014 and 2016 models; showing an increase in end systolic volume, slight increase (1 ml) in end diastolic volume and an increase in cavity pressure over the two year period (left) and pore pressure evolution over time at the mid section of the myocardium, shown as point A in Figure 6.12 (right).

from the base of the ventricle as the heart expands. During contraction, positive pressures are developed indicating a flow of fluid away from the mid section and a decrease in the amount of fluid, and as such it is clear that the fluid volume distribution is continually optimised during the simulation. Significantly, the peak values of pore pressure of 6 kPa and 6.5 kPa correlate to the results obtained by Wall et al. [105], in which pore pressures of 3.5 kPa to 7 kPa were induced in different compartments of the model.

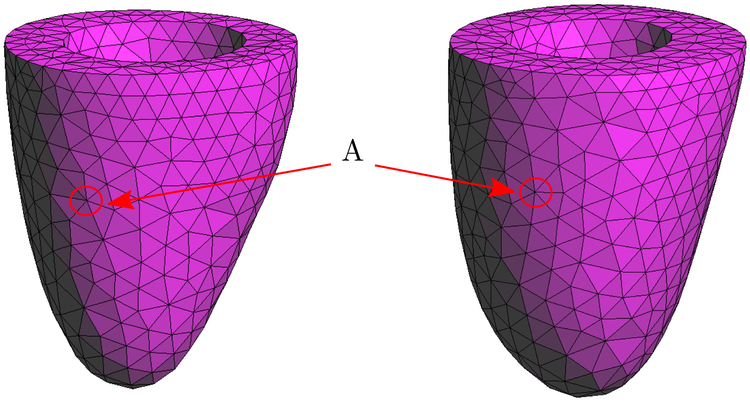

Figure 6.12. Point of numerical results on meshed geometry at the mid section of the heart; shown as point A.

As the pressure and volume behaviour of the heart are linked to the muscular behaviour and properties, the stress and strain of the myocardial fibres are thus addressed in order to elucidate the changes in the observed cardiac performance, and subsequently the changes in the fibre length and tension. In Fig. 6.13, it is shown that an increase in cavity pressure as a result of growth is associated with an increased fibre stress and strain, thus indicating that growth of the patient's heart has in fact placed more stress and strain on the myocardium, with the predicted strain being verified to a reasonable extent via comparison to results obtained from a separate patient, and by the findings of Donker et al. [31] who found that fibre stresses and strains in a dog's heart increase with ventricular volume overload. Noteworthy, fibre stress begins increasing in early diastole until the relaxation phase, whereas fibre strain is affected in a more accentuated manner at the onset of active contraction. The initial peak of fibre strain during diastole is, however, unable to be verified due to the clinical circumferential data beginning at t = 0.044 seconds.

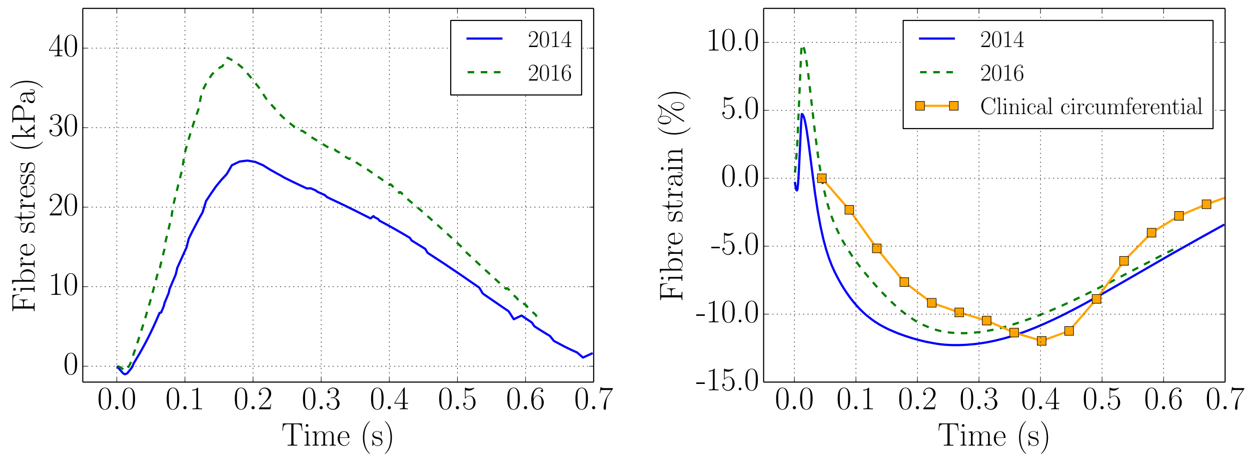

Figure 6.13. Fibre stress (left) and fibre strain (right) evolution over time at the mid section (point A of Figure 6.12) of the myocardium. Note: the curve labelled "Clinical circumferential" was obtained from tagged CMR scans of a separate patient for the mid section (inferior) of the epicardium in the circumferential direction (data supplied by CUBIC) corresponding approximately to point A of Figure 6.12, and is thus not intended for quantitative comparison but rather to illustrate a reasonable degree of qualitative agreement of strains produced numerically at the mid section, which is useful in the absence of further literature or clinical data at present.

As the sarcomere length is linked to the fibre strain, an increase between the 2014 and 2016 data is expected, which is confirmed by Fig. 6.14 (left); during diastolic filling the 2014 sarcomere length peaks at $2 \cdot 10^{-6}$ m, while in 2016 a peak of $2.1 \cdot 10^{-6}$ m is apparent. The onset of active contraction is apparent at the change in rate of change of length, where a decrease begins to occur until the relaxation phase is entered, during which the length begins to return to that of the resting state. Linked with sarcomere length is the active tension response, shown in Fig. 6.14 (right), where peaks of 18.6 kPa and 25.1 kPa are reached respectively, in agreement with Guccione and McCulloch [48] for a sarcomere length of 1.65 μm. In both cases, it is noted that the sarcomere length and active tension response have increased over the period from 2014 to 2016.

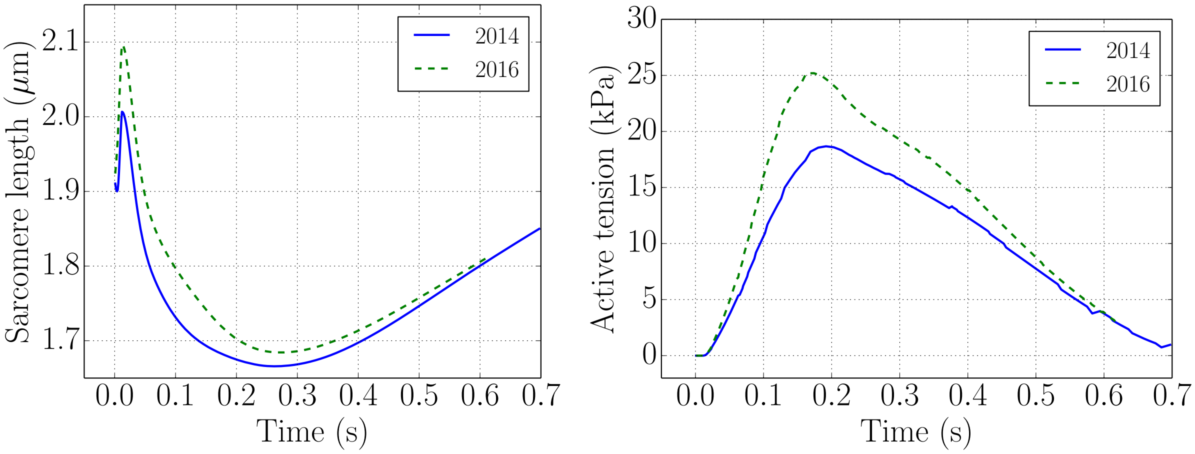

Figure 6.14. Sarcomere length (left) and active tension (right) evolution over time at the mid section of the myocardium, at point A of Figure 6.12 .

6.6.2 Modelled behavioural changes including mass supply

Following simulations on both geometries for the case of no supplied mass, simulations were conducted inclusive of the effects of mass supply, that is $\hat{\rho}^{\mathrm{S}}_{\mathrm{max}} \neq 0$, allowing for the stretch driven change in kinematics to be activated with corresponding parameters detailed in Table 6.5, adding the final aspect of this investigation; an ability of the model to predict the changes to the heart's behaviour during the two year period, and not solely at two discrete time points of the scans. For this purpose, the relevance of two sets of scans taken over a period of two years in which adverse growth and structural changes have occurred becomes apparent; when modelling the growth behaviour, the 2014 scans may be used as the initial starting point for analysis, and the 2016 scans from the same patient serving as the target point following growth.

Table 6.5. Growth specific material parameters for patient specific analysis.

Parameter	**Value**	**Unit**	**Source**
$\hat{\rho}^{\mathrm{S}}_{\mathrm{max}}$	0.5×10^{-7}	tonne/(s·mm^3)	-
ϵ^{c}	1.001	-	[42]
ϵ^{max}	1.5	-	[42]
γ	1	-	[42]
τ	4	–	[42]

As such, the initial geometry and material parameters used for the following simulation are that of the 2014 scans with the variable during the simulation being the amount of stretch-driven growth impacting the behaviour of the heart. Beginning at the 2014 geometry, growth occurs during the simulation in an attempt to match the final behaviour of the 2016 state of the patient's heart. By this process, changes in the behaviour of the initial model may be observed and analysed as a first step to draw conclusions with respect to growth on the behaviour of the rheumatic heart. The simulation was modelled over a period of one heart beat, which may be used to model the growth over a two year time period with the growth being assessed over a different time scale to that of the deformation.

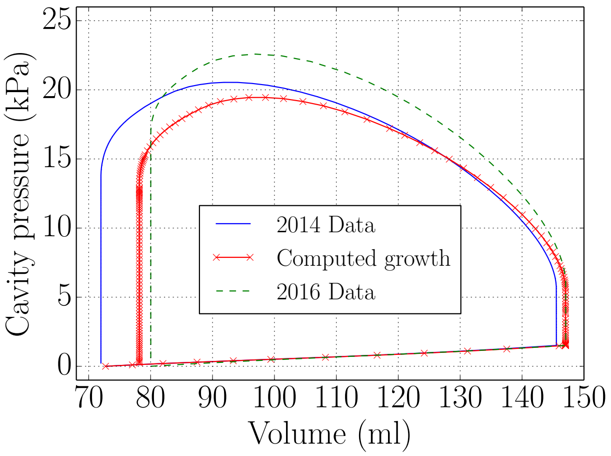

Figure 6.15. 2014 and 2016 pressure volume curves, compared against the computed growth pressure volume curve run on the 2014 geometry; where for the growth model a decreased stroke volume of 4.75 ml over two years was computed. Along with a decreased SV, dilation of the ventricle is observed where the dilation at end systole is greater than that at end diastole, typical of the case of dilated cardiomyopathy. A decrease in ventricular pressure is also observed.

In Figure 6.15, results of the three simulations have been presented in the form of pressure-volume curves, where the "2014 and 2016 Data" curves illustrate the final results in the absence of growth, that is the numerically simulated behaviour of the patient's heart at two points in time. The "Computed growth" curve illustrates the altered behaviour of the 2014 Data in the presence of growth. Here, for the "Computed growth" curve, it is observed that the initial cavity volume is 72 ml, with an associated EDV of 147 ml, where an increase of 1 ml when compared to the original volume is observed, serving as the first appearance of growth during the simulation in agreement with the clinical data obtained from CUBIC. Due to an overall increase in sarcomere length, the cavity volume is increased for the same end diastolic pressure of 1.5 kPa.

During the IVC phase, the *Dirichlet* boundary condition applied such that $\Delta \mathrm{V} = 0$ has taken priority during which the growth has been neglected and set to $\hat{\rho}^{\mathrm{S}}_{\mathrm{max}} = 0$ due to numerical difficulties during this stage of the cycle. Due to cavity volume being held constant during IVC, and an increase in mass along the cardiomyoctye axis causing elongation and thus an increase in cavity volume, convergence of the equation system is clearly affected, which was solved by restricting the increase in cavity volume due to growth to null.

During the ejection phase, growth is once again activated and ejection occurs until an ESV of 78.2 ml is obtained, compared against the 2016 ESV of 80 ml. At the onset of ejection, the cavity pressure lies between the original 2014 and 2016 pressures. However, at 128 ml the pressure drops below that of the original 2014 pressure, in contrast to the computed increase in pressure for 2016 which remains along the end systolic pressure volume relationship line.

In the case of dilated cardiomyopathy (DCM), a decrease in pressure is to be expected as the end-systolic pressure-volume relationship (ESPVR) shifts to the right with a decreased slope (see [51]), and is observed in this investigation. The cause of this discrepancy in results is likely due to surgical intervention in 2015, which is not able to be modelled in this investigation as the mitral valve has not been considered.

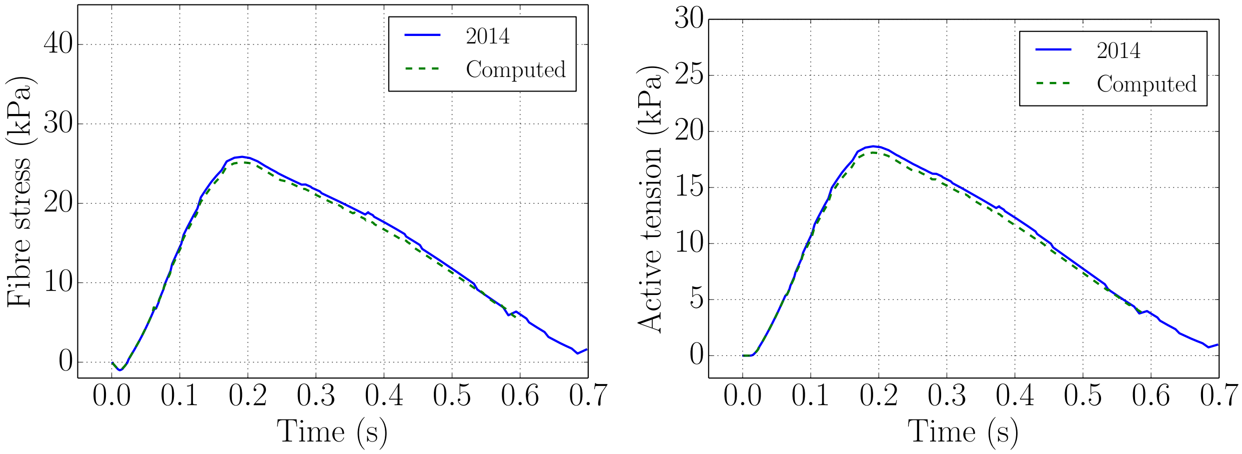

Figure 6.16. Fibre stress (left) and active tension (right) evolution over time at the mid section of the myocardium, at point A of Figure 6.12, showing the evolution in the presence of computed growth. Here, correlating to a decreased pressure, a decreased fibre stress and active tension is observed.

However, in the pursuit of further data regarding RHD and DCM, the active tension and fibre stress curves for 2014 and the computed growth, correlating to the pressure volume curve in Figure 6.15, are illustrated in Figure 6.16. Here, a decrease in fibre stress and active tension have been observed, leading to the possibility that in the case of purely dilated cardiomyopathy without surgical intervention, as the muscles stretch and loosen, the fibre stress and active tension are reduced, along with a slightly decreased cavity pressure.

Table 6.6. Cardiac indicator results as computed via inclusion of mass supply.

Parameter	**2014**	**2016**	**Simulated growth**	**Unit**
EDV	146 [22]	147 [22]	147 (0)	ml
ESV	72 [22]	80 [22]	78.2 (2.3)	ml
SV	74	67	68.8 (2.6)	ml
EF	51	46	46.8 (1.7)	%

Note: values in parenthesis indicate the percentage error from target (2016) results.

Based on the pressure volume curves shown in Figure 6.15 and cardiac indicator results in Table 6.6, it is observed that the implemented growth model has followed clinical results to a reasonable degree of volumetric error. With regards to the computed growth, the EDV matches that of 2016, and an increase of ESV from 72 ml to 78.2 ml of 6.2 ml has lead to a decreased volume, typical of DCM and in accordance with the 2016 results of 8 ml.

Additionally, a decrease in EF from 51% to 46.8% is apparent, similar to the 2016 EF of 46% indicative of a worsening of the heart's condition and efficiency.

Strongly connected with the growth curve in Figure 6.15 is the change in volume fraction due to mass supply, illustrated in Figure 6.17, which is the driving factor underlying the volume change. On the contour plot of added volume fraction $\mathrm{n}_{\mathrm{g}}^{\mathrm{S}}$, the largest deposition of mass is located in the basal to mid regions, where the maximum amount of stretch is experienced. Additionally, due to compression of the myocardium in these areas as a result of the elastic boundary condition, most stretch is experienced on the endocardial surface thus yielding the largest amount of mass supplied. The maximum value $\mathrm{n}_{\mathrm{g}}^{\mathrm{S}} = 0.071$ denotes an increase in solid volume over the two year period by 7.1%.

In the evolution of mass supplied at point B, the shape of the mass supplied strongly correlates with the specified mass supply function and shows an initially steep growth which tapers to a constant supply in the ejection phase where the rate at which mass is supplied decreases. At point A, an increased solid density of $\hat{\rho}^{\mathrm{S}}_{\mathrm{max}} \approx 6.75 \cdot 10^{-6}$ g/mm^3 has occurred and at the point $\hat{\rho}^{\mathrm{S}}_{\mathrm{max}} \approx 1.0 \cdot 10^{-6}$ g/mm^3, the horizontal line indicates that no growth has taken place over the time period, due to growth effects during the IVC being neglected.

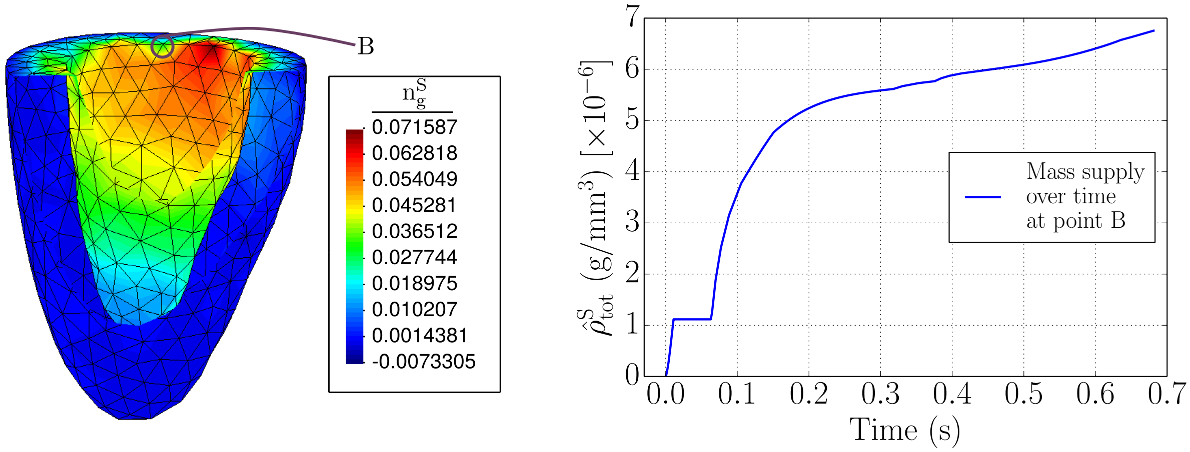

Figure 6.17. Growth volume fraction contour plot (left) and evolution of total mass exchanged from the fluid to the solid phase at point B (right).

Chapter 7

Conclusions and future work

In the following, conclusions with regards to the implemented TPM model, and subsequently with regards to the patient specific investigation are made. After which, the future work and further applications of the model are discussed.

7.1 Biphasic growth model

During this investigation, a biphasic material model within the framework of the theory of porous media (TPM) has been implemented, with specific applications to cardiac analysis, remodelling and the inclusion of growth modelling via a stretch-driven mass supply function. For this purpose, two additional degrees of freedom were used to augment the classical mechanics displacement degrees of freedom allowing a coupling of the displacement field, interstitial pressure/flow and the volume fractions. Furthermore, the TPM model has been coupled with the highly specialised cardiac mechanics toolbox of SESKA which leads to the use of TPM in conjunction with the active mechanics of the myocardium and allowing the orthotropic nature of the myocardium to be included. As such, the addition of porous media theory and additional cardiac mechanics analysis capability has been added into the SESKA toolbox achieving a novel coupling of specialised cardiac active contraction, circulatory haemodynamics and TPM. Based on the results presented in section 4.5, it is concluded that the additional porous media degrees of freedom have been implemented successfully and function as expected, which allowed for further analysis of the myocardium using the model.

In terms of the mass supply between the solid and fluid phases, it is desirable to include a third fluid phase containing the nutrients required for growth. Such an addition is likely to lead to a more realistic approximation of the growth behaviour, as the fraction of the blood is not slightly decreased during growth which has the possibility to influence the mechanics and interstitial pressures/flow. However, in the absence of data against which to compare this approach and the scope of this investigation, a conclusion cannot be drawn with respect to the sufficiency of the use of two rather than three degrees of freedom. However, as volumetric results in Chapter 6 were closely matched to that of clinical data, the possibility that use of the biphasic description remains sufficient at this point.

Extending upon the work of Werner et al. [107], the developed model allowed extension of the partially developed cardiac analysis model within the framework of TPM.

7.2 Case study

At the onset, realistic patient left ventricular (LV) 3D models were created using scans from 2014 and 2016 of one patient diagnosed with rheumatic heart disease (RHD), over which significant growth and remodelling of the LV had occurred provided by CUBIC. In terms of segmentation and 3D model creation, compared against the provided clinical data of cardiac volumes, it was concluded that the degree of accuracy of the models was reasonable allowing further study to be conducted.

Following model creation, certain cardiac mechanics and TPM material parameters were calibrated in section 6.5 and the behaviour of the model was benchmarked against the existing SESKA toolbox and Wall et al. [105]. Cardiac parameters were calibrated making use of the Levenberg-Marquadt method in order to achieve the required end diastolic and end systolic volumes in agreement with clinically provided volumetric data from CUBIC. Pressure-volume behaviour of the implemented model closely matched that of the existing toolbox, with a small degree of difference as a result of the behaviour of the interstitial fluid being taken into account, adding a dynamic response. The pore pressure degree of freedom was benchmarked and while values were not entirely numerically comparable due to a pig heart being used by Wall et al. [105], patterns and trends of the pressure distribution were in agreement. Based on the calibrated and benchmarked results, it was concluded that further patient specific case study was able to be conducted.

In the case study, three sets of simulations were conducted; two with the exclusion of mass supply on the 2014 and 2016 models in order to access the cardiac behaviour of the patient's heart and the change in behaviour over a period of two years of growth and remodelling. The simulations showed an increase in cavity volume with a decreased stroke volume and ejection fraction, indicative of dilated cardiomyopathy as a result of mitral valve regurgitation caused by RHD. An increase in pore pressure, fibre stress, fibre strain, sarcomere length and active tension as a result of the disease was observed, however, such increases are not common in the case of DCM and are possibly due to surgical intervention in 2015 altering the valve behaviour. Additionally, fibre strain results were comparable to those of clinically provided fibre strain data.

A third simulation was conducted, which began at the 2014 model state, with the inclusion of mass supply such that the final state of the heart closely matched that of the 2016 state following growth and remodelling. From this, it was concluded that the growth model had described the change in state of the heart over the two year period, however, a more detailed investigation into the cause of change is required in order to elucidate the chronology of the disease.

7.3 Future work and applications

While biological modelling is challenging in the most simple of cases, the human heart is an extraordinarily intricate case. Therefore, while extensive theoretical approaches have been applied in this work, a multitude of possible future additions remain available in order to more accurately describe the growth of cardiac tissue. Therefore, within the context of cardiac growth the following future additions to the current approach are proposed, which is by no means a complete list.

Firstly, approaches have been employed within the context of TPM whereby a third phase in which the nutrients of the blood are contained (see e.g. [86]). Such an inclusion leads to the advantage that the amount of fluid contained within the material is not altered as only the nutrient phase is degraded during the mass exchange process. However, in the case of continuous growth, a source term is required which presents an implementational and theoretical challenge to the currently used model.

The mass supply function presented within this investigation is based purely on mechanical effects on the macro-scale. However, cardiac growth and remodelling is caused by a multitude of factors (chemical, biological, hormonal and mechanical to name a few) which in actuality occur at a cellular and lower level (see for example [73]). Furthermore, the possibility of treatment using pharmaceutical compounds to alter changes on the cellular level exists. Therefore, an implementation of a more sophisticated micro-structural approach such as the FE^2 method coupled with TPM (see Bartel et al. [12, 13]) may be employed in the future.

As the model has been set up in order to make use of the existing SESKA toolbox with a multitude of mass supply functions, implementation of stress-driven function describing concentric growth (such as that of an athletes heart) to further growth knowledge in the computational cardiac mechanics field exists as an opportunity to further add to the toolbox.

In terms of 3D model creation, the creation of bi-ventricular geometries is the next step towards modelling of the entire heart. Making use of the existing scans, segmentation of the right ventricle is possible, which has the advantage of adding a more accurate description of the ventricular behaviour as the mechanics of the left ventricle is in actuality influenced by the right and vice versa.

With the formulation of the current approach, and that of the references used such as Göktepe et al. [42], Werner et al. [107], it is clear that over the period of one heart beat, which is applied a time scale of larger than one beat in reality, a larger change in ESV compared to that of the EDV is expected, as growth is added at each time step. This leads to the situation whereby more stretch has occurred near the end of the cycle as opposed to the relatively early stage at which EDV occurs. Therefore, to gain further results and conclusions, a pre-run during which growth occurs may be conducted, following which no growth is added and the behaviour of the newly grown heart may be studied, as opposed to the “in-beat” behaviour of this investigation.

Finally, in order to draw further conclusions, future work may include a larger set of scans from different patients adding a higher degree of statistical significance to the results. Additionally, due to a slightly poor scan quality in the 2016 data, the patient may be rescanned in order to more accurately describe the heart geometry.

Appendix A

Linearisation of the weak forms

The balance equations are linearised in the following manner:

$$\varDelta \mathrm{G} = \frac{\partial \mathrm{G}}{\partial \mathbf{u}_{\mathrm{S}}}\Delta \mathbf{u} + \frac{\partial \mathrm{G}}{\partial \lambda}\Delta\lambda + \frac{\partial \mathrm{G}}{\partial \mathrm{n}^{\mathrm{S}}}\Delta \mathrm{n}^{\mathrm{S}}. \tag{A.1}$$

A.1 Balance of momentum - mixture

We have the weak form for the balance of momentum as:

$$\mathrm{G}_{\mathrm{mom}} = \int_{\mathrm{B}_{0\mathrm{S}}} \frac{1}{2}\,\mathrm{S}_{\mathrm{ij}}\delta \mathrm{C}_{\mathrm{ij}}\mathrm{dV} - \int_{\mathrm{B}_{0\mathrm{S}}} \rho_0 \mathrm{b}_{\mathrm{i}}\delta \mathrm{u}_{\mathrm{i}}\mathrm{dV}. \tag{A.2}$$

Therefore, with the use of eq. (A.1), we linearise the balance of momentum as follows:

$$\Delta \mathrm{G}_{\mathrm{mom}} = \int_{\mathrm{B}_{0\mathrm{S}}} \frac{1}{2}\,\Delta \mathrm{S}_{\mathrm{ij}}\delta \mathrm{C}_{\mathrm{ij}}\mathrm{dV} + \int_{\mathrm{B}_{0\mathrm{S}}} \frac{1}{2}\,\mathrm{S}_{\mathrm{ij}}\Delta\delta \mathrm{C}_{\mathrm{ij}}\mathrm{dV} - \int_{\mathrm{B}_{0\mathrm{S}}} \Delta\rho_0 \mathrm{b}_{\mathrm{i}}\delta \mathrm{u}_{\mathrm{i}}\mathrm{dV}. \tag{A.3}$$

Linearisation of the stress

For the linearised stress, we have

$$\begin{aligned}
\Delta \mathbf{S} &= \frac{\partial \mathbf{S}}{\partial \mathbf{E}_{\mathrm{S}}}\Delta \mathbf{E}_{\mathrm{S}} \\
&= \frac{\partial \mathbf{S}}{\partial \mathbf{C}_{\mathrm{S}}}\frac{\partial \mathbf{C}_{\mathrm{S}}}{\partial \mathbf{E}_{\mathrm{S}}}\Delta \mathbf{E}_{\mathrm{S}} \\
&= \frac{\partial \mathbf{S}}{\partial \mathbf{C}_{\mathrm{S}}}2\Delta \mathbf{E}_{\mathrm{S}} \\
&= \frac{\partial \mathbf{S}}{\partial \mathbf{C}_{\mathrm{S}}}2\frac{1}{2}\,\Delta \mathbf{C}_{\mathrm{S}} \\
&= \frac{\partial \mathbf{S}}{\partial \mathbf{C}_{\mathrm{S}}}\Delta \mathbf{C}_{\mathrm{S}}.
\end{aligned} \tag{A.4}$$

In index notation for the total stress we have

$$\mathrm{S}_{\mathrm{ij}} = \mathrm{S}^{\mathrm{E}}_{\mathrm{ij}} - \mathrm{J}\lambda \mathrm{C}^{-1}_{\mathrm{ij}}, \tag{A.5}$$

where $\mathrm{S}^{\mathrm{E}}_{\mathrm{ij}}$ is the effective stress, analogous to $\mathbf{S}^{\mathrm{S}}_{\mathrm{E}}$ when using tensor notation. Therefore, for the linearised stress we have

$$\Delta \mathrm{S}_{\mathrm{ij}} = \frac{\partial \mathrm{S}^{\mathrm{E}}_{\mathrm{ij}}}{\partial \mathrm{C}_{\mathrm{on}}} \Delta \mathrm{C}_{\mathrm{on}} - \frac{\partial \mathrm{J}}{\partial \mathrm{C}_{\mathrm{on}}} \lambda \mathrm{C}^{-1}_{\mathrm{ij}} \Delta \mathrm{C}_{\mathrm{on}} - \mathrm{J}\lambda \frac{\partial \mathrm{C}^{-1}_{\mathrm{ij}}}{\partial \mathrm{C}_{\mathrm{on}}} \Delta \mathrm{C}_{\mathrm{on}} - \mathrm{J}\mathrm{C}^{-1}_{\mathrm{ij}} \frac{\partial \lambda}{\partial \lambda} \Delta \lambda. \tag{A.6}$$

Linearisation of $\boldsymbol{\delta}\mathbf{C}_{\mathbf{S}}$

With the use of $\mathbf{C}_{\mathrm{S}} = \mathbf{F}^{\mathrm{T}}\mathbf{F}$ we have

$$\begin{aligned} \delta \mathrm{C}_{\mathrm{ij}} &= \delta \left(\mathrm{F}_{\mathrm{ki}} \mathrm{F}_{\mathrm{kj}} \right) \\ &= \delta \mathrm{F}_{\mathrm{ki}} \mathrm{F}_{\mathrm{kj}} + \mathrm{F}_{\mathrm{ki}} \delta \mathrm{F}_{\mathrm{kj}} \\ &= 2 \delta \mathrm{F}_{\mathrm{ki}} \mathrm{F}_{\mathrm{kj}} \end{aligned} \tag{A.7}$$

which yields

$$\begin{aligned} \Delta \delta \mathrm{C}_{\mathrm{ij}} &= \delta \mathrm{F}_{\mathrm{ki}} \Delta \mathrm{F}_{\mathrm{kj}} + \Delta \mathrm{F}_{\mathrm{ki}} \delta \mathrm{F}_{\mathrm{kj}} \\ &= 2 \delta \mathrm{F}_{\mathrm{ki}} \Delta \mathrm{F}_{\mathrm{kj}}. \end{aligned} \tag{A.8}$$

Linearisation of $\boldsymbol{\rho_0}$

For the density in the reference configuration we have

$$\rho_0 = \mathrm{J}(\mathrm{n}^{\mathrm{S}} \rho^{\mathrm{SR}} + \mathrm{n}^{\mathrm{F}} \rho^{\mathrm{FR}}). \tag{A.9}$$

With the use of $\mathrm{n}^{\mathrm{F}} = 1 - \mathrm{n}^{\mathrm{S}}$ we continue with

$$\begin{aligned} \rho_0 &= \mathrm{J}\mathrm{n}^{\mathrm{S}} \rho^{\mathrm{SR}} + (1 - \mathrm{n}^{\mathrm{S}}) \rho^{\mathrm{FR}} \\ &= \mathrm{J}\mathrm{n}^{\mathrm{S}} \rho^{\mathrm{SR}} + \rho^{\mathrm{FR}} - \mathrm{n}^{\mathrm{S}} \rho^{\mathrm{FR}} \end{aligned} \tag{A.10}$$

In the above, because we have assumed an incompressible material, the only dependency we have is on the Jacobian and the solid volume fraction:

$$\Delta \rho_0 = \frac{\partial \mathrm{J}}{\partial \mathrm{C}_{\mathrm{on}}} \mathrm{n}^{\mathrm{S}} \rho^{\mathrm{SR}} \Delta \mathrm{C}_{\mathrm{on}} + \frac{\partial \mathrm{n}^{\mathrm{S}}}{\partial \mathrm{n}^{\mathrm{S}}} \left\{ \mathrm{J} \rho^{\mathrm{SR}} - \rho^{\mathrm{FR}} \right\} \Delta \mathrm{n}^{\mathrm{S}}. \tag{A.11}$$

As such, linearisation of the balance of momentum proceeds as follows:

$$\begin{aligned} \Delta \mathrm{G}_{\mathrm{mom}} = &\int_{\mathrm{B}_{0\mathrm{S}}} \frac{1}{2} \frac{\partial \mathrm{S}^{\mathrm{E}}_{\mathrm{ij}}}{\partial \mathrm{C}_{\mathrm{on}}} \delta \mathrm{C}_{\mathrm{ij}} \Delta \mathrm{C}_{\mathrm{on}} \mathrm{dV} \\ &+ \int_{\mathrm{B}_{0\mathrm{S}}} \frac{1}{2} \frac{\partial \mathrm{S}^{\mathrm{E}}_{\mathrm{ij}}}{\partial \mathrm{n}^{\mathrm{S}}} \delta \mathrm{C}_{\mathrm{ij}} \Delta \mathrm{n}^{\mathrm{S}} \mathrm{dV} \\ &- \int_{\mathrm{B}_{0\mathrm{S}}} \frac{1}{2} \frac{\partial \mathrm{J}}{\partial \mathrm{C}_{\mathrm{on}}} \lambda \mathrm{C}^{-1}_{\mathrm{ij}} \delta \mathrm{C}_{\mathrm{ij}} \Delta \mathrm{C}_{\mathrm{on}} \mathrm{dV} \end{aligned}$$

$$
\begin{aligned}
&-\int_{\mathrm{B_{0S}}}\frac{1}{2}\,\mathrm{J}\lambda\frac{\partial \mathrm{C_{ij}^{-1}}}{\partial \mathrm{C_{on}}}\delta \mathrm{C_{ij}}\Delta \mathrm{C_{on}}\mathrm{dV}\\
&-\int_{\mathrm{B_{0S}}}\frac{1}{2}\,\mathrm{J}\mathrm{C_{ij}^{-1}}\frac{\partial \lambda}{\partial \lambda}\delta \mathrm{C_{ij}}\Delta \lambda\mathrm{dV}\\
&+\int_{\mathrm{B_{0S}}}\frac{1}{2}\,\mathrm{S_{ij}}2\delta \mathrm{F_{ki}}\Delta \mathrm{F_{kj}}\mathrm{dV}\\
&-\int_{\mathrm{B_{0S}}}\frac{\partial \mathrm{J}}{\partial \mathrm{C_{on}}}\mathrm{n^S}\rho^{\mathrm{SR}}\mathrm{b_i}\delta \mathrm{u_i}\Delta \mathrm{C_{on}}\mathrm{dV}.\\
&-\int_{\mathrm{B_{0S}}}\frac{\partial \mathrm{n^S}}{\partial \mathrm{n^S}}\left\{\mathrm{J}\rho^{\mathrm{SR}}-\rho^{\mathrm{FR}}\right\}\mathrm{b_i}\delta \mathrm{u_i}\Delta \mathrm{n^S}\mathrm{dV}.
\end{aligned}
\tag{A.12}
$$

We therefore need to evaluate the derivatives in eq. (A.12).

Evaluation of $\frac{\partial \mathbf{S^E_{ij}}}{\partial \mathbf{C_{on}}}$

As the stress is defined as a function of the elastic kinematics, we have

$$\mathrm{S^E_{ij}} = \mathrm{F^{g-1}_{ia}}\mathrm{S^e_{ab}}\mathrm{F^{g-1}_{jb}} \tag{A.13}$$

and the relation for the update of the mass supply defined as

$$\mathrm{n^S_g} = \mathrm{n^S_{0S}} + \mathrm{n^S_{g(n)}} + \mathrm{n^S_{g(n+1)}} \tag{A.14}$$

in which $\mathrm{n^S_{g(n)}}$ is a history variable and thus the only term updated in the current iteration process is

$$\mathrm{n^S_{g(n+1)}} = \frac{\hat{\rho}^{\mathrm{S}}}{\rho^{\mathrm{SR}}_{0\mathrm{S}}} \tag{A.15}$$

where $\hat{\rho}^{\mathrm{S}} = \hat{\rho}^{\mathrm{S}}\left(\mathbf{C}_{\mathrm{S}}\right)$. Therefore, we have

$$
\begin{aligned}
\frac{\partial \mathrm{S^E_{ij}}}{\partial \mathrm{C_{kl}}} &= 2\,\frac{\partial \mathrm{F^{g-1}_{im}}}{\partial \mathrm{C_{kl}}}\mathrm{S^E_{mn}}\mathrm{F^{g-1}_{jn}} + \mathrm{F^{g-1}_{ia}}\frac{\partial \mathrm{S^e_{ab}}}{\partial \mathrm{C^e_{rs}}}\frac{\partial \mathrm{C^e_{rs}}}{\partial \mathrm{C_{kl}}}\mathrm{F^{g-1}_{jb}}\\
&= 2\,\frac{\partial \mathrm{J_g^{-1/3}}}{\partial \mathrm{J_g}}\frac{\partial \mathrm{J_g}}{\partial \mathrm{C_{kl}}}\mathrm{S^E_{mn}}\mathrm{F^{g-1}_{jn}} + \mathrm{F^{g-1}_{ia}}\frac{\partial \mathrm{S^e_{ab}}}{\partial \mathrm{C^e_{rs}}}\frac{\partial\left\{\mathrm{F^{g-1}_{xr}}\mathrm{C_{xy}}\mathrm{F^{g-1}_{ys}}\right\}}{\partial \mathrm{C_{kl}}}\mathrm{F^{g-1}_{jb}}
\end{aligned}
\tag{A.16}
$$

with the growth part of the deformation gradient defined as $\mathbf{F}^{\mathrm{g-1}}_{\mathrm{ia}} = \delta_{\mathrm{ia}} + (\mathrm{J_g^{-1/3}} - 1)\mathrm{M^0_{ia}}$ and where the derivative of the growth part of the Jacobian is taken as

$$\frac{\partial \mathrm{J_g}}{\partial \mathrm{C_{kl}}} = \frac{\partial \mathrm{J_g}}{\partial \mathrm{n^S_g}}\frac{\partial \mathrm{n^S_g}}{\partial \mathrm{C_{kl}}} \tag{A.17}$$

where

$$\frac{\partial \mathrm{J_g}}{\partial \mathrm{n_g^S}} = -\frac{\left(\rho^{\mathrm{SR}} - \rho^{\mathrm{FR}}\right)\left(\mathrm{n_{0S}^S}\left(\rho^{\mathrm{SR}} - \rho^{\mathrm{FR}}\right) + \rho^{\mathrm{FR}}\right)}{\left(\rho^{\mathrm{SR}}\mathrm{n_g^S} - \rho^{\mathrm{FR}}\mathrm{n_g^S} + \rho^{\mathrm{FR}}\right)^2}$$

where the subscripts k,l can be replaced by o,n to arrive at the required index notation, and where the elastic constitutive tensor $\mathcal{H}^{\mathrm{e}}$ has been used, which is defined generally here, but the derivation for this investigation may be viewed in more detail in [36]. For sake of illustration within the framework of TPM and simplicity, the case of an isotropic material with a Neohookean strain energy function is derived further, which can easily be extended to accommodate a multitude of strain energy functions: For a Neohookean type approach, the effective solid stress is defined as

$$\mathrm{S_{ij}^E} = \mu^{\mathrm{S}}\left\{\delta_{\mathrm{ij}} - \mathrm{C_{ij}^{-1}}\right\} + \lambda^{\mathrm{S}}\mathrm{lnJ}\mathrm{C_{ij}^{-1}} \tag{A.18}$$

Therefore, we have

$$\begin{aligned}
\frac{\partial \mathrm{S_{ij}^E}}{\partial \mathrm{C_{on}}} &= \underbrace{\frac{\partial(\mu^S\delta_{ij})}{\partial C_{on}}}_{=0} - \mu^{\mathrm{S}}\frac{\partial \mathrm{C_{ij}^{-1}}}{\partial \mathrm{C_{on}}} + \lambda^{\mathrm{S}}\frac{\partial \mathrm{lnJ}}{\partial \mathrm{C_{on}}}\mathrm{C_{ij}^{-1}} + \lambda^{\mathrm{S}}\mathrm{lnJ}\frac{\partial \mathrm{C_{ij}^{-1}}}{\partial \mathrm{C_{on}}} \\
&= -\mu^{\mathrm{S}}\frac{\partial \mathrm{C_{ij}^{-1}}}{\partial \mathrm{C_{on}}} + \lambda^{\mathrm{S}}\frac{\partial \mathrm{lnJ}}{\partial \mathrm{C_{on}}}\mathrm{C_{ij}^{-1}} + \lambda^{\mathrm{S}}\mathrm{lnJ}\frac{\partial \mathrm{C_{ij}^{-1}}}{\partial \mathrm{C_{on}}} \qquad \text{(A.19)} \\
&= \lambda^{\mathrm{S}}\frac{\partial \mathrm{lnJ}}{\partial \mathrm{C_{on}}}\mathrm{C_{ij}^{-1}} + \frac{\partial \mathrm{C_{ij}^{-1}}}{\partial \mathrm{C_{on}}}(\lambda^{\mathrm{S}}\mathrm{lnJ} - \mu^{\mathrm{S}}). \qquad \text{(A.20)}
\end{aligned}$$

From the above, we need to evaluate $\frac{\partial \mathrm{C_{ij}^{-1}}}{\partial \mathrm{C_{on}}}$ and $\frac{\partial \mathrm{lnJ}}{\partial \mathrm{C_{on}}}$:

$$\frac{\partial \mathrm{C_{ij}^{-1}}}{\partial \mathrm{C_{on}}} = -\mathrm{C_{io}^{-1}}\mathrm{C_{jn}^{-1}} \tag{A.21}$$

Note:

$$\frac{\partial \mathrm{C_{ij}^{-1}}}{\partial \mathrm{C_{on}}} = -\frac{1}{2}\left(\mathrm{C_{io}^{-1}}\mathrm{C_{jn}^{-1}} + \mathrm{C_{in}^{-1}}\mathrm{C_{1j}^{-1}}\right)$$

$$\rightarrow \frac{\partial \mathrm{C_{ij}^{-1}}}{\partial \mathrm{C_{12}}} = -\frac{1}{2}\left(\mathrm{C_{i1}^{-1}}\mathrm{C_{2j}^{-1}} + \mathrm{C_{i2}^{-1}}\mathrm{C_{1j}^{-1}}\right)$$

$$\rightarrow \frac{\partial \mathrm{C_{ij}^{-1}}}{\partial \mathrm{C_{21}}} = -\frac{1}{2}\left(\mathrm{C_{i2}^{-1}}\mathrm{C_{1j}^{-1}} + \mathrm{C_{i1}^{-1}}\mathrm{C_{2j}^{-1}}\right)$$

symmetry of the above yields:

$$\frac{\partial \mathrm{C_{ij}^{-1}}}{\partial \mathrm{C_{on}}} = -\mathrm{C_{io}^{-1}}\mathrm{C_{jn}^{-1}}$$

(A.22)

$$\begin{aligned}
\frac{\partial \mathrm{lnJ}}{\partial \mathrm{C_{on}}} &= \frac{\partial \mathrm{lnJ}}{\partial \mathrm{J}}\frac{\partial \mathrm{J}}{\partial \mathrm{C_{on}}} \\
&= \frac{\partial \mathrm{lnJ}}{\partial \mathrm{J}}\frac{\partial\sqrt{\det\mathbf{C}}}{\partial \mathrm{C_{on}}}
\end{aligned}$$

$$
\begin{aligned}
&= \frac{\partial \mathrm{lnJ}}{\partial \mathrm{J}} \frac{\partial \sqrt{\det \mathbf{C}}}{\partial \det \mathbf{C}} \frac{\partial \det \mathbf{C}}{\partial \mathrm{C_{on}}} \\
&= \mathrm{J}^{-1} \frac{1}{2} \underbrace{\det(\mathbf{C})^{-\frac{1}{2}} \det(\mathbf{C})}_{\det(\mathbf{C})^{\frac{1}{2}} = \mathrm{J}} \mathrm{C_{no}^{-1}} \\
&= \frac{1}{2} \mathrm{C_{no}^{-1}}.
\end{aligned} \tag{A.23}
$$

Therefore, we have

$$
\begin{aligned}
\frac{\partial \mathrm{S_{ij}^E}}{\partial \mathrm{C_{on}}} &= -\mu^{\mathrm{S}} \frac{\partial \mathrm{C_{ij}^{-1}}}{\partial \mathrm{C_{on}}} + \lambda^{\mathrm{S}} \frac{\partial \mathrm{lnJ}}{\partial \mathrm{C_{on}}} \mathrm{C_{ij}^{-1}} + \lambda^{\mathrm{S}} \mathrm{lnJ} \frac{\partial \mathrm{C_{ij}^{-1}}}{\partial \mathrm{C_{on}}} \\
&= \frac{1}{2} \lambda^{\mathrm{S}} \mathrm{C_{no}^{-1}} \mathrm{C_{ij}^{-1}} - \mathrm{C_{io}^{-1}} \mathrm{C_{jn}^{-1}} (\lambda^{\mathrm{S}} \mathrm{lnJ} - \mu^{\mathrm{S}}).
\end{aligned} \tag{A.24}
$$

Evaluation of $\frac{\partial \mathbf{J}}{\partial \mathbf{C_{on}}}$

$$
\begin{aligned}
\frac{\partial \mathrm{J}}{\partial \mathrm{C_{on}}} &= \frac{\sqrt{\det \mathbf{C}}}{\partial \mathrm{C_{on}}} \\
&= \frac{\partial \sqrt{\det \mathbf{C}}}{\partial \det \mathbf{C}} \frac{\partial \det \mathbf{C}}{\partial \mathrm{C_{on}}} \\
&= \frac{1}{2} \; (\det \mathbf{C})^{-\frac{1}{2}} \; \det \mathbf{C} \; \mathrm{C_{no}^{-1}} \\
&= \frac{1}{2} \; \mathrm{J}^{-1} \mathrm{J}^2 \mathrm{C_{no}^{-1}} \\
&= \frac{1}{2} \; \mathrm{J} \mathrm{C_{no}^{-1}}
\end{aligned} \tag{A.25}
$$

Evaluation of $\frac{\partial \mathbf{J}}{\partial \mathbf{F_{on}}}$ [52]

$$
\frac{\partial \mathrm{J}}{\partial \mathrm{F_{on}}} = \mathrm{J} \mathrm{F_{no}^{-1}} \tag{A.26}
$$

Further evaluation of the derivatives leads to

$$
\begin{aligned}
\Delta \mathrm{G_{mom}} = &\int_{\mathrm{B_{0S}}} \mathrm{F_{ia}^{g-1}} \mathcal{H}^{\mathrm{e}}_{\mathrm{abrs}} \mathrm{F_{or}^{g-1}} \mathrm{F_{ns}^{g-1}} \mathrm{F_{jb}^{g-1}} \delta \mathrm{C_{ij}} \Delta \mathrm{C_{on}} \mathrm{dV} \\
&- \int_{\mathrm{B_{0S}}} \frac{1}{2} \left\{ \frac{1}{2} \mathrm{J} \mathrm{C_{no}^{-1}} \right\} \lambda \mathrm{C_{ij}^{-1}} \delta \mathrm{C_{ij}} \Delta \mathrm{C_{on}} \mathrm{dV} \\
&- \int_{\mathrm{B_{0S}}} \frac{1}{2} \mathrm{J} \lambda \left\{ -\mathrm{C_{io}^{-1}} \mathrm{C_{jn}^{-1}} \right\} \delta \mathrm{C_{ij}} \Delta \mathrm{C_{on}} \mathrm{dV}
\end{aligned}
$$

$$
\begin{aligned}
&- \int_{B_{0S}} \frac{1}{2}\, \mathrm{J} \mathrm{C}^{-1}_{ij} \delta \mathrm{C}_{ij} \Delta \lambda \mathrm{dV} \\
&+ \int_{B_{0S}} \mathrm{S}_{ij} \delta \mathrm{F}_{ki} \Delta \mathrm{F}_{kj} \mathrm{dV} \\
&+ \int_{B_{0S}} \left\{ \mathrm{J} \rho^{SR} - \rho^{FR} \right\} \mathrm{b}_i \delta \mathrm{u}_i \Delta \mathrm{n}^S \mathrm{dV} \\
&- \int_{B_{0S}} \rho^{SR} \mathrm{n}^S \left\{ \frac{1}{2}\, \mathrm{J} \mathrm{C}^{-1}_{no} \right\} \mathrm{b}_i \delta \mathrm{u}_i \Delta \mathrm{C}_{on} \mathrm{dV} \qquad \text{(A.27)}
\end{aligned}
$$

From the above, we need to evaluate δC_{ij}, ΔC_{on}, δF_{ki} and ΔF_{kj}. For the deformation gradient we have

$$
\mathbf{F} = \mathbf{1} + \mathrm{Grad}\mathbf{u} \qquad \text{(A.28)}
$$

$$
\begin{aligned}
\mathrm{F}_{ki} &= \delta_{ki} + \frac{\partial \mathrm{u}_k}{\partial \mathrm{X}_i} \\
&= \delta_{ki} + \mathrm{u}_{k,i} \qquad \text{(A.29)}
\end{aligned}
$$

$$
\delta \mathrm{F}_{ki} = \delta \mathrm{u}_{k,i} \qquad \text{(A.30)}
$$

$$
\Delta \mathrm{F}_{kj} = \Delta \mathrm{u}_{k,j} \qquad \text{(A.31)}
$$

Therefore for $\mathbf{C}$, we have:

$$
\delta \mathrm{C}_{ij} = 2 \delta \mathrm{u}_{k,i} \mathrm{F}_{kj} \qquad \text{(A.32)}
$$

And following the same approach, we also have:

$$
\Delta \mathrm{C}_{on} = 2 \Delta \mathrm{u}_{l,o} \mathrm{F}_{ln} \qquad \text{(A.33)}
$$

which yields

$$
\begin{aligned}
\Delta \mathrm{G}_{mom} = &\int_{B_{0S}} \mathrm{F}^{g-1}_{ia} \mathcal{H}^{e}_{abrs} \mathrm{F}^{g-1}_{or} \mathrm{F}^{g-1}_{ns} \mathrm{F}^{g-1}_{jb} 2 \delta \mathrm{u}_{k,i} \mathrm{F}_{kj} 2 \Delta \mathrm{u}_{l,o} \mathrm{F}_{ln} \mathrm{dV} \\
&- \int_{B_{0S}} \frac{1}{2} \left\{ \frac{1}{2}\, \mathrm{J} \mathrm{C}^{-1}_{no} \right\} \lambda \mathrm{C}^{-1}_{ij} 2 \delta \mathrm{u}_{k,i} \mathrm{F}_{kj} 2 \Delta \mathrm{u}_{l,o} \mathrm{F}_{ln} \mathrm{dV} \\
&- \int_{B_{0S}} \frac{1}{2}\, \mathrm{J} \lambda \left\{ -\mathrm{C}^{-1}_{io} \mathrm{C}^{-1}_{jn} \right\} 2 \delta \mathrm{u}_{k,i} \mathrm{F}_{kj} 2 \Delta \mathrm{u}_{l,o} \mathrm{F}_{ln} \mathrm{dV} \\
&- \int_{B_{0S}} \frac{1}{2}\, \mathrm{J} \mathrm{C}^{-1}_{ij} 2 \delta \mathrm{u}_{k,i} \mathrm{F}_{kj} \Delta \lambda \mathrm{dV} \\
&+ \int_{B_{0S}} \mathrm{S}_{ij} \delta \mathrm{u}_{k,i} \Delta \mathrm{u}_{k,j} \mathrm{dV}
\end{aligned}
$$

$$
\begin{aligned}
&+\int_{\mathrm{B_{0S}}} \left\{\mathrm{J}\rho^{\mathrm{SR}} - \rho^{\mathrm{FR}}\right\} \mathrm{b_i}\delta\mathrm{u_i}\Delta\mathrm{n^S}\mathrm{dV} \\
&-\int_{\mathrm{B_{0S}}} \rho^{\mathrm{SR}}\mathrm{n^S}\left\{\frac{1}{2}\,\mathrm{J}\mathrm{C}^{-1}_{\mathrm{no}}\right\}\mathrm{b_i}\delta\mathrm{u_i}2\Delta\mathrm{u_{l,o}}\mathrm{F_{ln}}\mathrm{dV}
\end{aligned}
\qquad (A.34)
$$

A.2 Balance of mass - mixture

We have the weak form for the balance of mass as

$$
\mathrm{G_{mass}} = -\int_{\mathrm{B_{0S}}} (\mathrm{n^F}\mathrm{w_{FS0}})_{\mathrm{i}}\delta\lambda_{,\mathrm{i}}\mathrm{dV} + \int_{\mathrm{B_{0S}}} \mathrm{J}\mathrm{E}'_{\mathrm{ij}}\mathrm{C}^{-1}_{\mathrm{ij}}\delta\lambda\mathrm{dV}, + \int_{\mathrm{B_{0S}}} \mathrm{J_S}\,\hat{\rho}^{\mathrm{S}}\left(\frac{1}{\rho^{\mathrm{FR}}} - \frac{1}{\rho^{\mathrm{SR}}}\right)\delta\lambda\mathrm{dV} \qquad (A.35)
$$

with the seepage velocity $(\mathrm{n^F}\mathrm{w_{FS0}})_{\mathrm{i}} = \mathrm{K^F}\mathrm{J_S}\left(\mathrm{C}^{-1}_{\mathrm{il}}\alpha_{\mathrm{F1}} + (1 - \alpha_{\mathrm{F1}}\mathrm{M}^0_{\mathrm{il}})\right)(-\lambda_{,\mathrm{l}})$.

With the use of eq. (A.1), we linearise the balance of mass as follows:

$$
\begin{aligned}
\Delta\mathrm{G_{mass}} = &-\int_{\mathrm{B_{0S}}} \Delta(\mathrm{n^F}\mathrm{w_{FS0}})_{\mathrm{i}}\delta\lambda_{,\mathrm{i}}\,\mathrm{dV} \\
&+\int_{\mathrm{B_{0S}}} \Delta\mathrm{J}\mathrm{E}'_{\mathrm{ij}}\mathrm{C}^{-1}_{\mathrm{ij}}\delta\lambda\mathrm{dV} \\
&+\int_{\mathrm{B_{0S}}} \mathrm{J}\Delta\mathrm{E}'_{\mathrm{ij}}\mathrm{C}^{-1}_{\mathrm{ij}}\delta\lambda\mathrm{dV} \\
&+\int_{\mathrm{B_{0S}}} \mathrm{J}\mathrm{E}'_{\mathrm{ij}}\Delta\mathrm{C}^{-1}_{\mathrm{ij}}\delta\lambda\mathrm{dV}. \\
&+\int_{\mathrm{B_{0S}}} \Delta\mathrm{J}\,\hat{\rho}^{\mathrm{S}}\left(\frac{1}{\rho^{\mathrm{FR}}} - \frac{1}{\rho^{\mathrm{SR}}}\right)\delta\lambda\mathrm{dV} \\
&+\int_{\mathrm{B_{0S}}} \mathrm{J}\,\Delta\hat{\rho}^{\mathrm{S}}\left(\frac{1}{\rho^{\mathrm{FR}}} - \frac{1}{\rho^{\mathrm{SR}}}\right)\delta\lambda\mathrm{dV}
\end{aligned}
\qquad (A.36)
$$

Linearisation of the seepage velocity

The linearised seepage velocity reads

$$
\begin{aligned}
\Delta(\mathrm{n^F}\mathrm{w_{FS0}})_{\mathrm{i}} = &\frac{\partial\mathrm{K^F}}{\partial\mathrm{F_{on}}}\mathrm{J}\left\{\mathrm{C}^{-1}_{\mathrm{il}}\alpha_{\mathrm{F1}} + \left(1 - \alpha_{\mathrm{F1}}\mathrm{M}^0_{\mathrm{il}}\right)\right\}\lambda_{,\mathrm{l}}\,\Delta\mathrm{F_{on}} \\
&-\mathrm{K^F}\frac{\partial\mathrm{J}}{\partial\mathrm{F_{on}}}\left\{\mathrm{C}^{-1}_{\mathrm{il}}\alpha_{\mathrm{F1}} + \left(1 - \alpha_{\mathrm{F1}}\mathrm{M}^0_{\mathrm{il}}\right)\right\}\lambda_{,\mathrm{l}}\,\Delta\mathrm{F_{on}} \\
&-\mathrm{K^F}\mathrm{J}\left\{\frac{\partial\mathrm{C}^{-1}_{\mathrm{il}}}{\partial\mathrm{F_{on}}}\alpha_{\mathrm{F1}}\right\}\lambda_{,\mathrm{l}}\,\Delta\mathrm{F_{on}} \\
&-\mathrm{K^F}\mathrm{J}\left\{\mathrm{C}^{-1}_{\mathrm{il}}\alpha_{\mathrm{F1}} + \left(1 - \alpha_{\mathrm{F1}}\mathrm{M}^0_{\mathrm{il}}\right)\right\}\frac{\partial\lambda_{,\mathrm{l}}}{\partial\lambda_{,\mathrm{o}}}\Delta\lambda_{,\mathrm{o}}
\end{aligned}
\qquad (A.37)
$$

which yields

$$
\begin{aligned}
\Delta(\mathrm{n^F w_{FS0}})_\mathrm{i} = {} & \frac{\partial \mathrm{K^F}}{\partial \mathrm{F_{on}}} \mathrm{J} \left\{ \mathrm{C^{-1}_{il}} \alpha_\mathrm{F1} + \left(1 - \alpha_\mathrm{F1} \mathrm{M^0_{il}}\right) \right\} \lambda_{,\mathrm{l}} \, \Delta \mathrm{F_{on}} \\
& - \mathrm{K^F J F^{-1}_{no}} \left\{ \mathrm{C^{-1}_{il}} \alpha_\mathrm{F1} + \left(1 - \alpha_\mathrm{F1} \mathrm{M^0_{il}}\right) \right\} \lambda_{,\mathrm{l}} \, \Delta \mathrm{F_{on}} \\
& - \mathrm{K^F J} \left\{ (-\mathrm{F^{-1}_{io} C^{-1}_{nl}} - \mathrm{C^{-1}_{in} F^{-1}_{ol}}) \alpha_\mathrm{F1} \right\} \lambda_{,\mathrm{l}} \, \Delta \mathrm{F_{on}} \\
& - \mathrm{K^F J} \left\{ \mathrm{C^{-1}_{il}} \alpha_\mathrm{F1} + \left(1 - \alpha_\mathrm{F1} \mathrm{M^0_{il}}\right) \right\} \delta_\mathrm{ol} \Delta \lambda_{,\mathrm{o}}
\end{aligned}
\tag{A.38}
$$

where the permeability factor is linearised depending on the choice of the dependence on deformation characterised by the factor m in eq. (4.45).

Linearisation of $\Delta \mathbf{E}'_\mathrm{ij}$

$$
\begin{aligned}
\Delta \mathrm{E}'_\mathrm{ij} & = \frac{1}{2} \, \Delta(\mathrm{F_{ki} F_{kj}})' \\
& = \frac{1}{2} \, \Delta(\mathrm{F'_{ki} F_{kj}} + \mathrm{F_{ki} F'_{kj}}) \\
& = \frac{1}{2} \, \left\{ \Delta(\mathrm{F'_{ki} F_{kj}}) + \Delta(\mathrm{F_{ki} F'_{kj}}) \right\} \\
& = \frac{1}{2} \, \left\{ \Delta \mathrm{F'_{ki} F_{kj}} + \mathrm{F'_{ki}} \Delta \mathrm{F_{kj}} + \Delta \mathrm{F_{ki} F'_{kj}} + \mathrm{F_{ki}} \Delta \mathrm{F'_{kj}} \right\} \\
& = \Delta \mathrm{F'_{ki} F_{kj}} + \mathrm{F'_{ki}} \Delta \mathrm{F_{kj}}
\end{aligned}
\tag{A.39}
$$

Following linearisation of the previous quantities, we have for the balance of mass:

$$
\begin{aligned}
\Delta(\mathrm{n^F w_{FS0}})_\mathrm{i} = {} & \int_{\mathrm{B_{0S}}} \frac{\partial \mathrm{K^F}}{\partial \mathrm{F_{on}}} \mathrm{J} \left\{ \mathrm{C^{-1}_{il}} \alpha_\mathrm{F1} + \left(1 - \alpha_\mathrm{F1} \mathrm{M^0_{il}}\right) \right\} \lambda_{,\mathrm{l}} \, \Delta \mathrm{F_{on}} \\
& - \int_{\mathrm{B_{0S}}} \mathrm{K^F} \frac{\partial \mathrm{J}}{\partial \mathrm{F_{on}}} \left\{ \mathrm{C^{-1}_{il}} \alpha_\mathrm{F1} + \left(1 - \alpha_\mathrm{F1} \mathrm{M^0_{il}}\right) \right\} \lambda_{,\mathrm{l}} \, \Delta \mathrm{F_{on}} \\
& - \int_{\mathrm{B_{0S}}} \mathrm{K^F J} \left\{ \frac{\partial \mathrm{C^{-1}_{il}}}{\partial \mathrm{F_{on}}} \alpha_\mathrm{F1} \right\} \lambda_{,\mathrm{l}} \, \Delta \mathrm{F_{on}} \\
& - \int_{\mathrm{B_{0S}}} \mathrm{K^F J} \left\{ \mathrm{C^{-1}_{il}} \alpha_\mathrm{F1} + \left(1 - \alpha_\mathrm{F1} \mathrm{M^0_{il}}\right) \right\} \frac{\partial \lambda_{,\mathrm{l}}}{\partial \lambda_{,\mathrm{o}}} \Delta \lambda_{,\mathrm{o}} \\
& + \int_{\mathrm{B_{0S}}} \frac{\partial \mathrm{J}}{\partial \mathrm{F_{on}}} \mathrm{E'_{ij} C^{-1}_{ij}} \delta \lambda \Delta \mathrm{F_{on} dV} \\
& + \int_{\mathrm{B_{0S}}} \mathrm{J F_{kj} C^{-1}_{ij}} \delta \lambda \Delta \mathrm{F'_{ki} dV} \\
& + \int_{\mathrm{B_{0S}}} \mathrm{J F'_{ki} C^{-1}_{ij}} \delta \lambda \Delta \mathrm{F_{kj} dV} \\
& + \int_{\mathrm{B_{0S}}} \mathrm{J E'_{ij}} \frac{\partial \mathrm{C^{-1}_{ij}}}{\partial \mathrm{F_{on}}} \delta \lambda \Delta \mathrm{F_{on} dV} \\
& + \int_{\mathrm{B_{0S}}} \mathrm{J F^{-1}_{no}} \, \hat{\rho}^\mathrm{S} \left(\frac{1}{\rho^\mathrm{FR}} - \frac{1}{\rho^\mathrm{SR}} \right) \delta \lambda \Delta \mathrm{F_{on} dV}
\end{aligned}
$$

$$+\int_{\mathrm{B_{0S}}} \mathrm{J}\,\Delta\hat{\rho}^{\mathrm{S}}\left(\frac{1}{\rho^{\mathrm{FR}}}-\frac{1}{\rho^{\mathrm{SR}}}\right)\delta\lambda \mathrm{dV}. \tag{A.40}$$

Following evaluation of the previously required derivatives, and with the use of

$$\begin{aligned}
\frac{\partial \mathrm{C}^{-1}_{\mathrm{ij}}}{\partial \mathrm{F}_{\mathrm{on}}} &= \frac{\partial(\mathrm{F}^{-1}_{\mathrm{ik}}\mathrm{F}^{-1}_{\mathrm{jk}})}{\partial \mathrm{F}_{\mathrm{on}}} \\
&= \frac{\partial \mathrm{F}^{-1}_{\mathrm{ik}}}{\partial \mathrm{F}_{\mathrm{on}}}\mathrm{F}^{-1}_{\mathrm{jk}} + \mathrm{F}^{-1}_{\mathrm{ik}}\frac{\partial \mathrm{F}^{-1}_{\mathrm{jk}}}{\partial \mathrm{F}_{\mathrm{on}}} \\
&= -\mathrm{F}^{-1}_{\mathrm{io}}\mathrm{F}^{-1}_{\mathrm{nk}}\mathrm{F}^{-1}_{\mathrm{jk}} - \mathrm{F}^{-1}_{\mathrm{ik}}\mathrm{F}^{-1}_{\mathrm{nk}}\mathrm{F}^{-1}_{\mathrm{jo}} \\
&= -\mathrm{F}^{-1}_{\mathrm{io}}\mathrm{C}^{-1}_{\mathrm{nj}} - \mathrm{C}^{-1}_{\mathrm{in}}\mathrm{F}^{-1}_{\mathrm{jo}}.
\end{aligned} \tag{A.41}$$

$$\frac{\partial \mathrm{F}^{-1}_{\mathrm{ij}}}{\partial \mathrm{F}_{\mathrm{on}}} = -\mathrm{F}^{-1}_{\mathrm{io}}\mathrm{F}^{-1}_{\mathrm{nj}} \qquad \text{see eq. (B.14)} \tag{A.42}$$

$$\frac{\partial \mathrm{J}}{\partial \mathrm{F}_{\mathrm{on}}} = \mathrm{J}\mathrm{F}^{-1}_{\mathrm{no}}, \tag{A.43}$$

We have the following:

$$\begin{aligned}
\Delta(\mathrm{n}^{\mathrm{F}}\mathrm{w}_{\mathrm{FS0}})_{\mathrm{i}} = &\int_{\mathrm{B_{0S}}} \frac{\partial \mathrm{K}^{\mathrm{F}}}{\partial \mathrm{F}_{\mathrm{on}}}\mathrm{J}\left\{\mathrm{C}^{-1}_{\mathrm{il}}\alpha_{\mathrm{F1}} + \left(1-\alpha_{\mathrm{F1}}\mathrm{M}^{0}_{\mathrm{il}}\right)\right\}\lambda_{,\mathrm{l}}\,\Delta \mathrm{u}_{\mathrm{o,n}} \\
&- \int_{\mathrm{B_{0S}}} \mathrm{K}^{\mathrm{F}}\mathrm{J}\mathrm{F}^{-1}_{\mathrm{no}}\left\{\mathrm{C}^{-1}_{\mathrm{il}}\alpha_{\mathrm{F1}} + \left(1-\alpha_{\mathrm{F1}}\mathrm{M}^{0}_{\mathrm{il}}\right)\right\}\lambda_{,\mathrm{l}}\,\Delta \mathrm{u}_{\mathrm{o,n}} \\
&- \int_{\mathrm{B_{0S}}} \mathrm{K}^{\mathrm{F}}\mathrm{J}\left\{-\mathrm{F}^{-1}_{\mathrm{io}}\mathrm{C}^{-1}_{\mathrm{nj}} - \mathrm{C}^{-1}_{\mathrm{in}}\mathrm{F}^{-1}_{\mathrm{jo}}\right\}\alpha_{\mathrm{F1}}\lambda_{,\mathrm{l}}\,\Delta \mathrm{F}_{\mathrm{on}} \\
&- \int_{\mathrm{B_{0S}}} \mathrm{K}^{\mathrm{F}}\mathrm{J}\left\{\mathrm{C}^{-1}_{\mathrm{il}}\alpha_{\mathrm{F1}} + \left(1-\alpha_{\mathrm{F1}}\mathrm{M}^{0}_{\mathrm{il}}\right)\right\}\frac{\partial\lambda_{,\mathrm{l}}}{\partial\lambda_{,\mathrm{o}}}\delta_{\mathrm{oj}} \\
&+ \int_{\mathrm{B_{0S}}} \mathrm{J}\mathrm{F}^{-1}_{\mathrm{no}}\mathrm{E}'_{\mathrm{ij}}\mathrm{C}^{-1}_{\mathrm{ij}}\delta\lambda\Delta \mathrm{u}_{\mathrm{o,n}}\mathrm{dV} \\
&+ \int_{\mathrm{B_{0S}}} \mathrm{J}\mathrm{F}_{\mathrm{kj}}\mathrm{C}^{-1}_{\mathrm{ij}}\delta\lambda\Delta \mathrm{u}_{\mathrm{k,i}}\frac{\beta}{\alpha\Delta \mathrm{t}}\mathrm{dV} \\
&+ \int_{\mathrm{B_{0S}}} \mathrm{J}\mathrm{F}'_{\mathrm{ki}}\mathrm{C}^{-1}_{\mathrm{ij}}\delta\lambda\Delta \mathrm{u}_{\mathrm{k,j}}\mathrm{dV} \\
&+ \int_{\mathrm{B_{0S}}} \mathrm{J}\mathrm{E}'_{\mathrm{ij}}\left\{-\mathrm{F}^{-1}_{\mathrm{io}}\mathrm{C}^{-1}_{\mathrm{nj}} - \mathrm{C}^{-1}_{\mathrm{in}}\mathrm{F}^{-1}_{\mathrm{jo}}\right\}\delta\lambda\Delta \mathrm{u}_{\mathrm{o,n}}\mathrm{dV} \\
&+ \int_{\mathrm{B_{0S}}} \mathrm{J}\mathrm{F}^{-1}_{\mathrm{no}}\,\hat{\rho}^{\mathrm{S}}\left(\frac{1}{\rho^{\mathrm{FR}}}-\frac{1}{\rho^{\mathrm{SR}}}\right)\delta\lambda\Delta \mathrm{u}_{\mathrm{o,n}}\mathrm{dV} \\
&+ \int_{\mathrm{B_{0S}}} \mathrm{J}\frac{\partial\hat{\rho}^{\mathrm{S}}}{\partial \mathrm{C}_{\mathrm{on}}}\left(\frac{1}{\rho^{\mathrm{FR}}}-\frac{1}{\rho^{\mathrm{SR}}}\right)\delta\lambda\,2\Delta \mathrm{u}_{\mathrm{l,o}}\mathrm{F}_{\mathrm{ln}}\mathrm{dV}
\end{aligned} \tag{A.44}$$

where the Newmark time discretisation scheme has been employed for $\Delta\mathrm{F}'_{\mathrm{ki}}$ (see section 4.4.1).

A.3 Balance of mass - solid

The weak form for the balance of mass for the solid phase exclusively is given as

$$\mathrm{G}^{\mathrm{s}}_{\mathrm{mass}} = \int_{\mathrm{B}_{0\mathrm{S}}} \left\{ \mathrm{J}_{\mathrm{S}}(\mathrm{n}^{\mathrm{S}})'_{\mathrm{S}} + \mathrm{J}_{\mathrm{S}}\mathrm{n}^{\mathrm{S}}\,\mathrm{tr}\,\mathbf{D}_{\mathrm{S}} - \frac{\mathrm{J}_{\mathrm{S}}}{\rho^{\mathrm{SR}}}\hat{\rho}^{\mathrm{S}} \right\} \delta\mathrm{n}^{\mathrm{S}}\,\mathrm{dV} = 0. \tag{A.45}$$

Therefore, with eq. (A.1), linearisation with respect to all degrees of freedom within the model is continued as follows:

$$\begin{aligned}
\Delta\mathrm{G}^{\mathrm{S}}_{\mathrm{mass}} &= \int_{\mathrm{B}_{0\mathrm{S}}} \left\{ \frac{\partial \mathrm{J}}{\partial \mathrm{F}_{\mathrm{on}}}(\mathrm{n}^{\mathrm{S}})'_{\mathrm{S}} \right\} \delta\mathrm{n}^{\mathrm{S}}\,\Delta\mathrm{F}_{\mathrm{on}}\mathrm{dV} \\
&= \int_{\mathrm{B}_{0\mathrm{S}}} \left\{ \mathrm{J}_{\mathrm{S}}\frac{\partial(\mathrm{n}^{\mathrm{S}})'_{\mathrm{S}}}{\partial(\mathrm{n}^{\mathrm{S}})'_{\mathrm{S}}} \right\} \delta\mathrm{n}^{\mathrm{S}}\,\Delta(\mathrm{n}^{\mathrm{S}})'_{\mathrm{S}}\mathrm{dV} \\
&= \int_{\mathrm{B}_{0\mathrm{S}}} \left\{ \frac{\partial \mathrm{J}}{\partial \mathrm{F}_{\mathrm{on}}}\mathrm{n}^{\mathrm{S}}\,\mathrm{tr}\,\mathbf{D}_{\mathrm{S}} \right\} \delta\mathrm{n}^{\mathrm{S}}\,\Delta\mathrm{F}_{\mathrm{on}}\mathrm{dV} \\
&= \int_{\mathrm{B}_{0\mathrm{S}}} \left\{ \mathrm{J}_{\mathrm{S}}\frac{\partial \mathrm{n}^{\mathrm{S}}}{\partial \mathrm{n}^{\mathrm{S}}}\,\mathrm{tr}\,\mathbf{D}_{\mathrm{S}} \right\} \delta\mathrm{n}^{\mathrm{S}}\,\Delta\mathrm{n}^{\mathrm{S}}\mathrm{dV} \\
&= \int_{\mathrm{B}_{0\mathrm{S}}} \left\{ \mathrm{J}_{\mathrm{S}}\mathrm{n}^{\mathrm{S}}\Delta\,\mathrm{tr}\,\mathbf{D}_{\mathrm{S}} \right\} \delta\mathrm{n}^{\mathrm{S}}\,\Delta\mathrm{E}'_{\mathrm{on}}\mathrm{dV} \\
&= \int_{\mathrm{B}_{0\mathrm{S}}} \left\{ \mathrm{J}_{\mathrm{S}}\mathrm{n}^{\mathrm{S}}\Delta\,\mathrm{tr}\,\mathbf{D}_{\mathrm{S}} \right\} \delta\mathrm{n}^{\mathrm{S}}\,\Delta\mathrm{F}_{\mathrm{on}}\mathrm{dV} \\
&= \int_{\mathrm{B}_{0\mathrm{S}}} \left\{ \frac{\partial \mathrm{J}_{\mathrm{S}}}{\partial \mathrm{F}_{\mathrm{on}}}\frac{1}{\rho^{\mathrm{SR}}}\hat{\rho}^{\mathrm{S}} \right\} \delta\mathrm{n}^{\mathrm{S}}\,\Delta\mathrm{F}_{\mathrm{on}}\mathrm{dV} \\
&= \int_{\mathrm{B}_{0\mathrm{S}}} \left\{ \frac{\mathrm{J}_{\mathrm{S}}}{\rho^{\mathrm{SR}}}\frac{\partial \hat{\rho}^{\mathrm{S}}}{\partial \mathrm{C}_{\mathrm{on}}} \right\} \delta\mathrm{n}^{\mathrm{S}}\,\Delta\mathrm{C}_{\mathrm{on}}\mathrm{dV}
\end{aligned}$$

wherein the term $\Delta\,\mathrm{tr}\,\mathbf{D}_{\mathrm{S}}$ has been addressed in eq. (A.39) yielding

$$\begin{aligned}
\Delta\mathrm{G}^{\mathrm{S}}_{\mathrm{mass}} &= \int_{\mathrm{B}_{0\mathrm{S}}} \left\{ \mathrm{J}\mathrm{F}^{-1}_{\mathrm{no}}(\mathrm{n}^{\mathrm{S}})'_{\mathrm{S}} \right\} \delta\mathrm{n}^{\mathrm{S}}\,\Delta\mathrm{u}_{\mathrm{o,n}}\mathrm{dV} \\
&= \int_{\mathrm{B}_{0\mathrm{S}}} \left\{ \mathrm{J} \right\} \delta\mathrm{n}^{\mathrm{S}}\,\frac{\beta}{\alpha\Delta\mathrm{t}}\Delta\mathrm{n}^{\mathrm{S}}\mathrm{dV} \\
&= \int_{\mathrm{B}_{0\mathrm{S}}} \left\{ \mathrm{J}\mathrm{F}^{-1}_{\mathrm{no}}\mathrm{n}^{\mathrm{S}}\,\mathrm{tr}\,\mathbf{D}_{\mathrm{S}} \right\} \delta\mathrm{n}^{\mathrm{S}}\,\Delta\mathrm{u}_{\mathrm{o,n}}\mathrm{dV} \\
&= \int_{\mathrm{B}_{0\mathrm{S}}} \left\{ \mathrm{J}\,\mathrm{tr}\,\mathbf{D}_{\mathrm{S}} \right\} \delta\mathrm{n}^{\mathrm{S}}\,\Delta\mathrm{n}^{\mathrm{S}}\mathrm{dV} \\
&= \int_{\mathrm{B}_{0\mathrm{S}}} \left\{ \mathrm{J}\mathrm{n}^{\mathrm{S}}\Delta\,\mathrm{tr}\,\mathbf{D}_{\mathrm{S}} \right\} \delta\mathrm{n}^{\mathrm{S}}\,\Delta\mathrm{E}'_{\mathrm{on}}\mathrm{dV} \\
&= \int_{\mathrm{B}_{0\mathrm{S}}} \left\{ \mathrm{J}\mathrm{n}^{\mathrm{S}}\Delta\,\mathrm{tr}\,\mathbf{D}_{\mathrm{S}} \right\} \delta\mathrm{n}^{\mathrm{S}}\,\Delta\mathrm{F}_{\mathrm{on}}\mathrm{dV} \\
&= \int_{\mathrm{B}_{0\mathrm{S}}} \left\{ \mathrm{J}\mathrm{F}^{-1}_{\mathrm{no}}\frac{1}{\rho^{\mathrm{SR}}}\hat{\rho}^{\mathrm{S}} \right\} \delta\mathrm{n}^{\mathrm{S}}\,\Delta\mathrm{u}_{\mathrm{o,n}}\mathrm{dV}
\end{aligned}$$

$$= \int_{\mathrm{B_{0S}}} \left\{ \frac{\mathrm{J}}{\rho^{\mathrm{SR}}} \frac{\partial \hat{\rho}^{\mathrm{S}}}{\partial \mathrm{C_{on}}} \right\} \delta \mathrm{n^S} \, 2\Delta \mathrm{u_{l,o}} \mathrm{F_{ln}} \mathrm{dV}$$

where the Newmark time discretisation scheme has been employed for $\Delta(\mathrm{n^S})'_{\mathrm{S}}$ (see section 4.4.1) and is further employed for $\Delta \mathrm{E}'_{\mathrm{on}}$.

Appendix B

Additional derivations

Material velocity gradient $(\mathbf{F}_{\mathrm{S}})'_{\mathrm{S}}$

Considering $(\mathbf{F}_{\mathrm{S}})'_{\mathrm{S}} = \mathrm{Grad}\mathbf{x}'_{\mathrm{S}}$ in index notation as $\mathrm{F}'_{\mathrm{ij}}$ we have the approximated material time derivative of the deformation gradient considering a displacement increment per time step:

$$
\begin{aligned}
\mathrm{F}'_{\mathrm{ij}} &= \frac{\partial}{\partial \mathrm{t}} \frac{\partial \mathrm{x_i}}{\partial \mathrm{X_j}} \\
&= \frac{\partial}{\partial \mathrm{X_j}} \frac{\partial \mathrm{x_i}}{\partial \mathrm{t}} \\
&= \frac{\partial}{\partial \mathrm{X_j}} \mathrm{v_i} \\
&= \frac{\partial}{\partial \mathrm{X_j}} \frac{\Delta \mathrm{u_i}}{\Delta \mathrm{t}} \\
&= \frac{\Delta \mathrm{u_{i,j}}}{\Delta \mathrm{t}}
\end{aligned} \tag{B.1}
$$

Green strain rate $(\mathbf{E}_{\mathrm{S}})'_{\mathrm{S}}$

With the use of the spatial velocity gradient $\mathbf{L}_{\mathrm{S}} = \left(\mathrm{Grad}\mathbf{x}'_{\mathrm{S}}\right) \mathbf{F}_{\mathrm{S}}^{-1}$, we have for the Green strain rate

$$
\begin{aligned}
(\mathbf{E}_{\mathrm{S}})'_{\mathrm{S}} &= \left[\frac{1}{2}\ \left(\mathbf{F}^{\mathrm{T}}\mathbf{F} - \mathbf{1}\right)\right]' \\
&= \frac{1}{2}\ \left[(\mathbf{F}_{\mathrm{S}})'^{\mathrm{T}}_{\mathrm{S}}\, \mathbf{F} + (\mathbf{F}_{\mathrm{S}})'^{\mathrm{T}}_{\mathrm{S}}\, (\mathbf{F}_{\mathrm{S}})'_{\mathrm{S}}\right] \\
&= \frac{1}{2}\, \mathbf{F}^{\mathrm{T}} \left[\mathbf{F}^{-\mathrm{T}}\, (\mathbf{F}_{\mathrm{S}})'^{\mathrm{T}}_{\mathrm{S}}\, \mathbf{F}\mathbf{F}_{\mathrm{S}}^{-1} + \mathbf{F}^{-\mathrm{T}}\mathbf{F}^{\mathrm{T}}\, (\mathbf{F}_{\mathrm{S}})'_{\mathrm{S}}\, \mathbf{F}_{\mathrm{S}}^{-1}\right] \mathbf{F} \\
&= \frac{1}{2}\, \mathbf{F}^{\mathrm{T}} \left[\mathbf{F}^{-\mathrm{T}}\, (\mathbf{F}_{\mathrm{S}})'^{\mathrm{T}}_{\mathrm{S}} + (\mathbf{F}_{\mathrm{S}})'^{\mathrm{T}}_{\mathrm{S}}\, \mathbf{F}_{\mathrm{S}}^{-1}\right] \mathbf{F} \\
&= \frac{1}{2}\, \mathbf{F}^{\mathrm{T}} \left[\mathbf{F}^{-\mathrm{T}}\mathbf{F}^{\mathrm{T}}\mathbf{L}_{\mathrm{S}}^{\mathrm{T}} + \mathbf{L}\mathbf{F}\mathbf{F}_{\mathrm{S}}^{-1}\right] \mathbf{F} \\
&= \frac{1}{2}\, \mathbf{F}^{\mathrm{T}} \left[\mathbf{L}_{\mathrm{S}}^{\mathrm{T}} + \mathbf{L}\right] \mathbf{F} \\
&= \mathbf{F}^{\mathrm{T}}\mathbf{D}\mathbf{F}
\end{aligned} \tag{B.2}
$$

In index notation, we have

$$\begin{aligned}
\mathrm{E}'_{\mathrm{ij}} &= \frac{1}{2}\ \left[\mathrm{F}'_{\mathrm{ki}}\mathrm{F}_{\mathrm{kj}} + \mathrm{F}_{\mathrm{ki}}\mathrm{F}'_{\mathrm{kj}}\right] \\
&= \frac{1}{2}\left[\frac{\Delta \mathrm{u}_{\mathrm{k,i}}}{\Delta \mathrm{t}}\mathrm{F}_{\mathrm{kj}} + \mathrm{F}_{\mathrm{ki}}\frac{\Delta \mathrm{u}_{\mathrm{k,j}}}{\Delta \mathrm{t}}\right] \qquad \text{(B.3)}
\end{aligned}$$

Evaluation of $\boldsymbol{\delta}\left(\mathbf{E_S}\right)_{\mathbf{ij}}$ and $\boldsymbol{\Delta}\left(\mathbf{E_S}\right)_{\mathbf{on}}$

$$\begin{aligned}
\mathrm{E}_{\mathrm{ij}} &= \frac{1}{2}\left(\mathrm{C}_{\mathrm{ij}} - \delta_{\mathrm{ij}}\right) \\
&= \frac{1}{2}\left(\mathrm{F}_{\mathrm{ki}}\mathrm{F}_{\mathrm{kj}} - \delta_{\mathrm{ij}}\right) \qquad \text{(B.4)}
\end{aligned}$$

$$\begin{aligned}
\delta \mathrm{E}_{\mathrm{ij}} &= \frac{1}{2}\left(\delta \mathrm{F}_{\mathrm{ki}}\mathrm{F}_{\mathrm{kj}} + \mathrm{F}_{\mathrm{ki}}\delta \mathrm{F}_{\mathrm{kj}}\right) \\
&= \delta \mathrm{F}_{\mathrm{ki}}\mathrm{F}_{\mathrm{kj}} \qquad \text{(due to symmetry)} \qquad \text{(B.5)}
\end{aligned}$$

(Only when multiplied with the symmetric 2^{nd} Piola $\mathbf{S}$ this simplification is valid).

$$\mathbf{F} = 1 + \mathrm{Grad}\mathbf{u} \qquad \text{(B.6)}$$

$$\begin{aligned}
\mathrm{F}_{\mathrm{ki}} &= \delta_{\mathrm{ki}} + \frac{\partial \mathrm{u}_{\mathrm{k}}}{\partial \mathrm{X}_{\mathrm{i}}} \\
&= \delta_{\mathrm{ki}} + \mathrm{u}_{\mathrm{k,i}} \qquad \text{(B.7)}
\end{aligned}$$

$$\delta \mathrm{F}_{\mathrm{ki}} = \delta \mathrm{u}_{\mathrm{k,i}} \qquad \text{(B.8)}$$

Therefore, we have:

$$\delta \mathrm{E}_{\mathrm{ij}} = \delta \mathrm{u}_{\mathrm{k,i}}\mathrm{F}_{\mathrm{kj}} \qquad \text{(B.9)}$$

And following the same approach, we also have:

$$\Delta \mathrm{E}_{\mathrm{on}} = \Delta \mathrm{u}_{\mathrm{l,o}}\mathrm{F}_{\mathrm{ln}} \qquad \text{(B.10)}$$

Side note

From eq. (B.9), we gain the following relations:

$$\delta\mathbf{E}_\mathrm{S} = \mathrm{Grad}\delta\mathbf{u}_\mathrm{S}\mathbf{F}_\mathrm{S} \tag{B.11}$$

$$\mathrm{Grad}\delta\mathbf{u}_\mathrm{S} = \mathbf{F}_\mathrm{S}^{-1}\delta\mathbf{E}_\mathrm{S} \tag{B.12}$$

Evaluation of $\boldsymbol{\delta}\mathbf{C_{ij}}$

$$\mathrm{C_{ij}} = \mathrm{F_{ki}F_{kj}} \tag{B.13}$$

$$\begin{aligned}\delta\mathrm{C_{ij}} &= \delta\mathrm{F_{ki}F_{kj}} + \mathrm{F_{ki}}\delta\mathrm{F_{kj}}\\ &= 2\delta\mathrm{F_{ki}F_{kj}} \qquad\qquad \text{(symmetry)}\\ &= 2\delta\mathrm{u_{k,i}F_{kj}}\end{aligned}$$

Evaluation of $\frac{\boldsymbol{\partial}\mathbf{F^{-1}}}{\boldsymbol{\partial}\mathbf{F}}$

$$\begin{aligned}&\mathbf{F}^{-1}\mathbf{F} = 1\\ &\frac{\partial\mathbf{F}^{-1}}{\partial\mathbf{F}}\mathbf{F} + \mathbf{F}^{-1}\frac{\partial\mathbf{F}}{\partial\mathbf{F}} = 0\\ &\frac{\partial\mathbf{F}^{-1}}{\partial\mathbf{F}}\mathbf{F} = -\mathbf{F}^{-1}\frac{\partial\mathbf{F}}{\partial\mathbf{F}}\\ &\frac{\partial\mathbf{F}^{-1}}{\partial\mathbf{F}} = -\mathbf{F}^{-1}\frac{\partial\mathbf{F}}{\partial\mathbf{F}}\mathbf{F}^{-1}\\ &\frac{\partial\mathrm{F}_\mathrm{ik}^{-1}}{\partial\mathrm{F}_\mathrm{on}} = -\mathrm{F}_\mathrm{ij}^{-1}\frac{\partial\mathrm{F}_\mathrm{jl}}{\partial\mathrm{F}_\mathrm{on}}\mathrm{F}_\mathrm{lk}^{-1}\\ &\frac{\partial\mathrm{F}_\mathrm{ik}^{-1}}{\partial\mathrm{F}_\mathrm{on}} = -\mathrm{F}_\mathrm{ij}^{-1}\delta_\mathrm{jo}\delta_\mathrm{ln}\mathrm{F}_\mathrm{lk}^{-1}\\ &\frac{\partial\mathrm{F}_\mathrm{ik}^{-1}}{\partial\mathrm{F}_\mathrm{on}} = -\mathrm{F}_\mathrm{io}^{-1}\mathrm{F}_\mathrm{nk}^{-1}\end{aligned} \tag{B.14}$$

Appendix C

Ethics approval

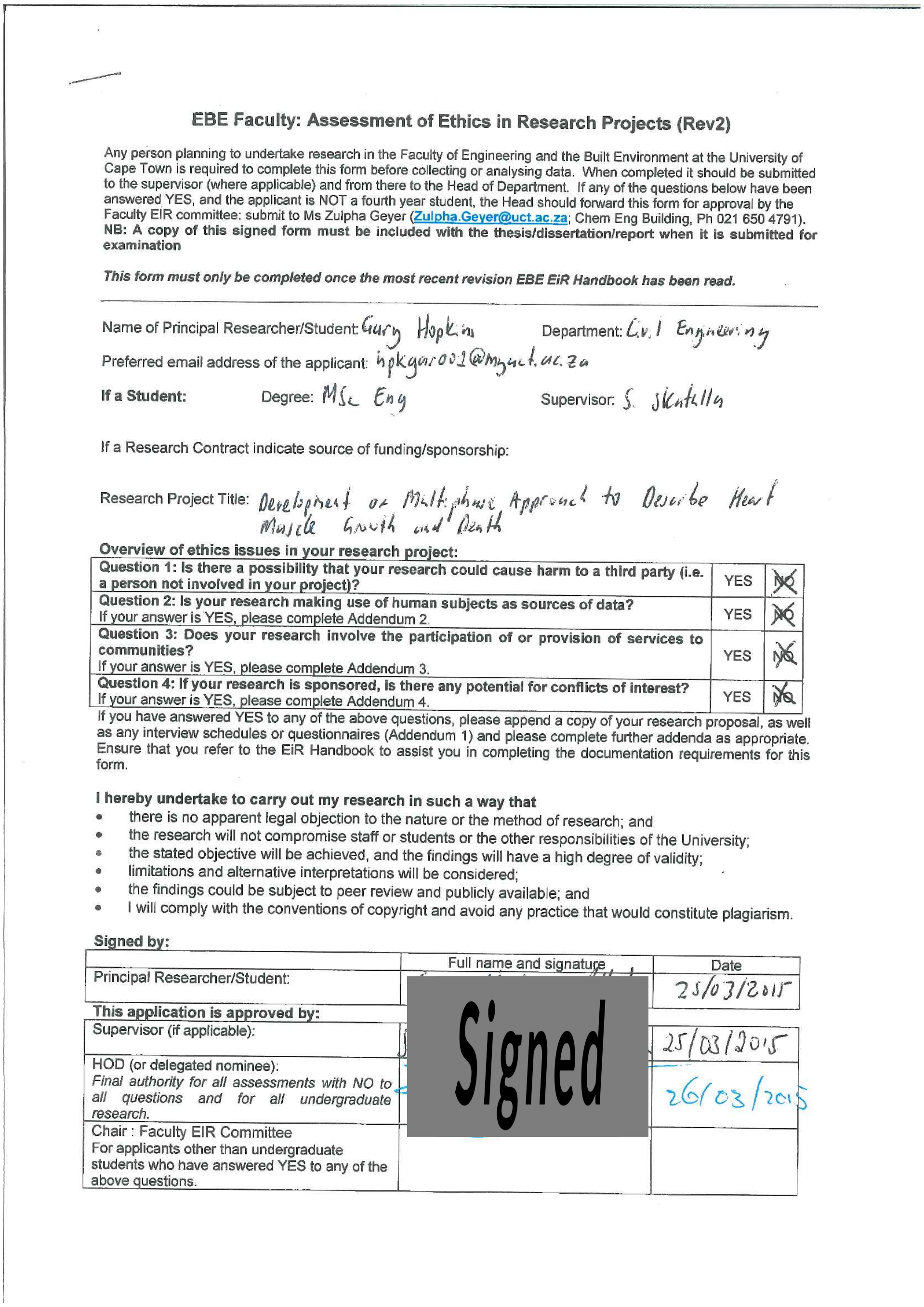

EBE Faculty: Assessment of Ethics in Research Projects (Rev2)

Any person planning to undertake research in the Faculty of Engineering and the Built Environment at the University of Cape Town is required to complete this form before collecting or analysing data. When completed it should be submitted to the supervisor (where applicable) and from there to the Head of Department. If any of the questions below have been answered YES, and the applicant is NOT a fourth year student, the Head should forward this form for approval by the Faculty EIR committee: submit to Ms Zulpha Geyer (Zulpha.Geyer@uct.ac.za; Chem Eng Building, Ph 021 650 4791).
NB: A copy of this signed form must be included with the thesis/dissertation/report when it is submitted for examination

This form must only be completed once the most recent revision EBE EiR Handbook has been read.

Name of Principal Researcher/Student: Gary Hopkins   Department: Civil Engineering

Preferred email address of the applicant: hpkgar001@myuct.ac.za

If a Student: Degree: MSc Eng   Supervisor: S. Skatulla

If a Research Contract indicate source of funding/sponsorship:

Research Project Title: Development of Multiphase Approach to Describe Heart Muscle Growth and Death

Overview of ethics issues in your research project:

Question 1: Is there a possibility that your research could cause harm to a third party (i.e. a person not involved in your project)?	YES	[✓ NO]
Question 2: Is your research making use of human subjects as sources of data? If your answer is YES, please complete Addendum 2.	YES	[✓ NO]
Question 3: Does your research involve the participation of or provision of services to communities? If your answer is YES, please complete Addendum 3.	YES	[✓ NO]
Question 4: If your research is sponsored, is there any potential for conflicts of interest? If your answer is YES, please complete Addendum 4.	YES	[✓ NO]

If you have answered YES to any of the above questions, please append a copy of your research proposal, as well as any interview schedules or questionnaires (Addendum 1) and please complete further addenda as appropriate. Ensure that you refer to the EiR Handbook to assist you in completing the documentation requirements for this form.

I hereby undertake to carry out my research in such a way that

- there is no apparent legal objection to the nature or the method of research; and
- the research will not compromise staff or students or the other responsibilities of the University;
- the stated objective will be achieved, and the findings will have a high degree of validity;
- limitations and alternative interpretations will be considered;
- the findings could be subject to peer review and publicly available; and
- I will comply with the conventions of copyright and avoid any practice that would constitute plagiarism.

Signed by:

	Full name and signature	Date
Principal Researcher/Student:	Signed	25/03/2015

This application is approved by:

Supervisor (if applicable):		25/03/2015
HOD (or delegated nominee): *Final authority for all assessments with NO to all questions and for all undergraduate research.*		26/03/2015
Chair : Faculty EIR Committee For applicants other than undergraduate students who have answered YES to any of the above questions.		

Figure C.1. 2015 ethics approval

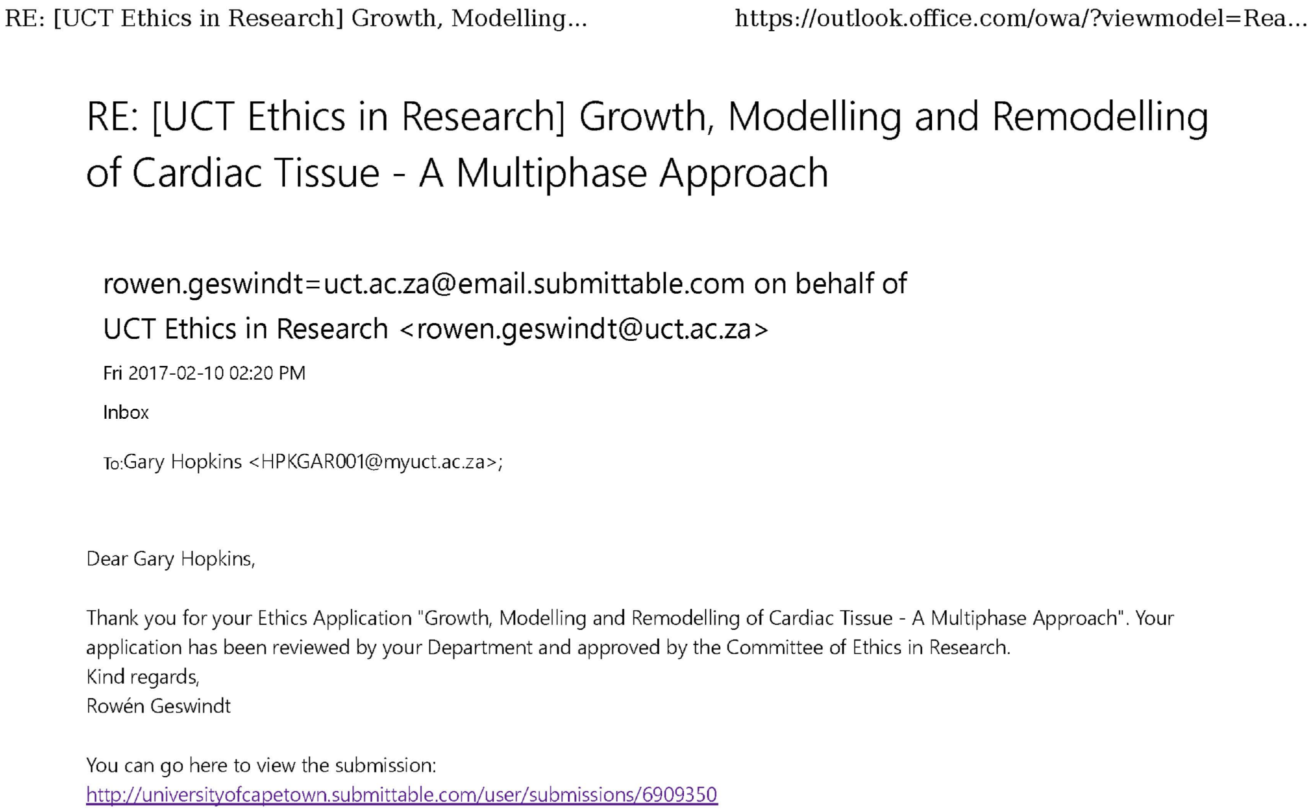

RE: [UCT Ethics in Research] Growth, Modelling... https://outlook.office.com/owa/?viewmodel=Rea...

RE: [UCT Ethics in Research] Growth, Modelling and Remodelling of Cardiac Tissue - A Multiphase Approach

rowen.geswindt=uct.ac.za@email.submittable.com on behalf of
UCT Ethics in Research <rowen.geswindt@uct.ac.za>
Fri 2017-02-10 02:20 PM
Inbox

To:Gary Hopkins <HPKGAR001@myuct.ac.za>;

Dear Gary Hopkins,

Thank you for your Ethics Application "Growth, Modelling and Remodelling of Cardiac Tissue - A Multiphase Approach". Your application has been reviewed by your Department and approved by the Committee of Ethics in Research.
Kind regards,
Rowén Geswindt

You can go here to view the submission:
http://universityofcapetown.submittable.com/user/submissions/6909350

Figure C.2. 2017 ethics approval; required due to change in response of Question 2 in Fig. C.1 from “No” to “Yes”.

List of References

[1] J. Aguado-Sierra, A. Krishnamurthy, C. Villongco, J. Chuang, E. Howard, M.J. Gonzales, J. Omens, D.E. Krummen, S. Narayan, R.C.P. Kerckhoffs, and A.D.. McCulloch. Patient-specific modeling of dyssynchronous heart failure: A case study. *Progress in Biophysics and Molecular Biology*, 107(1):147 – 155, 2011. ISSN 0079-6107. doi: http://dx.doi.org/10.1016/j.pbiomolbio.2011.06.014. URL `http://www.sciencedirect.com/science/article/pii/S0079610711000617`. Experimental and Computational Model Interactions in Bio-Research: State of the Art.

[2] D. Ambrosi and S. Pezzuto. Active stress vs. active strain in mechanobiology: constitutive issues. *Journal of Elasticity*, 2011. doi: 10.1007/s10659-011-9351-4.

[3] D. Ambrosi, A. Guillou, and ES. Di Martino. Stress-modulated remodeling of a nonhomogeneous body. *Biomechanics and Modeling in Mechanobiology*, 7(1):63–76, 2008.

[4] American Heart Association . Heart disease and stroke statistics 2014 update. *Circulation*, 129:e28–e292, 2014. doi: https://doi.org/10.1161/01.cir.0000441139.02102.80.

[5] American Heart Association. Heart disease and stroke statistics - 2007 update: A report from the american heart association statistics committee and stroke statistics subcommittee. *Circulation*, 2007. doi: https://doi.org/10.1161/CIRCULATIONAHA.106.179918.

[6] G. Ateshian. On the theory of reactive mixtures for modeling biological growth. *Biomechan Model Mechanobiol*, 6:423–445, 2007.

[7] G. Ateshian and JD. Humphrey. Continuum mixture models of biological growth and remodeling: Past successes and future opportunities. *Annual Review of Biomedical Engineering*, 14(1):91–111, 2012. doi: 10.1146/annurev-bioeng-071910-124726.

[8] G. Ateshian and T. Ricken. Multigenerational interstitial growth of biological tissues. *Biomechanics and Modeling in Mechanobiology*, 9:689–702, 2010. doi: 10.1007/s10237-010-0205-y.

[9] R.J. Atkin and R.E. Crain. Continuum theories of mixtures: Basic theory and historical development. *The Quarterly Journal of Mechanics and Applied Mathematics*, 29:209 – 244, 1976.

[10] I. Babuška. Error bounds for finite element method. *Numerische Mathematik*, 16:322–333, 1971.

[11] B. Baillargeon, N. Rebelo, DD. Fox, RL. Taylor, and E. Kuhl. The living heart project: A robust and integrative simulator for human heart function. *European Journal of Mechanics A/Solids*, 48:38–47, April 2014. doi: 10.1016/j.euromechsol.2014.04.001.

[12] F. Bartel, T. Ricken, J Schröder, and J. Bluhm. A two-scale homogenisation approach for fluid saturated porous media based on tpm and fe2-method. *Proc. Appl. Math. Mech.*, 15:447–448, 2016. doi: doi:10.1002/pamm.201510214.

[13] F. Bartel, T. Ricken, J Schröder, and J. Bluhm. Remarks on coupled multi-scale simulations and high performance computation. *Proc. Appl. Math. Mech.*, 16:511–512, 2016. doi: DOI10.1002/pamm.201610244.

[14] K. Bathe. The inf–sup condition and its evaluation for mixed finite element methods. *Computer and Structures*, 79(2):243–252, 2001.

[15] ET. Bell. *Men of Mathematics: The Lives and Achievements of the Great Mathematicians from Zeno to Poincare.* Simon & Schuster, New York, 1986.

[16] MA. Biot. General theory of three dimensional consolidation. *Journal of Applied Physics*, 12:155–164, 1941.

[17] J. Bluhm. *In Porous media : theory, experiments and numerical applications*, chapter Modelling of saturated thermo-elastic porous solids with different phase temperatures. Springer-Verlag Berlin, Heidelberg, New York, 2002.

[18] R. Bowen. Incompressible porous media models by use of the theory of mixtures. *International Journal of Engineering Science*, 20(6):697–735, 1980.

[19] R. Bowen. Compressible porous media models by use of the theory of mixtures. *International Journal of Engineering Science*, 20(6):697–735, 1982.

[20] RM. Bowen. Theory of mixtures. In AC. Eringen, editor, *Continuum Physics*, volume 3, chapter 1, pages 1–127. Academic Press, New York, 1976.

[21] F. Brezzi. On the existance, uniqueness and approxamation of saddle-point problems arising from lagrange multipliers. *R.A.I.R.O*, 8(R2):129–151, 1974.

[22] Cape Universities Body Imaging Centre. Faculty of Health Sciences UCT, Groote Schuur Hospital, Cape Town, South Africa.

[23] R. S. Chadwick. Mechanics of the left ventricle. *Biophys J*, 39(3):279–88, Sep 1982. doi: 10.1016/S0006-3495(82)84518-9.

[24] D. Chang. Wiggers diagram, showing various events of a cardiac cycle. Online, March 2012. URL `http://commons.wikimedia.org/wiki/File:Wiggers_Diagram.svg`. This file is licensed under the Creative Commons Attribution-Share Alike 2.5 Generic license.

[25] P. Ciarletta, D. Ambrosi, and GA. Maugin. Mass transport in morphogenetic processes: A second gradient theory for volumetric growth and material remodeling. *Journal of the Mechanics and Physics of Solids*, 60(3):432–450, March 2012. doi: doi:10.1016/j.jmps.2011.11.011.

[26] B. D. Coleman and W. Noll. The thermodynamics of elastic materials with heat conduction and viscosity. *Archives for Rational Mechanics and Analalyis*, 13:167–178, 1963. doi: http://dx.doi.org/10.1016/0022-247X(67)90180-1.

[27] R. de Boer. Highlights in the historical development of the porous media theory: toward a transistent macroscopic theory. *Applied Mechanics Reviews*, 49(4):201–262, 1996.

[28] Reint de Boer. *Theory of Porous Media: Highlights in the Historical Development and Current State.* Springer-Verlag Berlin Heidelberg, 1 edition, 2000. doi: 10.1007/978-3-642-59637-7.

[29] A.K. Didwania and R. de Boer. Saturated compressible and incompressible porous solids : Macro- and micromechanical approaches. *Transport in Porous Media*, 34:101–115, 1999.

[30] R. Dongaonkar, R.H. Stewart, H.J. Geissler, and G.A. Laine. Myocardial microvascular permeability, interstitial oedema, and compromised cardiac function. *Cardiovascular Research*, 87(2):331–339, 2010.

[31] D. Donker, P. Volders, T. Arts, B. Bekkers, L Hofstra, R Sptjens, J Beekman, M Borgers, H Crijns, and M Vos. End-diastolic myofiber stress and ejection strain increase with ventricular volume overload: Serial in-vivo analyses in dogs with complete atrioventricular block. *Basic Research in Cardiology*, 100(4):372–382, 2005.

[32] D Drumheller. The theoretical treatment of a porous solid using a mixture theory. *International Jornal of Solids and Structures 14 (6)*, 14(6):441–456, 1978.

[33] W. Ehlers. *Porous Media: Theory, Experiments and Numerical Applications,*, chapter Foundations of multiphasic and porous materials, pages 3–86. Springer-Verlag, Berlin, 2002.

[34] W. Ehlers. Challenges of porous media models in geo- and biomechanical engineering including electro-chemically active polymers and gels. *International Journal of Advances in Engineering Sciences and Applied Mathematics*, 1:1–24, 2009.

[35] Wolfgang Ehlers, Robert Krause, and Bernd Markert. Modelling and remodelling of biological tissue in the framework of continuum biomechanics. *Pamm*, 11(1):35–38, 2011. ISSN 16177061. doi: 10.1002/pamm.201110010. URL `http://doi.wiley.com/10.1002/pamm.201110010`.

[36] M. Essack. Material parameter identification for modelling the left ventricle in the healthy state. Master's thesis, University of Cape Town, 2014.

[37] MR. Essop and VT. Nkomo. Rheumatic and nonrheumatic valvular heart disease: Epidemiology, management, and prevention in africa. *Circulation*, 112:3854–3591, 2005. doi: 10.1161/CIRCULATIONAHA.105.539775.

[38] F. Feyel. Multiscale FE^2 elastoviscoplastic analysis of composite structures. *Computational Materials Science*, 1999.

[39] F. Feyel. A multilevel finite element method (fe^2) to describe the response of highly nonlinear structures using generalized continua. *Computer Methods in Applied Mechanics and Engineering*, 192:3233–3244, 2003.

[40] V. Fuster, R.A. Walsh, and R.G. Harrington. *Hurst's The Heart*, volume 1. McGraw-Hill Medical (Hersteller), 13 edition, 2011.

[41] AM. Gerdes. The use of isolated myocytes to evaluate myocardial remodeling. *Trends in Cardiovascular Medicine*, 2(4):152–155, July - August 1992.

[42] S. Göktepe, O.J. Abilez, and E. Kuhl. A generic approach towards finite growth with examples of athletes heart, cardiac dilation, and cardiac wall thickening. *Journal of the Mechanics and Physics of Solids*, 58:1661–1680, 2010. doi: 10.1016/j.jmps.2010.07.003.

[43] S. Göktepe, OJ. Abilez, KK. Parker, and E. Kuhl. A multiscale model for eccentric and concentric cardiac growth through sarcomerogenesis. *Journal of Theoretical Biology*, 265(3):433–442, 2010.

[44] S. Göktepe, S.N.S. Acharya, J. Wong, and E. Kuhl. Computational modelling of passive myocardium. *International Journal for Numerical Methods in Biomedical Engineering*, 27:1–12, 2011.

[45] D. Gorton, B. Govan, C. Olive, and N. Ketheesan. A role for an animal model in determining the immune mechanisms involved in the pathogenesis of rheumatic heart disease. *International Congress Series*, 1289:289–292, 2006. doi: 10.1016/j.ics.2005.11.079.

[46] H. L. Granzier and T. C. Irving. Passive tension in cardiac muscle: contribution of collagen, titin, microtubules, and intermediate filaments. *Biophys J*, 68(3):1027–44, Mar 1995. doi: 10.1016/S0006-3495(95)80278-X.

[47] W Grossman, D Jones, and LP McLaurin. Wall stress and patterns of hypertrophy in human left-ventricle. *Journal of Clinical Investigation*, 56:56–64, 1975.

[48] J. M. Guccione and A. D. McCulloch. Mechanics of active contraction in cardiac muscle: Part i–constitutive relations for fiber stress that describe deactivation. *J Biomech Eng*, 115(1):72–81, Feb 1993. doi: 10.1115/1.2895473.

[49] J M Guccione, L K Waldman, and A D McCulloch. Mechanics of active contraction in cardiac muscle: Part ii-cylindrical models of the systolic left ventricle. *ASME Journal of Biomechanical Engineering*, 115:82–90, 1993. doi: 10.1115/1.2895474.

[50] F. Guyon and R. Le Riche. Least squares parameter estimation and the levenberg-marquardt algorithm: Deterministic analysis, sensistivities and numerical experiments. Technical Report 041/99, Indian National Science Academy, 2000.

[51] I.P. Herman. *Physics of the Human Body*. Biological and Medical Physics, Biomedical Engineering. Springer International Publishing, 2 edition, 2016. doi: 10.1007/978-3-319-23932-3. Page 603.

[52] G. Holzapfel. *Nonlinear Solid Mechanics*. John Wiley & Son Ltd, 2000.

[53] T.J.R. Hughes. *The Finite Element Method: Linear Static and Dynamic Finite Element Analysis*. PrenPrentice-Hall., 1987.

[54] Human Anatomy System. Microscopic anatomy of cardiac muscle microscopic anatomy of cardiac muscle ocr a level biology. Online, September 2016. URL `https://www.anatomylibrary.us/microscopic-anatomy-of-cardiac-muscle/microscopic-anatomy-of-cardiac-muscle-microscopic-anatomy-of-cardiac-muscle-ocr-a-l`

[55] JD. Humphrey. Continuum biomechanics of soft biological tissues. *The Royal Society*, 459:3–46, 2003.

[56] S. Imatani and G. Maugin. A constitutive model for material growth and its application to three-dimensional finite element analysis. *Mechanics Research Communications*, 29 (6):477–483, November-December 2002. doi: doi:10.1016/S0093-6413(02)00294-X.

[57] Yumiko Kanzaki, Fumio Terasaki, Makoto Okabe, Shuichi Fujita, Takashi Katashima, Kaoru Otsuka, and Nobukazu Ishizaka. Images in cardiovascular medicine: Three-dimensional architecture of cardiomyocytes and connective tissue in human heart revealed by scanning electron microscopy. *Circulation*, 122(19):1973–1974, November 2010. URL `http://circ.ahajournals.org/content/122/19/1973/F2.full`.

[58] Arnold M. Katz. *Physiology of the heart*. Wolters Kluwer and Lippincott Williams & Wilkins, fifth edition edition, 2011.

[59] R. C. Kerckhoffs, O. P. Faris, P. H. Bovendeerd, F. W. Prinzen, K. Smits, E. R. McVeigh, and T. Arts. Timing of depolarization and contraction in the paced canine left ventricle: model and experiment. *J Cardiovasc Electrophysiol*, 14(10 Suppl):S188–95, Oct 2003. doi: 10.1046/j.1540.8167.90310.x.

[60] R.C.P. Kerckhoffs, J.H. Omens, and A.D. McCulloch. A single strain-based growth law predicts concentric and eccentric cardiac growth during pressure and volume overload. *Mechanics Research Communications*, 42:40–50, 2012.

[61] D. Klepach, LC. Lee, JF. Wenk, MB. Ratcliffe, TI. Zohdi, JL. Navia, GS. Kassab, E. Kuhl, and JM. Guccione. Growth and remodeling of the left ventricle: A case study of myocardial infarction and surgical ventricular restoration. *Mechanics Research Communications*, 42:134–141, 2012.

[62] S.M. Klisch, A. Hoger, and T.J. Van Dyke. A theory of volumetric growth for compressible elastic biological materials. *Mathematics and Mechanics of Solids*, 6(6):551–575, 2001.

[63] RF. Krause. *Growth, Modelling and Remodelling of Biological Tissue*. PhD thesis, University of Stuttgart, 2013.

[64] A. Krishnamurthy, CT. Villongco, J. Chuang, Lawrence R. Frank, V. Nigam, E. Belezzuoli, P. Stark, D. Krummen, S. Narayan, J. Omens, A. McCulloch, and RCP. Ker-

ckhoffs. Patient-specific models of cardiac biomechanics. *Journal of Computational Physics*, 244:4–21, 2013.

[65] Wilco Kroon, Tammo Delhaas, Peter Bovendeerd, and Theo Arts. Computational analysis of the myocardial structure: Adaptation of cardiac myofiber orientations through deformation. *Medical Image Analysis*, 13(2):346–353, 2009. ISSN 1361-8415.

[66] E. Kuhl. Growing matter: A review of growth in living systems. *Journal of the Mechanical Behavior of Biomedical Materials*, 29:529–543, 2014. doi: http://dx.doi.org/10.1016/j.jmbbm.2013.10.009. Review paper.

[67] P. Lafortune, R. Aris, M. Vazquez, and G. Houzeaux. Coupled electromechanical model of the heart: Parallel finite element formulation. *International Journal for Numerical Methods in Biomedical Engineering*, 28:7286, 2012.

[68] E.H. Lee. Elastic-plastic deformation at finite strains. *J. Appl. Mech.*, 36:1–6, 1969.

[69] D. Legner, S. Skatulla, J. MBewu, R.R. Rama B.D. Reddy, C. Sansour, N.H. Davies, and T. Franz. Studying the influence of hydrogel injections into the infarcted left ventricle using the element-free galerkin method. *International Journal for Numerical Methods in Biomedical Engineering*, 30:416–429, 2014.

[70] P.J. Lynch. Heart normal anatomy coronal cross section. Online, December 2006. URL `https://commons.wikimedia.org/wiki/File:Heart_anterior_view_coronal_section.jpg`.

[71] E. Marieb and K. Hoehn. *Anatomy and physiology*. Pearson Education, Inc., six edition, 2007.

[72] E. Marijon, M. Mirabel, Celermajer DS., and X. Jouven. Rheumatic heart disease. *The Lancet*, 379(9819):953–964, 2012. doi: http://dx.doi.org/10.1016/S0140-6736(11)61171-9.

[73] M. Marjorie, J. van Berlo, and J. Molkentin. Molecular basis of physiological heart growth: fundamental concepts and new players. *HHS Public Access*, 14(1):38–48, May 2013. doi: 10.1038/nrm3495.

[74] A. Menzel and E. Kuhl. Frontiers in growth and remodeling. *Mechanics Research Communications*, 42:1–14, 2012. doi: http://dx.doi.org/10.1016/j.mechrescom.2012.02.007.

[75] N.M. Newmark. A method for computation of structural dynamics. *ASCE Journal of the Engineering Mechanics Division*, 85:67–94, 1959.

[76] S.A. Niederer and N.P. Smith. The role of the frank–starling law in the transduction of cellular work to whole organ pump function: a computational modeling analysis. *PLoS Computational Biology*, 5(4):e100037, 2009.

[77] JT. Oden. *Finite elements of nonlinear continua*. McGraw-Hill, New York, 1972.

[78] Wikiversity Journal of Medicine. The heart wall. Online, September 2013. URL `http://en.wikipedia.org/wiki/Cardiac_muscle#/media/File:Blausen_0470_HeartWall.png`. The permission to use this work has been archived in the Wikimedia OTRS system. Full documentation is available only to OTRS volunteers as ticket #2013061010006654.

[79] J. H. Omens, S. M. Vaplon, B. Fazeli, and A. D. McCulloch. Left ventricular geometric remodeling and residual stress in the rat heart. *Journal of Biomechanical Engineering*, 120(6):715–9, December 1998.

[80] L. H. Opie, P. J. Commerford, B. J. Gersh, and M. A. Pfeffer. Controversies in ventricular remodelling. *Lancet*, 367(9507):356–67, Jan 28 2006.

[81] H. Qin and D. Terzopoulos. Dynamic nurbs swung surfaces for physics-based shape design. *Computer-Aided Design*, 27(2):111–127, 1995. doi: http://dx.doi.org/10.1016/0010-4485(95)92151-H.

[82] R.R. Rama, S. Skatulla, and C. Sansour. Real-time modelling of diastolic filling of the heart using the proper orthogonal decomposition with interpolation. *International Journal of Solids and Structures*, 2015. under review.

[83] M. K. Rausch, A. Dam, S. Göktepe, O. J. Abilez, and E. Kuhl. Computational modeling of growth: systemic and pulmonary hypertension in the heart. *Biomechanics and Modeling in Mechanobiology*, 10(6):799–811, 2011. doi: 10.1007/s10237-010-0275-x.

[84] T. Ricken. Skriptum zur vorlesung multiphase materials. Technische Universität Dortmund, July 2014.

[85] T. Ricken and J. Bluhm. Remodeling and growth of living tissue: a multiphase theory. *Archive of Applied Mechanics*, 80:453–465, 2010. doi: 10.1007/s00419-009-0383-1.

[86] T. Ricken, A. Schwarz, and J. Bluhm. A triphasic model of transversely isotropic biological tissue with applications to stress and biologically induced growth. *Computational Materials Science*, 39:124–136, 2007. doi: http://dx.doi.org/10.1016/j.commatsci.2006.03.025.

[87] T. Ricken, U. Dahmen, and O. Dirsch. A biphasic model for sinusoidal liver perfusion remodeling after outflow obstruction. *Biomechanics and Modeling in Mechanobiology*, 9(4):435–450, January 2010. doi: 10.1007/s10237-009-0186-x.

[88] T. Ricken, D. Werner, HG. Holzhütter, M. König, U. Dahmen, and O. Dirsch. Modeling function-perfusion behavior in liver lobules including tissue, blood, glucose, lactate and glycogen by use of a coupled two-scale PDE-ODE approach. *Biomech Model Mechanobiol*, 14(3):515–536, 2015. doi: 10.1007/s10237-014-0619-z.

[89] E.K. Rodriguez, J.H. Omens, LK Waldman, and AD McCulloch. Effect of residual stress on transmural sarcomere length distributions in rat left ventricle. *American Journal of Physiology-Heart and Circulatory Physiology*, 264(4):H1048, 1993.

[90] E.K. Rodriguez, A. Hoder, and A.D. McCulloch. Stress-dependent finite growth in soft elastic tissues. *Journal of Biomechanics*, 27:455–467, 1994.

[91] J. Schröder. *Plasticity and Beyond*, chapter A numerical two-scale homogenization scheme: the FE^2 -method, pages 1–65. Springer Wien Heidelberg New York Dordrecht London, 2014.

[92] S. Skatulla and C. Sansour. On a path-following method for non-linear solid mechanics with applications to structural and cardiac mechanics subject to arbitrary loading scenarios. *International Journal of Solids and Structures*, 96:181–191, 2016. doi: http://dx.doi.org/10.1016/j.ijsolstr.2016.06.009.

[93] K. Sliwa and P. Zilla. Rheumatic heart disease: The tip of the iceberg. *Circulation*, 125: 30603062, 2012. doi: https://doi.org/10.1161/CIRCULATIONAHA.112.114199.

[94] JS. Soares, S. Pasta, D. Vorp, and JE. Moore. Modeling in cardiovascular biomechanics. *International Journal of Engineering Science*, 48(11):1563–1575, 2010.

[95] M.S. Spach and J.F. Heidlage. The stochastic nature of cardiac propagation at a microscopic level: electrical description of myocardial architecture and its application to conduction. *Circulation research*, 76(3):366, 1995. doi: https://doi.org/10.1161/01.RES.76.3.366.

[96] L. Taber. Biomechanics of growth, remodeling and morphogenesis. *Applied Mechanics Reviews*, 48:487–545, 1995.

[97] C. Truesdell. *Rational Thermodynamics.* Springer-Verlag New York Berlin Heidelberg Tokyo, 1984.

[98] C. Truesdell and R. Toupin. The classical field theories. In S. Flügge, editor, *Handbuch der Physik*, volume 3, chapter 1. Springer-Verlag, Berlin, 1960.

[99] T.P. Usyk, R. Mazhari, and A.D. McCulloch. Effect of laminar orthotropic myofiber architecture on regional stress and strain in the canine left ventricle. *Journal of Elasticity*, 61:143–164, 2000. ISSN 0374-3535. URL `http://dx.doi.org/10.1023/A:1010883920374`. 10.1023/A:1010883920374.

[100] K.C. Vinnakota and J.B. Bassingthwaighte. Myocardial density and composition: a basis for calculating intracellular metabolite concentrations. *American journal of physiology. Heart and circulatory physiology*, 286(5):H1742–H1749, 2004. doi: 10.1152/ajpheart.00478.2003.

[101] K. Volokh. Stresses in growing soft tissues. *Acta Biomaterialia*, 2:493–504, 2006.

[102] K.Y. Volokh and Y. lev. Growth, anisotropy, and residual stresses in arteries. *Mechanics & chemistry of biosystems*, 2(1):27–40, 2005.

[103] K. von Terzaghi. *Erdbaumechanik auf bodenphysikalischer grundlage.* Franz Deuticke, 1925.

[104] K. von Terzaghi. Principles of soil mechanics. *Engineering News-Record*, 19, 20, 21, 22, 23, 25, 26, 26:742–746, 796–800, 832–936, 974–978, 912–915, 987–999, 1026–1029, 1064–1068, 1925.

[105] WA. Wall, L. Wiechert, A. Comerford, and S. Rausch. Towards a comprehensive computational model for the respiratory system. *International Journal for Numerical Methods in Biomedical EngineeringInternational Journal for Numerical Methods in Biomedical Engineering*, 26(1):807–827, 2010. doi: 10.1007/s10237-010-0275-x.

[106] C. D. Werner, F. B. Sachse, and O. Dssel. Electrical excitation propagation in the human heart. *International Journal of Bioelectromagnetism*, 2, 2000.

[107] D Werner, T Ricken, and A F Pfeiffer. On a FEM model for isotropic and transversely isotropic growth in biphasic materials. *Proceedings in Applied Mathematics and Mechanics*, 13:63–64, 2013. doi: 10.1002/pamm.201310027.

[108] Daniel Werner, Tim Ricken, Uta Dahmen, Olaf Dirsch, Hermann-Georg Holzhütter, and Matthias König. On the Influence of Growth in Perfusion Dependent Biological Systems - at the Example of the Human Liver. *Pamm*, 15(1):119–120, 2015. ISSN 16177061. doi: 10.1002/pamm.201510050. URL `http://onlinelibrary.wiley.com/doi/10.1002/pamm.201510050/abstract`.

[109] C. Wieners. *Taylor-Hood elements in 3D*, pages 189–196. Springer, 2003.

[110] J. Wong and E. Kuhl. Generating fibre orientation maps in human heart models using poisson interpolation. *Computer Methods in Biomechanics and Biomedical Engineering*, 17:1217–1226, 2014. doi: doi:10.1080/10255842.2012.739167.

[111] Y. Yuan. Recent advances in numerical methods for nonlinear equations and nonlinear least squares. *Numerical Algebra, Control and Optimization*, 1(1):15–34, 2011. doi: 10.3934/naco.2011.1.15.

[112] M.R. Zile, M. Tomita, K. Nakano, I. Mirsky, B. Usher, J. Lindroth, and B.A. Carabello. Effects of left ventricular volume overload produced by mitral regurgitation on diastolic function. *American Journal of Physiology - Heart and Circulatory Physiology*, 261(5): H1471–H1480, 1991.